



**HAL**  
open science

# Development and application of simultaneous 2D flow velocity and gas temperature measurements using thermographic phosphors under engine-relevant conditions

Valerio Frattina

► **To cite this version:**

Valerio Frattina. Development and application of simultaneous 2D flow velocity and gas temperature measurements using thermographic phosphors under engine-relevant conditions. Chemical and Process Engineering. Université Paris Saclay (COMUE); Universität Duisburg-Essen, 2019. English. NNT : 2019SACLCO73 . tel-02466375

**HAL Id: tel-02466375**

**<https://theses.hal.science/tel-02466375>**

Submitted on 4 Feb 2020

**HAL** is a multi-disciplinary open access archive for the deposit and dissemination of scientific research documents, whether they are published or not. The documents may come from teaching and research institutions in France or abroad, or from public or private research centers.

L'archive ouverte pluridisciplinaire **HAL**, est destinée au dépôt et à la diffusion de documents scientifiques de niveau recherche, publiés ou non, émanant des établissements d'enseignement et de recherche français ou étrangers, des laboratoires publics ou privés.

# Development and application of simultaneous 2D flow velocity and gas temperature measurements using thermographic phosphors under engine-relevant conditions

Thèse de doctorat de l'Université de Duisburg-Essen et de l'Université Paris-Saclay, préparée à CentraleSupélec

École doctorale n°579

Sciences Mécaniques et Energétiques, Matériaux et Géosciences

Spécialité de doctorat : Energétique

Thèse présentée et soutenue à Duisburg, le 21/10/2019, par

**Valerio Frattina**

Composition du Jury :

Christine Rousselle

Professeur, Université Orléans (PRISME)

Président

Thierry Schuller

Professeur, Université Toulouse III (IMFT)

Rapporteur

Benoit Fond

Maitre de conférences, Université de Magdeburg (OVGU)

Examineur

Sebastian Kaiser

Professeur, Université de Duisbourg-Essen (IVG)

Examineur

Gilles Bruneaux

Ingénieur de Recherche, IFPEN

Directeur de thèse

Christof Schulz

Directeur de Recherche, Université de Duisbourg-Essen (IVG)

Directeur de thèse

**Titre :** Développement et application d'une technique de diagnostic optique pour des mesures 2D et non-intrusives de température et de vitesse des gaz en condition moteur

**Mots clés :** température, PIV, phosphore, diagnostic optique,

**Résumé :** Dans le cadre de cette thèse, une technique de diagnostic optique a été développée pour mesurer simultanément la température et la vitesse de gaz dans un moteur thermique transparent.

La technique de la PIV-thermographique (T-PIV) combine la thermométrie par phosphorescence et la vélocimétrie par image de particules (PIV) et offre la possibilité de mesurer simultanément la température et la vitesse du gaz. Le matériau luminophore approprié a été choisi en testant trois luminophores disponibles dans le commerce : BAM:Eu<sup>2+</sup>, ZnO et ZnO:Zn.

L'émission lumineuse et la réponse spectrale à divers paramètres, y compris la température, ont été mesurées dans un écoulement gazeuxensemencé de particules afin de reproduire les conditions rencontrées typiquement dans un moteur. Cela a permis d'obtenir une courbe d'éta-lonnage dépendante de la température à utiliser dans les expériences sur moteur. Les particules de ZnO:Zn montrent une sensibilité relativement plus forte à la température permettant une précision plus élevée sur la mesure de température.

Pour ces raisons, le ZnO:Zn a été choisi comme candidat approprié pour les mesures dans le moteur transparent.

Les mesures ont été effectuées à un régime moteur de 1200 tr/min avec une fréquence d'échantillonnage de 10 Hz entre 180 et 540°vil sans combustion.

Les champs de température et de vitesse ont été mesurés avec succès à différents angles vilebrequin pendant la phase de compression et de détente. Les champs de température obtenus expérimentalement sont comparés aux températures obtenues à partir d'une simulation 0D montrant un écart de température d'environ 1% (200°vil) et de 14% (480°vil) par rapport au modèle de simulation. La précision de mesure estimée est de 55 K (18%) à 300 K et de 2 K (0.3%) à 614 K sur une moyenne de 200 cycles.

La T-PIV a également été testé pour mesurer la température des gaz en post-combustion. Dans ce cas, les mesures étaient impossibles, probablement en raison d'une dégradation du matériau luminophore utilisé qui ne résiste pas aux températures élevées de la combustion. Les perspectives de développements futurs qui résultent de ces résultats sont la sélection d'un luminophore capable de résister à plus hautes températures.

Enfin, la technique montre un grand potentiel de développement dans un environnement moteur.

**Title:** Development and application of simultaneous 2D flow velocity and gas temperature measurements using thermographic phosphors under engine-relevant conditions

**Keywords:** Thermographic PIV, thermographic phosphor, temperature, laser diagnostics

**Abstract:** A non-intrusive laser diagnostics technique has been developed for simultaneous measurements of velocity and gas temperature in optically accessible internal combustion engines. The technique, thermographic PIV (T-PIV) combines phosphor thermometry and particle image velocimetry (PIV) and offers the possibility of simultaneous measurement of gas temperature and velocity.

Suitable phosphor materials were selected by testing three commercially available phosphors: BAM:Eu<sup>2+</sup>, ZnO and ZnO:Zn. The luminescence emission and the spectral response to various parameters including temperature were measured yielding a temperature-dependent calibration curve to be used for signal interpretation in engine experiments. The ZnO:Zn phosphor shows the highest sensitivity to temperature allowing higher temperature precision. Therefore, ZnO:Zn phosphor was chosen as the suitable candidate for engine measurements.

Measurements were performed in an internal combustion engine at a speed of 1200 rpm with a sampling rate of 10 Hz between 180 and 540°CA under motored conditions. The temperature and velocity fields were measured successfully at various times throughout the compression and the exhaust stroke. The obtained temperature fields are compared with simulated bulk-gas temperatures from a 0D model-based simulation showing a temperature deviation of around 1% (200°CA) to 14% (480°CA) from the model. The measurement accuracy was found to be 55 K (18%) at 300 K and 2 K (0.3%) at 614 K for the 200-cycles average.

The potential of the diagnostics was tested also in in cylinder post-combustion gases. In this case, the diagnostics was failing probably due to the characteristics of the phosphor used, which does not seem to resist to high combustion temperatures degrading its luminescence properties. The potential of T-PIV in post-combustion gases remains under the conditions of finding more resistant phosphor particles.

**Titel:** Entwicklung und Anwendung einer simultanen, 2D-Geschwindigkeits-, und Temperaturmessmethode mittels thermographischer Phosphore unter motorischen Bedingungen

**Schlüsselwörter :** Thermographische PIV, thermographischer Phosphor, Temperatur, Laserdiagnostik

**Zusammenfassung:** In der vorliegenden Arbeit wurde eine nicht-intrusive Methode der Laserdiagnostik zur simultanen Messung von Gasgeschwindigkeit und -temperatur in einem optisch zugänglichen Verbrennungsmotor entwickelt und getestet. Diese Messmethode der thermographischen PIV (T-PIV) kombiniert Phosphorthermometrie mit Particle Image Velocimetry (PIV) und ermöglicht die simultane Messung von Geschwindigkeit und Temperatur eines Gases.

Im Verlauf der Arbeit wurden drei kommerziell verfügbare Phosphormaterialien für die Motorexperimente getestet: BAM:Eu<sup>2+</sup>, ZnO and ZnO:Zn. Die optischen Eigenschaften und die Spektralantwort des Phosphors auf Parametervariationen wie Temperaturänderungen wurden gemessen. Daraus wird eine temperaturabhängige Kalibrationskurve erstellt, die zur Temperaturmessung im Motor dient. Der Phosphor ZnO:Zn wurde für Temperaturmessungen im Motor ausgewählt, da die optischen Eigenschaften des Phosphors die größte Sensitivität zu Temperaturänderungen aufweisen.

In einem Verbrennungsmotor wurden Temperaturmessungen bei 1200 U/min und 10 Hz unter geschleppten Bedingungen zwischen 180°KW und 540°KW durchgeführt. Geschwindigkeit und Temperatur des Gases wurden an mehreren Kurbelwinkeln während des Verdichtungs- und Expansionstaktes gemessen und die Gastemperatur mit der Restgastemperatur einer 0D Simulation verglichen. Die Abweichung zwischen Mess- und Simulationsergebnissen beträgt 1% (200°KW) und 14% (480°KW). Die Messgenauigkeit für den Mittelwert über 200 Messzyklen beträgt 55 K (18%) bei 300 K und 2 K (0.3%) bei 614 K.

Die Messmethode wurde außerdem zur Restgastemperaturmessung im gefeuerten Betrieb des optischen Motors angewandt. Jedoch konnte unter diesen Bedingungen keine validen Messungen durchgeführt werden, da der Phosphor möglicherweise bei Verbrennungstemperaturen degradiert und die Lumineszenz-Eigenschaften verändert werden. Eine erfolgreiche Anwendung von T-PIV unter motorischen Bedingungen wird künftig unter der Voraussetzung möglich sein, dass verbrennungsresistente Phosphormaterialien gefunden werden.

**Development and application of simultaneous 2D flow velocity and gas temperature measurements using thermographic phosphors under engine-relevant conditions**

Der Fakultät für Ingenieurwissenschaften, Abteilung Maschinenbau und Verfahrenstechnik der

Universität Duisburg-Essen

zur Erlangung des akademischen Grades

eines/einer

Doktors der Ingenieurwissenschaften

Dr.-Ing.

vorgelegte Dissertation

von

Valerio Frattina

aus

Sora (Italien)

Gutachter: Univ.-Prof. Dr. rer. nat. Christof Schulz

Ing., Dr., HdR, Gilles Bruneaux

Tag der mündlichen Prüfung: 21.10.2019



---

## ACKNOWLEDGMENTS

This thesis is the achievement of three years of work at IFPEN (France) and at University of Duisburg-Essen (Germany). First, I would like to thank all the people who contributed to the results obtained in this work. The PhD was a great experience where I had the opportunity to work with many people: researchers, technicians, students... Thanks to all of them!

Thanks to my German supervisor, Christof for his patient guidance, criticism and support during these years and more in particular during the time I was writing the manuscript; I really appreciated your sense of perfection and precision... I learned a lot from you. Thanks Christof!

Thanks to my French supervisor and friend, Gilles for his advice, support and friendship. He is for me a source of inspiration. He always arrives to combine work, sport and pleasure together. We had funny moments during our boxing sections at lunchtime. He always hits me with his strong right hook... See you soon... I will back soon!

Thanks also to my German advisor, Torsten. He supported me during my visit in Duisburg, helping me with the experimental apparatus.

A special thanks to my French advisor and friend, Michele for his support and continuous encouragement. We had fruitful discussions during the last engine campaign about the post-processing algorithm. He also helped me by revising and correcting the manuscript... Thanks dude!

Thanks to all the technicians that have worked with me at IFPEN: Jerome, Laurent, Thomas, Vincent, Clément, Francis... we had many fruitful discussions together.

I must express my profound gratitude to my parents for their continuous support and encouragement during these years. Thanks also to my two sisters for their moral support. In addition, I would like to thank all friends/colleagues who have helped me during hard times: Federico, Michele, Hubert, Viviana, Luca, Simone, Andrea.

A special thanks to Matthias, he helped me in the organization of the drink after the defense, with big pizzas. Thanks dude!

A special thanks to my wife Clémence for her unconditional encouragements and lovely attentions. She supported me during the most difficult times when writing the thesis; she gave me the right inputs and moral support. Also thanks to my little daughter Gabrielle for her "encouragements" with lovely smiles during the defense's day.

I would like to thank my examiners and all members of the jury for the fruitful discussion and the helpful remarks.

---

# CONTENTS

ACKNOWLEDGMENTS .....	1
CONTENTS .....	2
1 INTRODUCTION.....	7
2 LASER-BASED STRATEGIES FOR MEASURING FLOW FIELDS AND TEMPERATURE 11	
2.1 Flow-field measurements .....	11
2.2 Temperature measurement .....	12
2.2.1 Rayleigh scattering.....	12
2.2.2 Coherent anti-Stokes Raman scattering (CARS).....	12
2.2.3 Laser-Induced fluorescence (LIF) .....	13
2.3 Phosphor thermometry (PT).....	14
2.4 Summary .....	14
3 THERMOGRAPHIC PIV (T-PIV) .....	16
3.1 Principle of thermographic PIV.....	16
3.2 Particle Image Velocimetry .....	16
3.3 Phosphor thermometry .....	17
3.3.1 Definition of thermographic phosphors.....	18
3.3.2 Basic mechanisms of luminescence .....	19
3.3.3 Global view of electronic transitions.....	20
3.3.4 Absorption.....	21
3.3.5 Luminescence emission .....	22
3.3.6 Non-radiative relaxation .....	22
3.3.7 Energy transfer.....	23
3.3.8 Temperature effects .....	24
3.3.9 Thermal response of the luminescence lifetime.....	25
3.3.10 Thermal response of the emission spectrum.....	25
3.4 Phosphor thermometry strategies .....	28
3.4.1 Lifetime method.....	28

---

3.4.2	Two-color intensity-ratio method.....	29
3.5	Choice of phosphor .....	30
3.6	Overview of applications.....	32
3.7	Engine applications: Potentials and challenges .....	34
3.8	Approach of the thesis .....	35
3.8.1	Specific objectives .....	35
3.8.2	Research methodology.....	36
4	CHARACTERIZATION OF PHOSPHOR PARTICLES .....	38
4.1	Phosphor selection.....	38
4.1.1	BAM:Eu <sup>2+</sup> .....	38
4.1.2	ZnO and ZnO:Zn.....	38
4.2	Characterization of phosphors on coated surfaces .....	39
4.2.1	Experiment.....	39
4.2.2	Laser fluence effect.....	41
4.2.3	Temperature dependence.....	46
4.3	Characterization of aerosolized phosphors.....	48
4.3.1	Experiment.....	48
4.3.2	Excitation system.....	48
4.3.3	Detection system.....	49
4.3.4	Particle preparation .....	49
4.3.5	Particle seeding .....	50
4.3.6	Particle counting system .....	51
4.4	Results obtained for aerosolized phosphor particles .....	53
4.4.1	Seeding density effect.....	53
4.4.2	Laser fluence effect.....	56
4.4.3	Temperature dependence.....	57
4.5	Comparison of the performance of phosphors in surface and aerosol measurements .....	61
4.6	Calibration procedure for two-color intensity-ratio method.....	63
4.6.1	Selection of detection wavelengths.....	64
4.6.2	Calibration data for temperature measurement .....	65
4.7	Uncertainty analysis .....	67
4.7.1	Measurements uncertainty.....	68

---

---

5	APPLICATIONS OF THERMOGRAPHIC PIV IN AN IC ENGINE .....	72
5.1	Context .....	72
5.2	Experiment .....	72
5.2.1	Characteristics of the optically-accessible engine .....	72
5.2.2	Particle seeding system.....	74
5.2.3	Optical measurement system .....	74
5.3	Particle image velocimetry (PIV) system.....	77
5.4	Image processing and measurements strategy.....	78
5.4.1	Image processing.....	78
5.5	Measurements strategy .....	81
5.6	Experimental results .....	83
5.6.1	Reference condition.....	83
5.6.2	Increased intake temperature condition .....	86
5.6.3	Temperature and velocity fields at the reference condition .....	88
5.6.4	Temperature and velocity fields with increased tumble .....	90
5.7	OD simulation of in-cylinder temperatures.....	93
5.7.1	Model description.....	93
5.7.2	Comparison of results: OD simulation vs. measurements .....	96
5.8	Measurement uncertainty .....	99
5.8.1	Effect of the calibration on the measurement uncertainty .....	101
5.8.2	Measurement precision .....	103
6	INFLUENCE OF SPRAY AND COMBUSTION.....	108
6.1	Experiments in the presence of fuel injection .....	108
6.2	Particle survival during combustion.....	111
7	PERSPECTIVES AND CONCLUSIONS .....	115
7.1	Perspectives .....	115
7.1.1	Diagnostics improvements .....	115
7.1.2	Applications of T-PIV in IC engines.....	116
7.2	Conclusions .....	117

---

---

8	REFERENCES.....	119
9	APPENDIX A.....	126

---

---

---

# 1 INTRODUCTION

Automobiles for a future sustainable society require a significantly reduced environmental impact. In this context, manufacturers are actively developing electrification technologies such as electric vehicles with batteries and/or fuel cells. However, there are many problems that must be overcome on the path towards electrification. These problems are not only technical, but also involve the development of new infrastructure such as new electricity networks with smart power grid, or distribution networks for alternative fuels such as hydrogen.

Hybrid electric vehicles (HEV) represent an alternative solution between conventional vehicles and battery electric vehicles (BEV). A hybrid car combines two or more power sources to move the vehicle. The most common architectures combine an internal combustion (IC) engine together with one or more electric motors. In this system, the two power sources are managed to work in the best efficiency conditions in order to increase fuel efficiency and reduce CO<sub>2</sub> emissions. In this context, IC engine will still play an important role for automobile in the near future.

Increasing the overall efficiency of internal combustion (IC) engines while reducing pollutants is a key development target of the automotive industry. A better understanding of physical and chemical phenomena during combustion process is needed for the development of new IC engines. The detailed measurement of parameters such as temperature and velocity field of the in-cylinder flow is fundamental for the optimization of the combustion process (e.g., heat transfer, flame propagation, auto-ignition, etc.) and to reduce pollutant formation. This is particularly true in the case of newly developed combustion modes, such as homogeneous-charge compression-ignition (HCCI) or low-temperature combustion (LTC), where enhanced air/fuel mixing and dilution are used to drastically reduce soot and NO<sub>x</sub> emissions. In these combustion modes, the ignition event is essentially controlled by chemistry, and thus, the temperature and velocity distribution in the cylinder have a strong influence on the combustion process. Moreover, in HCCI, stratification of the fresh-gas temperature has been demonstrated experimentally to be a key parameter to control the rate of pressure increase [1].

Temperature is a key parameter for many physical processes that occur in IC engines. When the fuel is injected in the cylinder, temperature directly affects evaporation and therefore has a major impact on wall impingement and fuel/air mixing. Temperature also has a strong influence on auto-ignition in Compression Ignition (CI) engines, since auto-ignition is mainly controlled by chemical kinetics. Moreover, the formation of pollutants in the hot gas environment, such as NO<sub>x</sub> or soot, is controlled by temperature. Therefore, obtaining detailed information on the in-cylinder temperature distribution is crucial for the development of efficient and clean combustion systems.

Velocity of the in-cylinder gas flow, on the other hand, affects the volumetric efficiency, the mixing process and also heat transfer. The in-cylinder gas flows are mainly important in the design of the combustion chamber. Moreover, the purpose of introducing rotating flow in the cylinder is to increase the combustion rate and extend the flammability limit. This may increase the engine thermal efficiency and at the same time, increased burning rates may reduce hydrocarbon (HC) and carbon monoxide (CO) emissions. Fast burning rate also allows rapid and stable combustion under lean conditions with a consequent reduction in fuel consumption.

---

In many cases, the gas velocity and temperature fields have strongly coupled effects on the complex in-cylinder processes. Simultaneous measurements of temperature and velocity are therefore of fundamental interest to study the fluid mechanics in IC engine.

Optical diagnostics techniques are especially effective in providing comprehensive and detailed information of flow fields, species concentration and temperature distribution in combustion processes. These techniques provide non-intrusive, *in situ*, spatially- and time-resolved measurements of a large variety of in-cylinder phenomena. These methods are used in combustion research to study the thermodynamics, chemical reactions and fluid dynamics of the in-cylinder mixture, before, during, and after combustion. Optical measurements also support numerical simulations through providing validation data. However, the engine environment is extremely hostile and the application of optical diagnostics with high accuracy and precision represents an important challenge.

Not many optical diagnostics techniques offer the capability of performing non-intrusive simultaneous measurements of temperature and velocity fields. A direct observation of the phenomena taking place inside the cylinder can hence help to understand the main physical processes involved. The investigation of the in-cylinder processes is particularly difficult due to the large variety of the phenomena involved: spray injection, turbulent mixing, chemical reactions, heat transfer, cycle-to-cycle fluctuations, knocking phenomena, misfire, etc. Moreover, all these phenomena take place within a short time and are affected by turbulent fluctuations. For detailed investigations of these quantities and their interaction, measurements in optically accessible engines are highly valuable.

Optically accessible engines are usually single-cylinder internal combustion engines, fitted with transparent parts to provide optical access to the combustion chamber, cylinder liner, and piston bowl/surface. Using the optical access, various processes taking place in the combustion chamber may be studied via optical diagnostics techniques. However, when using an optical engine for engine development and validation purposes the optical engine should resemble the “real” engine it is based on.

The development and application of a new diagnostics must fulfill high standards in term of experimental accuracy and spatial resolution, in order to provide valuable descriptions of the physical phenomena associated to a wide range of applications and studies. A brief literature review is presented in the next section to list the optical diagnostics available for simultaneous temperature and velocity measurements.

In this work, thermographic PIV is used to evaluate the in-cylinder temperature and velocity fields under engine relevant conditions. The main objective is to simultaneously measure the gas-phase temperature and the flow velocity in the cylinder of an optically accessible engine in motored operation. Simultaneous phosphor thermometry and particle image velocimetry (PIV) are chosen for this study. The combination of these diagnostics (hereafter referred as thermographic PIV) shows some attractive aspects making it particularly attractive for measurements in IC engines. During recent years, several applications have been conducted with thermographic phosphors and different phosphors have been tested [2–4], but only few of them are applications of this technique in IC engine conditions [5–7]. However, there are many aspects that need to be investigated in details to perform reliable and accurate measurements in this harsh environment.

The work presented in this thesis provides two main developments of the technique: i) a new *ex situ* calibration method is employed to characterize the phosphor particles and ii) this technique is applied

---

in an optical IC engine under multiple relevant conditions. This approach extends the validation of this technique in engine environment and it provides insight about the related experimental uncertainties.

This work is structured in six chapters, including the present introduction. In the next chapter, laser-optical methods for measuring temperature and gas velocity are introduced and compared and the state of the art of the Thermographic PIV is presented. In Chapter 3, the basic theory of thermographic phosphors and their luminescence properties is detailed. A literature review of the main applications of phosphor thermometry in IC engines is also provided. At the end of this chapter, the approach used in this thesis combined with the measurement strategy is presented. The fourth chapter describes the characterization of the phosphors that has been employed in this work together with the characterization methods used for the calibration of the luminescence signal. In Chapter 5, the application of thermographic PIV in IC engine is presented discussing the performance of the technique and its uncertainties. In the last chapter, a summary of the main findings and conclusions of this study is reported and the key areas of future developments are identified.

---

---

---

## 2 LASER-BASED STRATEGIES FOR MEASURING FLOW FIELDS AND TEMPERATURE

In this section, the main existing techniques for simultaneous temperature and velocity measurement in gas flow via laser-based methods are presented with a brief literature review. The following discussion is restricted to techniques that enable planar imaging of temperature with a possible combination with particle image velocimetry (PIV). An important consideration was to take into account the suitability of the existing techniques in terms of their potential to perform measurements in IC engine under relevant conditions.

### 2.1 Flow-field measurements

The most common laser based gas-phase velocimetry techniques are using the light scattering from particles/droplets present in the flow. These particles can be naturally present in the flow or they can be added for the application of the velocimetry technique.

Laser Doppler velocimetry (LDV) is used to measure the instantaneous velocity of a flow field, by analyzing the Doppler shift between the incident and scattered light frequencies from seeded particles. Measurements are made at a precise point defined by the intersection of two collimated, coherent laser beams, forming a fringe pattern. As a particle passes through the fringe pattern, it scatters light from the beams into a detector. The frequency of the resulting Doppler shift is directly proportional to the particle velocity. LDV is a powerful pointwise technique providing a high temporal resolution of one or two components of the velocity vector [8]. LDV is most frequently used for determining the velocity of droplets, e.g., in a spray, that do not represent the velocity of the surrounding gas.

Particle image velocimetry (PIV) is a widely used technique for measuring instantaneous gas-phase velocity fields in transparent media. In the most general case, a double-pulse laser with a defined pulse delay is used for light-sheet illumination of a cross-section of the flow. The light scattered by the particles is recorded in one or two images, each one collecting the light scattered by each one of the two laser pulses. The displacement of particles between the two images can be determined by a cross-correlation algorithm that evaluates the displacement each image pair. This configuration allows to determine the two component of velocity in a planar domain [9,10].

Extensions of this technique include stereoscopic PIV and tomographic PIV. In stereoscopic PIV, two cameras with different viewing angles are used to enable the determination of the third component of the velocity field within a volume illuminated with a widened light sheet. With this method, three components of the velocity in a two-dimensional domain are determined [11,12]. In tomographic PIV, several cameras and volumetric laser illumination enable to determine the three components of the velocity in a three dimensional domain [13,14]. PIV is extensively used for flow measurements in IC engine, providing a high spatial resolution of the velocity-field measurement [12,15].

---

## 2.2 Temperature measurement

### 2.2.1 Rayleigh scattering

Rayleigh scattering thermometry is based on the detection of light that is elastically scattered off gas molecules when illuminated by a laser source. The intensity of the scattered light is directly proportional to the laser intensity, the gas density, and the scattering cross-section, which depends on the gas composition in the probe volume. Knowing the effective scattering cross-section of the local gas mixture, temperature can be extracted from the measured gas density and pressure based on the (ideal) gas law [16].

Rayleigh scattering is a relatively strong process compared to, i.e., Raman scattering, and can therefore be applied for imaging measurements where a plane is illuminated by a laser light sheet and the signal is detected typically at right angle with a sensitive camera. This technique has been used for decades in combustion diagnostics, due to its strong signal, relatively simple setup and easy implementation [16,17]. However, Rayleigh scattering, as an elastic scattering process, suffers from interference from scattering from particles and spuriously scattered laser light from the surrounding surfaces. The combination of this technique with particle image velocimetry (PIV) is therefore not possible due to the large scattering cross-section of particles compared to gas molecules.

Filtered Rayleigh scattering has been used to spectrally separate the scattering from the particles from the Rayleigh signal from the gas [18–20]. For this purpose, a molecular or atomic filter, i.e., iodine, is employed to block the narrowband scattering from large particles and surfaces and transmit the temperature- (i.e., Doppler-) broadened Rayleigh signal. This approach has been used in combination with PIV in premixed flames [21–23]. However, the application of this technique is restricted to experiments in which the local gas composition is known and thus the effective gas-phase scattering cross-section is known.

### 2.2.2 Coherent anti-Stokes Raman scattering (CARS)

CARS is a four-wave mixing process based on the nonlinear response of the molecules to the incident electromagnetic waves of the laser beams. The pump, Stokes, and probe frequencies interact with the molecule of interest, to generate a coherent optical signal at the anti-Stokes frequency. When the difference in frequency between the pump and the Stokes beams is in resonance with a molecular vibration, the CARS signal can be significantly enhanced. This signal, from which the temperature information is extracted, propagates as a laser-like beam in a direction given by the phase-matching condition. From the generated spectrum, the temperature but also the species concentration can be extracted from the spectrum shape after a calibration process. CARS is one of the most powerful techniques for temperature measurements in term of accuracy, precision, and application in harsh environments [24,25]. This technique has been applied in a wide range of reacting and non-reacting flows including IC engines [26,27] and sprays [28]. However, this technique in general provide a point-wise measurement with a spatial resolution in one direction limited at few mm. Recently it has been extended to 2D measurements using a new two-beam method, instead of three, and a 2D imaging spectrometer [29]. In theory, CARS could also be combined with PIV to obtain a velocity-temperature field, but currently the field of view is still limited by the laser beam dimension in the probe volume.

---

### 2.2.3 Laser-Induced fluorescence (LIF)

In laser-induced fluorescence, atoms or molecules are electronically excited by absorption of laser light. The following return to the ground state partially takes place by spontaneous emission of photons over a short duration (nanosecond scale). This fast radiative emission is called fluorescence. The fluorescence signal intensity is a function of the molecular number density with strong dependence on temperature, pressure, and bath-gas composition. LIF is often used for quantitative studies of fuel concentration, temperature, fuel/air ratio in combustion system [25,30–32]. A wide range of atoms and molecules can be used for LIF thermometry, i.e., specifically added tracers such as indium atoms, NO, and a variety of organic molecules as well as with naturally occurring species such as OH and O<sub>2</sub> [33–35].

In two-line atomic fluorescence (TLAF), two temperature-sensitive electronic states in thermal equilibrium with the combustion gas are excited with two laser pulses. The ratio of the two-line emission is proportional to the temperature. TLAF based on a two-line excitation of indium has been used for temperature measurements in an IC engine over a wide temperature range, 800–2800 K [36]. However, atomic indium is only formed in the flame from precursors added to the fresh gas, thus the temperature can only be measured in post-flame regions.

In a similar way ro-vibrational states of small molecules, e.g., NO, OH, can also be probed by the two-line or multi-line excitation concept. The radical OH is formed during the combustion process in the flame front so it can be exploited for thermometry only in the post-flame regions. NO can be added into the flow to allow temperature measurements in both burnt and unburnt regions. However, attention in the selection of the excitation/detection schemes, have to be made to avoid interferences from O<sub>2</sub>, CO<sub>2</sub>, PAH-LIF signals. Applications of NO-LIF in IC engine can be found in references [35,37]. More details about quantitative molecular LIF thermometry can be found in references [33,38–40].

Some organic molecules, including aromatic hydrocarbons and ketones are frequently used as tracers in LIF thermometry. These tracers, seeded in the flow, allow measurements in the fresh-gas regions only because tracers decompose above 1000 K, making temperature measurements impossible. Another drawback is that the fluorescence signal depends not only on temperature, but also on tracer concentration, pressure and local gas composition. Toluene-LIF thermometry has been used to investigate the thermal stratification in HCCI engines [41–43]. This technique was also used in combination with PIV to measure the temporal evolution of the temperature stratification induced by compression and fuel injection in engine [44–46]. In all these studies, nitrogen instead of air, was used to avoid quenching of the toluene fluorescence signal by molecular oxygen.

---

## 2.3 Phosphor thermometry (PT)

Phosphor thermometry (PT) is based on the use of so-called thermographic phosphors as tracers for temperature determination. This technique has been mostly used for surface temperature measurements, but it has also been extended to gas-phase measurements [3].

In general, thermographic phosphors are microcrystalline solid materials doped with rare-earth elements. These materials are not sensitive to the pressure and the composition of the surrounding fluid; also, they are chemically inert with a high melting point. For all these properties, they are well suited for measurements in harsh environment like IC engines, gas turbine combustor walls, etc.

The luminescence properties of these materials strongly depend on temperature [10]. The temperature of the particle can be assessed by two main methods: by detecting the change in the duration of the luminescence emission after excitation, commonly called emission lifetime; and detecting the relative change of the emission intensity at two or more spectral ranges as a consequence of the temperature dependence of the shape of the emission spectra. The luminescence emission of the particles following the excitation pulse is recorded and the spectral or the temporal content is exploited to derive the temperature of the material.

Thermographic phosphors have been used for decades as tracers for remote surface temperature [2,47]. During recent years, this technique has been employed also for gas-phase thermometry where one prerequisite is the assumption of thermal equilibrium of particle and surrounding gas and negligible movement of the particle during the luminescence lifetime. Phosphor particles are seeded into the flow as a tracer and the detected luminescence is used to determine the flow temperature. A brief literature review of this technique is presented in the next chapter.

Typically, the particle size of these materials is of the same order of the materials used for particle image velocimetry (PIV). This aspect offers the possibility to employ thermographic phosphors also for the simultaneous velocity measurement. A detailed description of this technique is given in the next chapter.

## 2.4 Summary

The techniques described in this section are compared and presented in the following table that summarizes their main characteristics, advantages, and limitations.

Table 2-1: Summary of the existing optical diagnostic techniques for temperature measurements that can potentially be combined with particle-based flow-field measurements.

Technique	Spatial characteristics	$T / K$	Advantages	Limitations
Filtered Rayleigh scattering	imaging	300–2500	<ul style="list-style-type: none"><li>No seeding requirement</li></ul>	<ul style="list-style-type: none"><li>Needs to know the local gas composition</li><li>Narrow band filter</li><li>Stable narrow-band laser</li><li>Combined with PIV only in premixed flame</li></ul>

Coherent anti-Stokes Raman scattering (CARS)		pointwise	300–3000	<ul style="list-style-type: none"> <li>• Excellent accuracy/precision</li> <li>• Application in harsh environment</li> </ul>	<ul style="list-style-type: none"> <li>• Complex spectroscopy</li> <li>• Complex optical setup</li> <li>• Poor spatial resolution</li> <li>• Difficult to combine with PIV</li> </ul>
Laser-induced fluorescence (LIF)	Tracer LIF	imaging	300–900	<ul style="list-style-type: none"> <li>• Good precision</li> <li>• Can be combined with PIV</li> </ul>	<ul style="list-style-type: none"> <li>• Does not work in the post-flame zone</li> <li>• Possible quenching by O<sub>2</sub></li> <li>• Dependence on partial pressure</li> </ul>
	TIAF (indium)	imaging	800–2800	<ul style="list-style-type: none"> <li>• Good precision</li> <li>• Can be applied in sooting flames</li> </ul>	<ul style="list-style-type: none"> <li>• Measurements only in the post flame zone</li> </ul>
	NO LIF	imaging	250–3000	<ul style="list-style-type: none"> <li>• No seeding requirement</li> </ul>	<ul style="list-style-type: none"> <li>• Interference with O<sub>2</sub> LIF at high pressure</li> <li>• Absorption by CO<sub>2</sub> and H<sub>2</sub>O</li> </ul>
	OH LIF	imaging	1200–2600	<ul style="list-style-type: none"> <li>• No seeding requirement</li> </ul>	<ul style="list-style-type: none"> <li>• Measurements only in the post flame zone</li> </ul>
Phosphor thermometry (PT)		imaging	300–1000	<ul style="list-style-type: none"> <li>• Phosphor particles are inert</li> <li>• Insensitive to pressure</li> <li>• Insensitive to local gas composition</li> <li>• Can be combined with PIV</li> </ul>	<ul style="list-style-type: none"> <li>• The signal decreases with increasing temperature</li> <li>• Thermal equilibrium with local gas temperature must be critically analyzed</li> </ul>

This overview of techniques illustrates that simultaneous velocity and temperature measurements are a challenge and there are limitations for each technique. The presence of particles for velocimetry limits the choice of the thermometry technique that can be employed.

As a pointwise measurement, CARS technique does not allow the combination with PIV measurements. Similarly, the Rayleigh scattering signals depend strongly on local composition, and the evaluation of the species concentrations is required in order to measure temperature. The application of FRS combined with PIV turns out to be difficult and restricted to simple cases as premixed flames. LIF can be used combined with PIV but the main drawbacks are related to the tracer employed. LIF tracers tend to have optical properties that change as a function of the bath-gas environment, making the application of this technique complex and prevent the application after the onset of hydrocarbon decomposition and pre-ignition reactions.

PT combined with PIV has the advantage to use the same tracer particle material for both measurements after spectrally separating the luminescence (for PT) and the elastic scattering (for PIV). Also, due to their nature, these particles can be used in harsh environment like IC engines. The combination of PT and PIV is also called thermographic PIV (T-PIV). In the next chapter, a detailed overview of T-PIV is presented underlining the specific needs and challenges related to their engine application.

---

## 3 THERMOGRAPHIC PIV (T-PIV)

In this chapter, the state of the art of T-PIV technique is presented. Particle image velocimetry and phosphor thermometry techniques are presented outlining their strengths and their limitations. Phosphor thermometry is described in detail: A basic introduction of the luminescence processes involved is also presented with particular emphasis on the temperature-dependent processes and how these processes can be exploited for thermometry. Afterwards, the luminescence properties of phosphors useful for temperature measurements into engine are identified. In the last section, a review of flow measurement applications in engines is presented.

### 3.1 Principle of thermographic PIV

Thermographic PIV is using phosphor particles as a tracer for temperature and velocity measurements. The velocity of the flow is measured via particle image velocimetry: consecutive laser pulses (typically in the green wavelength range) emitted at well-defined time intervals are used to illuminate the seeded particles; the laser light scattered from the particles at each pulse, is imaged and the particle velocity is determined from the change in position [48]. At the same time, the temperature-dependent emissions of the particles are used to assess the flow temperature. Excited by a second laser pulse (typically in the UV range), the particles emit light: The duration and the spectrum of the emission can be used to determine their temperature. This approach is in general referred to as phosphor thermometry [49]. If the size of phosphor particles is selected correctly, e.g., for engine-relevant cases, typically in the order of 1–5  $\mu\text{m}$ , it can be assumed that they match the temperature and the velocity of the surrounding fluid. This approach offers the possibility of simultaneous measurement of temperature and velocity coupling phosphor thermography and PIV based on a single tracer.

The use of phosphor materials as a tracer has several advantages compared to LIF tracers. Thermographic phosphors are solid particles that exhibit a temperature-dependent luminescence emission following excitation. Unlike some of the LIF tracer, these materials are insensitive to pressure and local gas composition (e.g., signal quenching by molecular engine in aromatic fluorescence tracers). In addition, due to their nature (ceramic compound), they have a high melting point, meaning that they can resist high temperature and potentially survive in combustion environments while organic tracers decompose quickly in the flame front or in the pre-ignition phase at high temperature [30].

Furthermore, many phosphors have a broad absorption spectrum, making it possible to perform experiments with a wide range of excitation wavelength, including 3<sup>rd</sup> and 4<sup>th</sup> harmonics of Nd:YAG lasers. Their luminescence emission is often in the visible spectrum, simplifying signal detection. Also, in the literature much information can be found on a large variety of phosphors with different luminescence properties that have been employed before for thermometry (most work is reported for surface measurements).

In the next sections, the details of PIV and PT are presented separately underlining the specific needs and challenges related to their engine application.

### 3.2 Particle Image Velocimetry

---

In PIV, the velocity of the flow is indirectly measured by the velocity of the particles. Some requirements need to be fulfilled to make sure that the particles are closely tracking the flow motion. These are analyzed using the Stokes number (St) defined as

$$\text{St} = \frac{\rho_p d_p^2}{18 \mu \tau_f} \quad (1)$$

where  $\tau_f$  is the characteristic time of the flow. The value of St is the main criterion to quantify the ability of particles to follow the flow [9] since this number compares the inertia forces of the particles with the viscous forces exerted by the flow. For small Stokes numbers (significantly below unity), the particles behave like a perfect tracer and follow the flow motion; vice versa, for  $\text{St} > 1$ , the particles tend to become unresponsive to the fluid motion.

While the accuracy of the PIV measurements relies in the ability of the tracer particles to follow the instantaneous motion of the flow, excessively small particles have important drawbacks: For example, small particles improve the flow tracking but provide weak light scattering only. A compromise needs to be found between the adequate tracking ability of the particles and the intensity of the scattered light. Also, the response time of particle depends both on the particle size, density, and on the viscosity of the fluid that the particles move in. The appropriate particle size is chosen to have an adapted response time compared to the frequency fluctuations of the flow. It is reported that a particle diameter in the order of 2–3  $\mu\text{m}$ , with a density of  $6 \times 10^3 \text{ kg/m}^3$ , is able to follow turbulence frequencies of 1 kHz. Similar characteristics are shown by the phosphor particles. In fact, most phosphor particles such as ZnO:Zn ( $5.6 \times 10^3 \text{ kg/m}^3$ ) or BAM:Eu<sup>2+</sup> ( $3.7 \times 10^3 \text{ kg/m}^3$ ) have a density similar to tracers used in PIV such as Zirconium-oxide ( $5.7 \times 10^3 \text{ kg/m}^3$ ), resulting in a similar response times.

The seeding system is also of main importance for this technique. For high spatial resolution PIV, it is recommended to have a concentration of approximately 15 particles per interrogation volume [48]. Depending on the dimension of the probe volume, this criterion often corresponds to a seeding density between  $10^{10}$  and  $10^{11}$  particles/m<sup>3</sup>. A homogeneous and uniform seeding flow is desirable to avoid particle agglomeration. More details on these aspects are well explained by Melling [48].

### 3.3 Phosphor thermometry

This section provides a basic introduction to phosphorescence and the ways in which it can be used for remote temperature measurements. The photo-physics behind the luminescent emission and the way in which it is affected by temperature is described. The most effective methods to perform phosphor thermometry are described.

This section draws from the analysis provided in Ref. [3,50–52] and the reader can find further details in those references.

---

### 3.3.1 Definition of thermographic phosphors

A *phosphor* by definition is a “solid luminescent material”. The terminology originates in the 17<sup>th</sup> century where an alchemist from Bologna, Vincenzo Casciarolo, had the first experience with phosphor materials. He took a heavy crystalline stone near a volcano and he heated it intending to obtain a noble metal. At the end, he just obtained a luminescent material that emitted light in the dark after exposure to sunlight. After this experience, similar luminescent stones were named phosphors, from the Greek phosphorus, which means “light bearer” [53]. The name phosphor should not be confused with the chemical element phosphorus (P). Phosphorus can emit light due to chemiluminescence, which is responsible for its name. Due to their luminescent properties, phosphors are industrial products and used, e.g., in fluorescent lamps, cathode ray tube (CRT), and frequency converters in LEDs.

The process of phosphorescence involves the absorption of energy and the following emission of light. The phosphors considered here are solid materials that consist of a “host material” doped with small amount of “activators” (Figure 3-1). The host material usually is microcrystalline, transparent to visible radiation and has a high melting point. The activator materials are usually lanthanide or transition-metal ions. The chemical composition is generally described by the following terminology,



where A is the crystalline compound acting as host material, B is the activator ion and  $n$  is the oxidation number of the activator [54].

For example, in phosphor materials like  $Y_3Al_5O_{12}:Dy^{3+}$  or  $Al_2O_3:Cr^{3+}$  (commonly referred as ruby), the host materials are yttrium aluminum garnet ( $Y_3Al_5O_{12}$ ) and aluminum oxide ( $Al_2O_3$ ), while the activators are respectively dysprosium ( $Dy^{3+}$ ) and chromium ( $Cr^{3+}$ ) ions. Solid-state chemistry methods are often used to produce the majority of doped-based phosphor materials. The right amount of activator and host materials are mixed/blended together and then fired in a furnace with a well-controlled atmosphere. Then, the obtained phosphor might be re-fired and ground depending on the desired particles morphology. The details of how phosphor powders are produced can be found in the “Phosphor Handbook” [43].

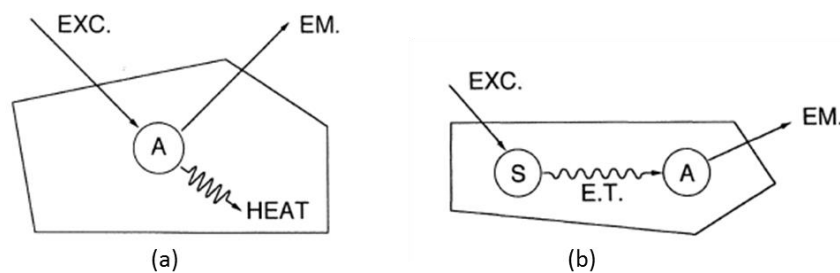


Figure 3-1: Schematics of a solid luminescent materials [55]. (A) Direct excitation (EXC) of the activator ion (A) following emission (EM) and non-radiative relaxation to the ground state (HEAT). (B) Indirect excitation of the activator by energy transfer (E.T.) from the sensitizer (S) to the activator.

Light absorption can occur either by the activator ions or by further dopants (“sensitizers”) as schematically described in Figure 3-1. When the absorption by the activator ions is too weak (e.g., because the optical transition is forbidden), sensitizers are added into the material that absorb the light and subsequently transfer its energy to the activator. Also, other dopants can be added to modify the emission color for a specific application [56]. The optical absorption can also take place by the lattice of the host

material itself. This process, called band absorption, involves the energy transfer from the host lattice to the activator, e.g., in  $\text{YVO}_4:\text{Eu}^{3+}$  or  $\text{ZnS}:\text{Ag}^+$  the host lattice transfers the excitation to the activator acting as sensitizer. Considering the same activator ion in two different host materials, the final optical properties are also different. The reason is to find in the different optical transitions acting between the activator and the host lattice. These optical transitions are governed by the strength of the crystal field. The crystal field is the electronic field acting on the activator ions due to the surrounding host materials [55].

In general, phosphors having luminescent emissions sensitive to temperature variations they are referred to as *thermographic phosphors*. The following sections describe the photo-physical process leading to luminescence and how these emissions can be used for temperature measurements.

### 3.3.2 Basic mechanisms of luminescence

The luminescence processes involve several complex and not well understood mechanisms. A simple two-level model, shown in Figure 3-2, can be used to illustrate the basics concepts of luminescence.

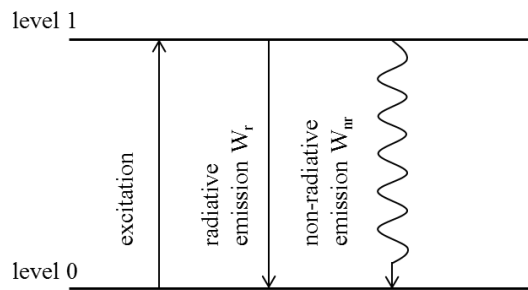


Figure 3-2: Simple two-level energy system showing excitation and radiative and non-radiative emission.

The exciting radiation is absorbed by the luminescence centers of the phosphor (e.g., activator ions, impurities, or sensitizer). The excitation directly or indirectly (through energy transfer) promotes the luminescence centers from the ground (level 0) to an excited state (level 1), leading to an initial population of  $N_{1_0}$  of excited centers. Following this, the excited state population returns to the ground state by emission of radiation and non-radiative relaxation. The global rate of the depopulation of the excited state is the sum of two contributions: the radiative  $W_r$  and the non-radiative  $W_{nr}$  transition probabilities. This process is analytically described as follows

$$W_{1 \rightarrow 0} = W_{nr} + W_r. \quad (3)$$

The depopulation of the excited state at an instant  $N_1(t)$  can be written as

$$\frac{dN_1(t)}{dt} = -(W_{nr} + W_r)N_1(t), \quad (4)$$

which can be rewritten, by solving for the term  $N_1(t)$ ,

$$N_1(t) = N_{1_0} \exp[-(W_{nr} + W_r)t] \quad (5)$$

By assuming the emitted intensity  $I$  as proportional to the radiative transition probability and the excited-state population  $N_1(t)$ , the equation can be written as,

$$I(t) = W_r N_1(t) = W_r N_{1_0} \exp(-t/\tau) \quad (6)$$

---

where  $\tau$  is the luminescence lifetime, defined as

$$\tau = \frac{1}{W_r + W_{nr}}. \quad (7)$$

The luminescence lifetime corresponds to the time required for the luminescence intensity to decrease by a factor of  $1/e$ .

The relaxation from the excited state to the ground state is a competition between radiative and non-radiative processes. In luminescence materials, the quantum efficiency is defined as the fraction of emitted light over the absorbed light, Eq. (8).

$$\eta = \frac{W_r}{W_r + W_{nr}} \quad (8)$$

High quantum efficiency is desirable to maximize the luminescence intensity. In phosphor engineering, significant effort is put in minimizing the non-radiative transitions and thus to enhance the quantum efficiency. Typical values of  $\eta$  lies between 50–95%, for phosphors such as  $\text{Sr}^2\text{P}^2\text{O}^7:\text{Eu}^{2+}$  and  $\text{Y}^2\text{O}^3:\text{Eu}^{3+}$  [53,55], used in fluorescent lamps.

In inorganic phosphors, the radiative transitions are considered forbidden by the quantum-mechanical selection rules. As a consequence, the radiative transitions are slow and occur over a large period of time, usually from  $10^{-6}$  to  $10^{-3}$  s.

The two-level model is a simplified approach with the assumption of two isolated energy levels. This model does not consider the interaction between other luminescence centers and impurities or dopants in the host lattice. In real phosphors, such interactions are always present and allow additional relaxation mechanism, responsible for multi-exponential luminescence decays [55]. Moreover, the presence of intermediate energy level transitions is the cause of light emissions at different energy and therefore, color. The rates of these electronic transitions as well as all the intermediate transitions are governed by quantum mechanical considerations. A brief description of these transitions is proposed in the following sections.

### 3.3.3 Global view of electronic transitions

Phosphor crystals are characterized by a valence band and a conduction band, separated by a wide energy gap (3–10 eV). The lower energy band occupied with electrons is called valence band, the band with higher energy level is called conduction band. The electronic band structure is modified with the addition of dopant ions or impurities (sensitizer). The electronic transitions take place between the band states of the host lattice and/or energy levels within the band gap. A detailed overview of the probable electronic transitions found in phosphors is given by Dorenbos et al. [57].

The electronic band structure and transition can be graphically described by means of the configurational coordinate model. As an example, Figure 3-3 presents the electronic transitions in a vibrating environment. This model shows the interactions between the absorbing ion and the vibrations of its surroundings. The potential energy curves of a luminescent center are plotted as a function of a configurational coordinate. This coordinate describes only one of the vibrational modes of the center involved. This mode is called symmetric stretching mode: In this specific case, the metal ion (luminescence center) is at rest and the surrounding ligands move toward and away from it, in phase.

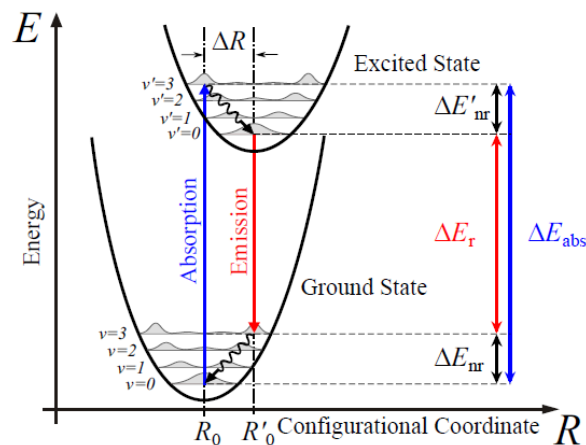


Figure 3-3: Configurational coordinate diagram showing electronic transitions between the ground state and the excited state [51].

In Figure 3-3, the  $x$ -axis represents the distance between the metal ion and the surrounding ligands, the  $y$ -axis the energy of the system. The potential energy of the ground and excited states are represented with a parabolic shape with a minimum in  $R_0$  and  $R'_0$ , respectively. The parabolic shape follows the assumption that the vibrational motion is harmonic and the restoring force is proportional to the displacement [55]. In the excited state, the equilibrium distance  $R'_0 \geq R_0$  corresponds to a larger bond length. This difference is due to the fact that in the excited state the chemical bond is often weaker and the parabolas are shifted relative to each other of a value  $\Delta R$ . The horizontal lines in the diagram show some of the vibrational energy levels with the corresponding probability density function. For the lowest vibrational level ( $v = 0$ ), the probability density function reaches its maximum at the equilibrium distance  $R_0$ . For higher vibrational levels, the wave functions have a more complex shape and the maxima of their probability density functions are located near the edges of the parabola.

In such a diagram, according to the Franck–Condon principle, the optical transitions are shown by vertical arrows. Since the electrons move much faster than the nuclei, the optical transitions take place in static surrounding ( $R = \text{constant}$ ). Both absorption and emission are optical transitions that occur between the ground state and the excited state. These transitions are represented as vertical lines in Figure 3-3. It is important to underline here, that not every possible transition between the ground state and the excited state occurs as optical transition. This is because the electronic transitions are governed by the quantum mechanical selection rules. For more details, see Ref. [55].

The following sections provide a simplified description of absorption, emission, non-radiative relaxation and energy transfer phenomena in phosphors.

### 3.3.4 Absorption

The absorption of light in homogeneous isotropic media follows the Beer–Lambert law,

$$I(z, \lambda) = I_0(\lambda) \exp[-\alpha(\lambda)z], \quad (9)$$

where  $\alpha(\lambda)$  is the absorption coefficient that is a property of a material and defines the amount of light absorbed.  $I_0(\lambda)$  is the incident light intensity minus reflection losses at the surface and  $z$  is the optical path length of the light through the material.

---

The absorption transition path is shown in Figure 3-3 as a blue vertical arrow. The optical transition starts from the lowest vibrational level, i.e.,  $v = 0$  and ends at  $v' > 0$  of the excited state. Therefore, the most probable transition occurs at  $R_0$ , where the probability density function reaches its maximum. This transition corresponds to the maximum absorption band. Other transitions, less probable, can start at  $R$  larger or smaller than  $R_0$  and contribute to the line width of the absorption band. The width of the absorption band depends on the spatial overlap of the two parabolas. A broader absorption band corresponds to a larger value of  $\Delta R$ . If  $\Delta R = 0$ , the two parabolas overlap and the absorption band becomes a narrow line. This transition is generally called zero-vibrational or no-phonon transition because no vibrations are involved.

The width of the absorption band informs us about the difference in bond lengths between the excited state and the ground state ( $\Delta R$ ). Usually, the terms weak and strong coupling are employed to indicate cases with small and large  $\Delta R$ . The value of  $\Delta R$  measures the strength of the interaction between the electrons and the vibrations of the center involved [55].

The shape of the absorption band, (i.e., narrow or broad) depends on the nature of the phosphor material. The absorption process can take place in the luminescence centers, i.e., activator ions or impurities, but may also occur in the host lattice. Also, the electronic interactions between the luminescent center and the host lattice have an influence in the absorption process. Considering a given luminescent center in different host lattices, the optical properties of the luminescent center will be different. It is important that the absorption of excitation light is not only related to the activator itself, but can also occur elsewhere. In general, the excitation of the activator ions is only possible with UV and/or visible radiation, whereas a wider range of excitation sources can be used.

After absorption, the system tends to return to the ground state with a combination of radiative and non-radiative emissions. These transitions are presented in the following sections.

### 3.3.5 Luminescence emission

As previously mentioned, absorption occurs in a broad optical band and brings the luminescent center into a highly excited state, combining electronic excitation and lattice vibration. After excitation, the system quickly relaxes to the thermalized state related to the temperature of the host lattice. From the respective vibrational level of the excited state, the center can return to the ground state by emission of radiation. The center then reaches a vibrationally-excited level of the ground state and subsequent relaxation thermalized the center with the surroundings.

This combination of radiative and non-radiative transitions is responsible for the color change between absorption and emission. The energy difference between the maximum of the absorption band and that of the emission band is called *Stokes shift*. Looking at the configurational diagram in Figure 3-3, the larger value of  $\Delta R$  corresponds to a larger Stokes shift since more energy needs to be released to the surroundings by non-radiative relaxation. In addition, the width of the emission bands increases with  $\Delta R$  for the same reasons to those discussed before for the absorption bands.

### 3.3.6 Non-radiative relaxation

After excitation, radiative processes are in competition with non-radiative relaxation. In the latter case, the entire absorbed energy is dissipated into the crystal lattice. Figure 3-4 shows three main pathways for non-radiative transitions that can be explained using configurational diagrams.

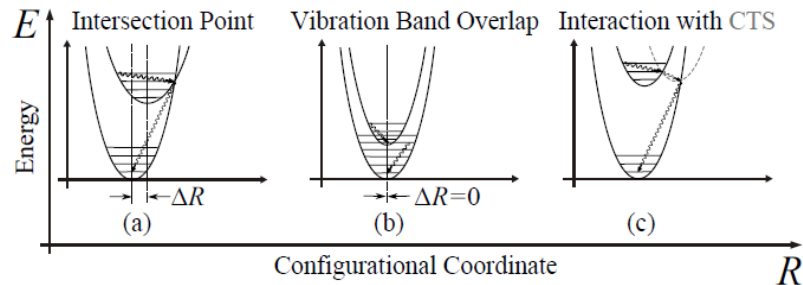


Figure 3-4: Non-radiative transitions: (a)  $\Delta R \neq 0$ : intersection between the ground state and the excited state potential, (b)  $\Delta R = 0$ : overlap of the low-energy vibrational levels of both the excited and the ground state due to a small energy gap between both states, (c) interaction with the charge-transfer state (CTS) potential, connecting the ground state and the excited state [51].

The two principal mechanisms for non-radiative relaxation found in phosphors are cross-over relaxation and multi-phonon emission, both of these processes are strongly temperature dependent. In the strong coupling case,  $\Delta R \neq 0$ , the excited and the ground state parabola may intersect in one point, Figure 3-4a. Via the intersection, the center can return to the ground state in a non-radiative manner. This is called cross-over relaxation and occurs if there is a significant spatial overlap between the lowest vibrational level of the excited state and those nearby of the ground state. This process accounts for the thermal quenching of the luminescence, since its probability increases with temperature and with  $\Delta R$ .

In Figure 3-4b, the two parabolas are in a weak coupling configuration and will never cross. In this case, non-radiative transitions can occur by the simultaneous excitation of several high-energy vibrational modes of the lattice. This non-radiative process, called multi-phonon emission, depends on the energy gap between the ground state and the excited state. The multi-phonon emission increases with temperature and decreases with the energy gap. This process is only important if the energy gap is less than about five times the highest vibrational frequency of the host lattice [55].

The third case is presented in Figure 3-4c: the ground and excited states are connected with a third potential, termed the charge-transfer state (CTS). In this case, both of the non-radiative processes described before are possible. The cross-over relaxation process is facilitated by the presence of the charge-transfer state. The probability of transition through CTS depends on both the temperature and the spatial position of the potential energy curves.

### 3.3.7 Energy transfer

Another possibility to return to the ground state without light emission is also possible. The absorbed energy of the luminescent center A can be transferred to another center B following the relationship



---

where  $A'$  corresponds to the excited state of the center A. The energy transfer may be followed by a radiative emission from  $B'$ . In this case, A is said to sensitize B and therefore is called sensitizer. Sensitizers are often added to the host material to increase the overall phosphorescence yield. If  $B'$  relaxes non-radiatively, B is said to be a quencher for A.

Energy transfer can occur between both similar and dissimilar luminescence centers. This process requires certain interactions between these centers. In case the energy differences between the ground and excited states of B and A are equal (resonance condition), a high transfer rate between these centers is possible. Other mechanisms facilitating the energy transfer are electric or magnetic multi-polar interaction [55].

Energy transition between similar luminescence centers can occur several times, allowing the absorbed energy to be transported far away from the original absorption center before emission. This process, called energy migration, is responsible of the so-called concentration quenching in phosphors. During this multi-step transfer, the excitation energy can reach a quenching site where it is released non-radiatively to the surroundings. Concentration quenching affects the luminescence efficiency of the phosphor. This quenching mechanism increases with the doping concentration because of the increased energy migration between similar centers. At low concentration, the luminescence increases with the number of luminescence centers. The maximum of the luminescence is related to a specific doping concentration, called quenching point [53,58]. After this point, the addition of more dopant ions does not increase the overall luminescence.

For more details about the luminescence processes involved in luminescent materials, the reader is referred to references [55,56]. An extensive treatment of inorganic phosphors can be found in [53] while in [58], a list of an important number of commercial phosphors is presented together with the description of their industrial applications.

### 3.3.8 Temperature effects

The mechanisms described in the previous sections consider a single luminescence center involved in the transitions between the ground and excited states. In practical cases, there are a large number of luminescence centers distributed in a solid. These centers are in thermal equilibrium and their electronic state population follows the Maxwell-Boltzmann distribution:

$$\frac{N_i}{N} = \frac{g_i e^{-\frac{E_i}{kT}}}{\sum_j g_j e^{-\frac{E_j}{kT}}} \quad (11)$$

where  $N$  is the total number of luminescence centers,  $N_i$  is the number of luminescence centers in state  $i$  with the energy  $E_i$  and the degeneracy  $g_i$ ,  $k$  is the Boltzmann constant, and  $T$  the temperature. At high temperature, higher vibrational levels are populated. After excitation and relaxation, the population of the excited state is distributed according the thermal energy of the host crystal. In the strong coupling case, as the energy levels close to the intersection point are densely populated, the probability of cross-over relaxation increases.

Temperature also affects multi-phonon emission. As the temperature increases, the higher vibrational modes of the lattice become populated, allowing stimulated emission of high-energy phonons, which increases the probability of multi-phonon emission [52,59].

### 3.3.9 Thermal response of the luminescence lifetime

A temperature increase causes the probability of non-radiative relaxation to become more significant and the luminescence quantum efficiency to decrease, according to Eq. (8). The increase in non-radiative transition rates corresponds to a faster depopulation of the excited state and therefore a shorter luminescence lifetimes, according to Eq. (7). The luminescence lifetime can decrease by several orders of magnitude over a wide range of temperature, i.e., the lifetime of  $\text{Mg}_4\text{GeO}_6\text{F}:\text{Mn}^{4+}$  changes from 3 ms at room temperature to below  $1\ \mu\text{s}$  at 1000 K [47]. A large variety of phosphors, showing different sensitivities to temperature can be found in the literature [2,4,60]. Figure 3-5, shows the temperature dependence of the luminescence lifetime of various phosphors.

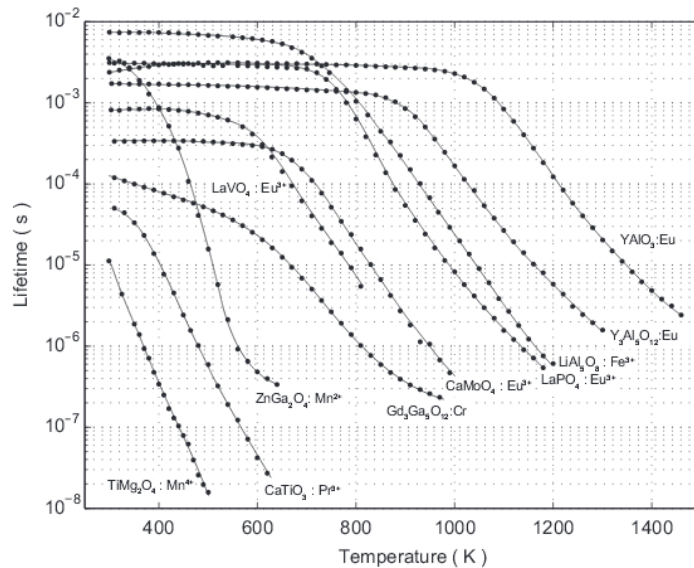


Figure 3-5: Temperature dependence of the luminescence lifetime characteristics of various thermographic phosphors [61,62].

Measuring the luminescence lifetime of the phosphor is a well-established technique to determine the temperature. Depending on the specific lifetime–temperature relationship and the temperature range, some phosphors are particularly suitable for this type of thermometry. When analyzing Figure 3-5, it must be kept in mind that the variation in lifetime is also correlated in a variation in signal intensity. Therefore, determining temperature variation over a larger temperature interval with a single phosphor has high requirements towards the dynamic range of the detection system when measuring lifetime and signal intensity.

### 3.3.10 Thermal response of the emission spectrum

Increasing the temperature can affect the emission spectrum of the activator ions in several ways:

- Broadening of linewidth due to lattice vibrations (phonons), which also reduce the radiative transition lifetime due to quenching
- Thermal expansion of the lattice creates larger ions separation, which can lead to a frequency shift, reducing the crystal field and reducing Stark component separation [63]

In some cases, light emission originates from transitions between two adjacent energy levels. An increase in the population of upper energy levels of the system, according to Boltzmann's law causes the spectrum to change: herein lies the relationship between temperature and the luminescence spectrum. This thermalization effect is described by Feist et al. [64] to explain a spectral emission method for the determination of the phosphor temperature considering two emission lines of YAG:Dy<sup>3+</sup>. The same effect can be found in the emission spectra of Y<sub>2</sub>O<sub>2</sub>S:Sm due to the similar arrangement of the energy levels of the activator ions [65]. This temperature measurement approach is in general referred to as *intensity ratio* approach.

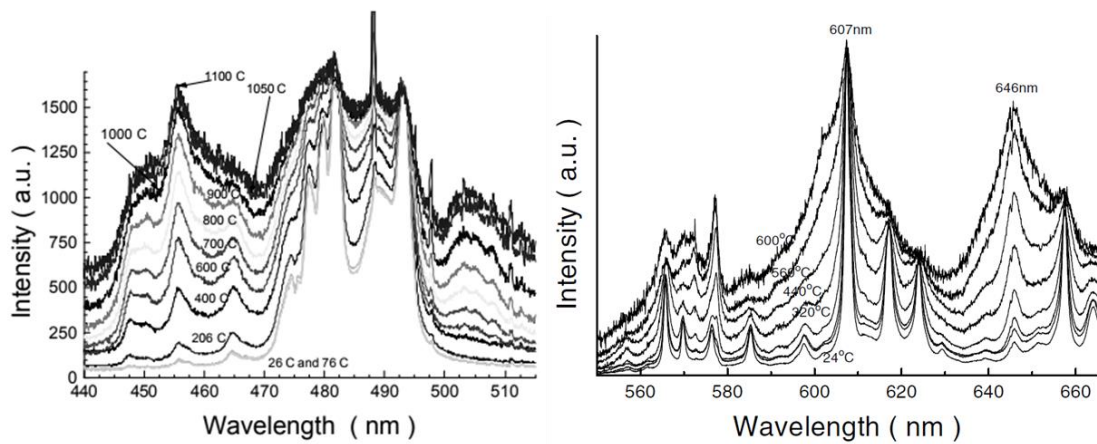


Figure 3-6: Emission spectra as a function of temperature. Left: YAG:Dy<sup>3+</sup> [64]; Right: Y<sub>2</sub>O<sub>2</sub>S:Sm [65].

Figure 3-6 shows the emission spectra of YAG:Dy<sup>3+</sup> and Y<sub>2</sub>O<sub>2</sub>S:Sm as a function of temperature. Other phosphors that have been reported to exhibit changes in emission band shape, i.e., YAG:Pr<sup>3+</sup> and YAM:Pr<sup>3+</sup>. YAG:Pr<sup>3+</sup> was used by Rothamer et al. to perform gas-phase imaging thermometry [66]. In this study, they applied the intensity ratio method from filtering the emission spectra at the two bands indicated in Figure 3-7, left. The measured intensity ratio obtained in that study has a non-monotonic response to temperature, as shown on the right hand side of Figure 3-7. The ratio increases from room temperature to 1100 K, followed by a decrease up to 1400 K, which disagrees with a Boltzmann distribution of the emitting states [3]. The temperature behavior of the emission spectrum of YAG:Pr, reported in Ref. [67], was further analyzed in Ref. [3]. The authors pointed out that the non-monotonic behavior of the ratio could be explained through a competition of two cross-relaxation processes between neighboring Pr<sup>3+</sup> ions [3].

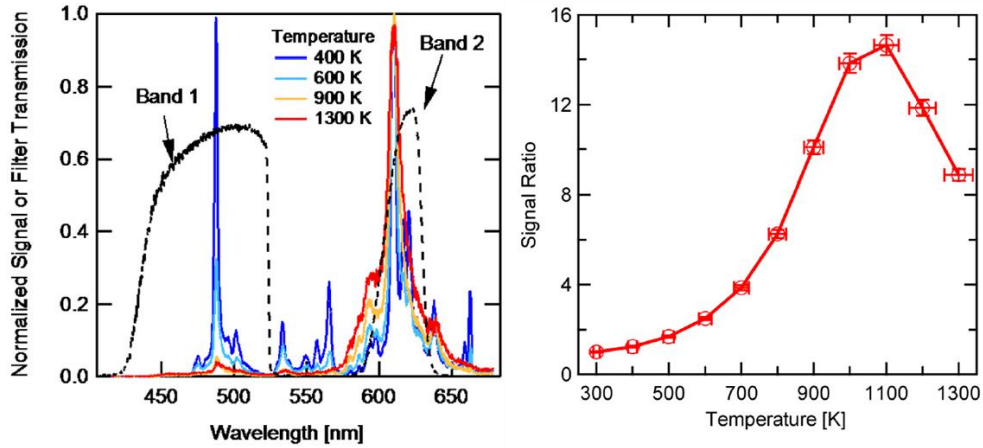


Figure 3-7: Left: Emission spectra at different temperature of YAG:Pr<sup>3+</sup>; Right: Corresponding intensity ratio between the two emission bands illustrated in the left graph [6,68].

Other mechanisms can be responsible of the shift and/or broadening of the emission bands, increasing with the temperature. In phosphors doped with Eu<sup>2+</sup>, emissions occur from transitions from the 4f to the 5d state (4f5d transition) [52]. With increasing temperature, the thermal dilation of the lattice reduces the crystal field acting on the Eu<sup>2+</sup> ion, producing a shift in the emission bands [52]. In addition, the coupling distance between the excited and ground states increases, and it results in a broadening of the emission spectrum. An example is the emission spectrum of BAM:Eu<sup>2+</sup> that shifts towards the UV and broadens with increasing temperature, as shown in Figure 3-8.

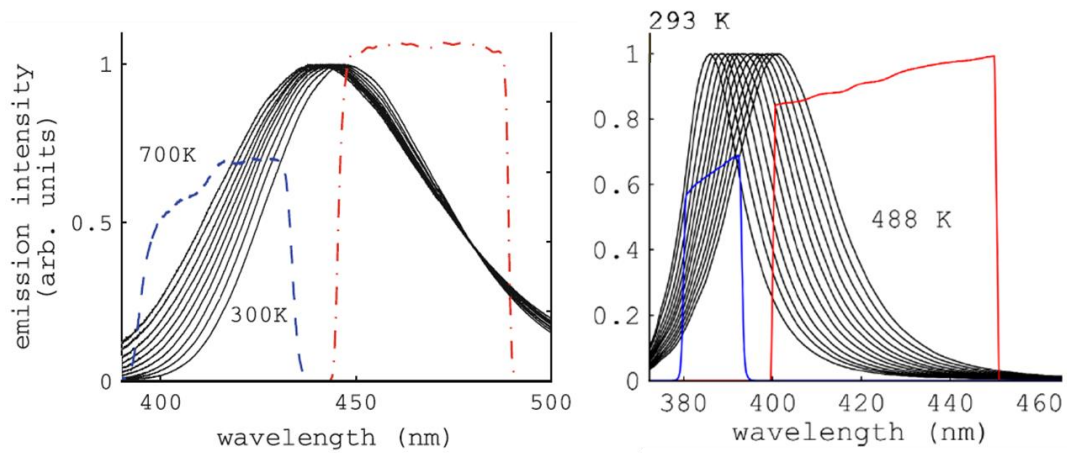


Figure 3-8: Normalized emission spectra for various temperatures for Left: BAM:Eu<sup>2+</sup> [69]; Right: ZnO [70]). Blue and red lines indicate the transmission filters used for the intensity-ratio method.

Similar behavior can be found in semiconductor materials that are used as phosphors for their luminescence properties. ZnO is a semiconductor that exhibits a shift in the emission band with increasing temperature, as shown in Figure 3-8. As the temperature increases, the band gap tends to decrease. As a consequence, the edge luminescence shifts to lower energy photons and therefore longer wavelengths.

Such spectral changes provide another way to measure temperature using phosphors. The techniques employed to take advantage of these luminescence properties for temperature measurement are discussed in the next section.

---

### 3.4 Phosphor thermometry strategies

As discussed above, the luminescence properties of thermographic phosphors are sensitive to temperature. So far, in real phosphors the photophysical processes involved are not yet fully understood and they are too complex for a model-based determination of the luminescence properties. As a consequence, the luminescence properties of the phosphors need to be characterized experimentally and a calibration process is required for quantitative temperature measurements.

There are several methods to infer phosphor temperature from its luminescence emissions. The two main methods found in the literature rely on different aspects of the emissions:

- *Luminescence lifetime*: The temperature is related to the luminescence signal decay following the excitation pulse
- *Intensity ratio*: The temperature is related to the relative change or shift of emission spectra

#### 3.4.1 Lifetime method

This method is based on the measurement of the luminescence lifetime of the phosphorescence emissions. Depending on the phosphor used, phosphorescence lifetime decrease of two or three order of magnitude when increasing the temperature, allowing very precise temperature measurements (Figure 3-9).

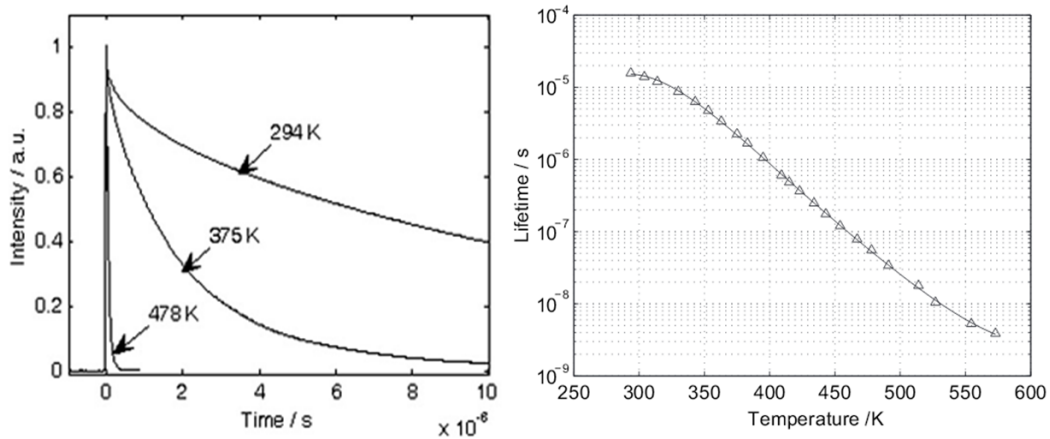


Figure 3-9: Left: Normalized PMT signals from CdWO<sub>4</sub> at 294, 376, and 478 K, corresponding to lifetimes of 15.8, 2.26  $\mu$ s, and 55.6 ns, respectively [4,4]. Right: Luminescence lifetime vs. temperature for CdWO<sub>4</sub> [71].

Generally, after a relatively short excitation pulse (e.g., laser pulse), the luminescence intensity decays in a characteristic way that depends on the phosphor temperature. This decay can be approximated to an exponential function:

$$I = I_0 \exp(-t/\tau) \quad (12)$$

where  $I_0$  is the initial intensity,  $t$  is the time, and  $\tau$  is the luminescence lifetime (defined by the decay of the signal intensity to  $1/e$ ). In this type of thermometry, the signal intensity, detected after the laser excitation, is recorded using a fast detector. The decay curve is then fitted using a single or a multi exponential function (e.g., Eq. (12)) to obtain a lifetime representative for the measured decay. This value, is then compared to calibration data to determine the temperature. Due to the many orders of

---

magnitude change in lifetime, this method is very sensitive within a specific temperature range. The advantage of a measurement in the time domain is that the experiment is less sensitive to the optical setup alignment compared to the intensity ratio method detailed below. This method is usually employed for point measurements using a photomultiplier tube (PMT) as detector but it has also been demonstrated for 2D imaging measurements using a high-speed camera. The frames of the camera distributed across the decay curve are recorded and the phosphorescence lifetimes are fitted to each pixel.

2D measurements were first demonstrated for surface measurements by Omrane et al. [72,73]. Wall temperature next to the propagating flame events have been studied using  $\text{Mg}_4\text{FGeO}_6:\text{Mn}$  as a thermographic phosphor and a framing camera with eight separated detectors at 100 MHz repetition rate. The resulting measurements, with a temporal resolution below 1 ms, show an accuracy and precision better than  $\pm 5$  K at temperatures between 680 and 780 K. Such a method is difficult to apply in turbulent flows because of the high time resolution required to resolve the flow motion ( $\mu\text{s}$  scale). For this approach two requirements are important: the choice of a phosphor with a lifetime that varies around the  $\mu\text{s}$  scale, and a high speed camera capable of operating at MHz range with a good spatial resolution.

The main limitations of the lifetime method are:

- a. The decay time should be long enough to be resolved by current camera technology. Considering minimum gating times of available cameras of about 100 ns and limitations of synchronization devices accuracy (10 ns), for accurate measurements the decay time should be at least 500 ns
- b. The lifetime of the phosphor in the expected temperature range, needs to be small when compared to the time scale of the temperature variations. Therefore, the measurement technique relies on the fact that the particle temperature remains constant during the decay time.

For the reasons listed before, at the moment, the 2D-lifetime approach covers a very limited range of temperatures with poor spatial resolution, due to the limited range for lifetime and intensity measurements.

### 3.4.2 Two-color intensity-ratio method

The intensity-ratio method for temperature measurements is based on the temperature-dependent changes in the emission spectra of a phosphor when considering a system with well-defined excited states and narrow transitions. After excitation, the measured phosphorescence signal is given by the following equation [4]

$$S_\lambda(T) \approx C_\lambda t_e \alpha_\lambda I \exp\left(-\frac{hcE_\lambda}{kT}\right), \quad (13)$$

where  $C_\lambda$  is the detection efficiency,  $t_e$  is the exposure time of the detector,  $\alpha_\lambda$  is the optical filter transmission,  $I$  is the laser pulse energy,  $h$  is the Planck constant,  $c$  is the speed of light,  $k$  is the Boltzmann constant and  $E_\lambda$  is the energy difference between two states. This equation is simplified by dividing the intensities of two different energy states

$$R(T) = \frac{S_\lambda(T)}{S_{\lambda+1}(T)} = \zeta I \exp\left(-\frac{hc\Delta E}{kT}\right), \quad (14)$$

---

where  $R$  is the signal ratio,  $\Delta E$  is the energy difference between the two excited states, and  $\zeta$  is a constant determined experimentally taking into account the features of the two collecting system. This method can be extended for 2D measurements by measuring the change of the emission spectrum using two different filters, chosen to include emission lines or spectral regions that exhibit different temperature dependence. After the superposition and division of the two images, an intensity-ratio map is obtained that can be translated in a temperature map.

Usually, two detectors are used for the collection of two images of the same object. In this case, the resulting ratio from the division of the two images needs to be corrected by

$$R_{i,j} = \frac{I_{i,j}^1 - B_{i,j}^1}{Ref_{i,j}^1 - B_{i,j}^1} \frac{Ref_{i,j}^2 - B_{i,j}^2}{I_{i,j}^2 - B_{i,j}^2}, \quad (15)$$

where  $I$  denotes the phosphorescence intensity at pixel location  $i, j$ .  $B$  and  $Ref$  are the background and reference intensity images. Background images take into account the contribution of light sources others than the luminescence from phosphor particles. In general, the background image is taken with the laser pulse but without particle seeding, allowing to take into account surface scattering or others sources of interference. The reference image also referred to as flat field image and it is needed to correct for spatial non-uniformity in light collection efficiency.

This equation allows correcting the different sensitivity and the spatial non-uniformity introduced by the detectors in order to obtain high accuracy and precision. This method has been used for temperature measurements on surfaces and in sprays [74–76]. For example, Brübach et al. [70,75], opted for this method for temperature imaging measurements in a gasoline-type spray using  $Mg_4GeO_{5.5}F:Mn$  phosphor particles (8  $\mu m$ ) dispersed in n-dodecane with different initial fuel temperatures. A 266 nm excitation source was used with an ICCD camera coupled with stereoscope optics and each channel with a different band pass filter. The resulting measurements were then exploited to determine the temperature field. The camera exposure was set at 1 ms starting 1  $\mu s$  after the laser pulse to avoid the detection of fluorescence from the fuel. Calibration measurements were performed in an optically-accessible liquid tank. As expected, with increasing fuel temperature, an increased spray temperature was observed.

In general, the color-ratio method enables 2D imaging measurements with cheaper instruments compared to the lifetime method (that would require a high-frame-rate camera). The main aspect to be taken into account is the signal-to-noise ratio (SNR) over the two channels, which determines the accuracy and precision of the measurements. This aspect will be discussed later in more detail because the intensity-ratio method will be employed in the experiments performed in this work.

### 3.5 Choice of phosphor

A large number of thermographic phosphors have already been well characterized for surface thermometry. The sensitivity to temperature, in terms of lifetime decay and spectral intensity ratio, is presented in Figure 3-10 for most of the available phosphors [4]. This overview is useful for the choice of a phosphor for specific applications, considering first of all, the thermometry method used. In Figure 3-10, the solid blue lines indicate the dependence of the luminescence lifetime on temperature (left hand side y-axis) while the dashed lines show the temperature dependence of the two-color intensity ratio (right

hand side y-axis). The lifetime shows a strong dependence on temperature with changes by several orders of magnitude over few hundred K, which is a much stronger dependence than that provided by the spectral intensity ratio. On exception, however, zinc oxide exhibits a strong temperature sensitivity of the intensity ratio.

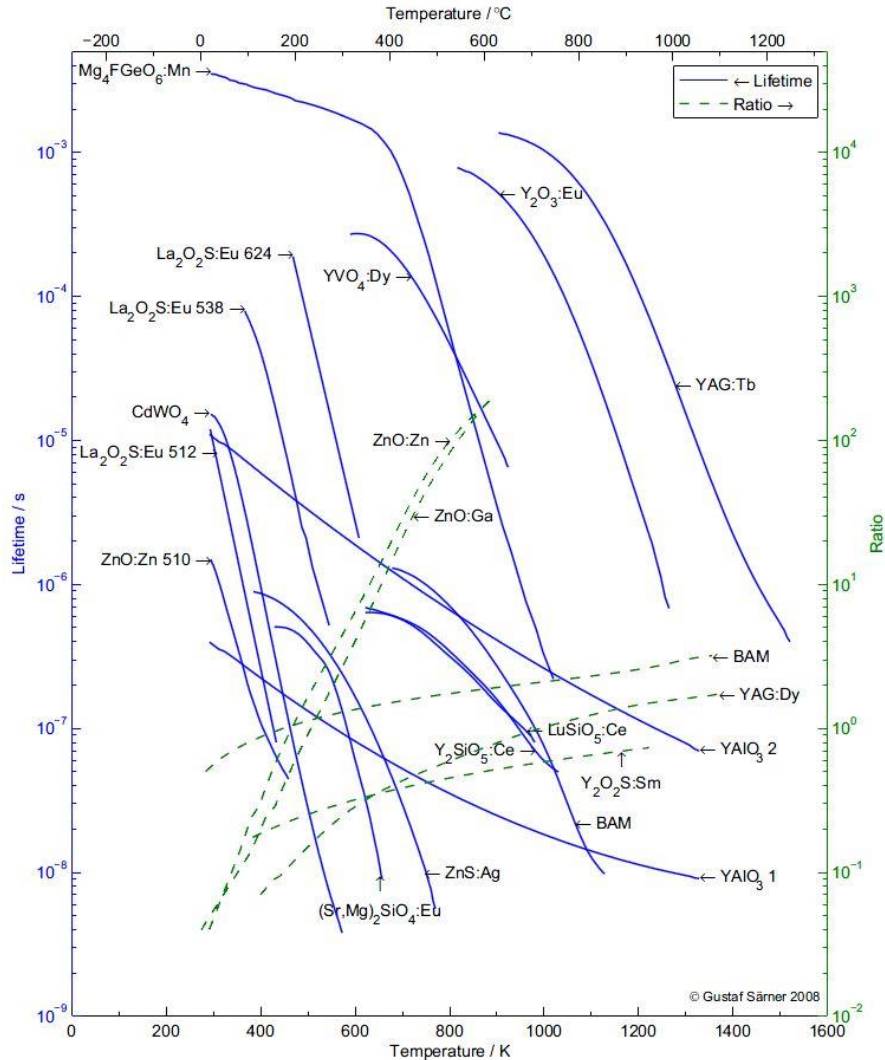


Figure 3-10: Temperature sensitivity for some phosphors used for surface thermometry. Solid lines show the luminescence lifetime, the dashed lines the intensity ratio as a function of temperature [4,71] .

The main criteria for choosing a thermographic phosphor are:

- I. Sufficient temperature sensitivity over the temperature range of interest. It is obvious that the measurement precision strongly depends on the temperature-dependence of the respective quantity of the phosphor
- II. For gas-phase applications, small phosphor particles are required to be capable of following the flow
- III. In turbulent and high-velocity gas flows, the time scale of measurements must be limited to a few microseconds to prevent significant displacement of the particles within the measurement interval (e.g., BAM:Eu<sup>2+</sup>, ~1 μs or ZnO, ~1 ns) The measurement interval is determined by

---

either the exposure time or the phosphorescence lifetime, whichever is shorter, therefore, the temporal resolution of the measurements can be reduced to resolve fast fluctuations.

- IV. To avoid the interference from background signal it is preferable to choose a phosphor with short lifetime and strong phosphorescence emission. For high temperature applications, it is also preferable to use phosphors that emit in the blue or ultraviolet (UV) wavelength to minimize the spectral interference from black-body radiation [4].

### 3.6 Overview of applications

The feasibility of simultaneous temperature and velocity measurements using thermographic phosphors has been investigated and demonstrated by Fond et al. [52,77]. Single-shot and averaged imaging measurements of a turbulent heated jet have been studied by Fond et al. [77]. In the 450–600 K range, they found a measurement accuracy of 2% and a precision between 2 and 5%. In these studies, BAM:Eu<sup>2+</sup> phosphor particles (2 μm) were used and excited at 355 nm (100 mJ/cm<sup>2</sup> fluence) for thermometry. Double-pulse 532 nm laser radiation was used for PIV. The luminescence of the particles was detected by two cameras with a beam splitter arrangement to exploit the spectral-intensity-ratio method. In this work, non-intensified cameras were used. The exposure time was set at 5 μs allowing the collection of the entire phosphorescence lifetime (approx. 1 μs). The temperature calibration was performed in a heated jet operated in steady state condition, by measuring the temperature with a thermocouple centered in the imaging plane.

Instantaneous temperature and velocity fields were obtained for the turbulent heated jet. The single-pixel temperature precision was also measured from 600 measurements at steady jet temperature. A precision of 16 and 33 K at 483 and 683 K, respectively, was found in this study.

This technique was used by Abram et al. for the investigation of unsteady heat transfer phenomena in the wake of an heated cylinder at 3 kHz repetition rates [78]. The air flow was seeded with 2.4 μm BAM:Eu<sup>2+</sup> phosphor particles, at 293 K temperature and 1.6 m/s velocity field. A heated pipe (6.25 mm diameter,  $T = 530$  K) was positioned horizontally and crossed the flow. The laser sheets intersected the flow perpendicular just above the heated pipe. The detection system was positioned normal to the light sheet. Three high-speed CMOS cameras were used in this study to capture temperature and velocity fluctuation. Two cameras were used to exploit the thermometry and the third one was used for PIV measurements. For further information about this technique the reader is referred to the review paper published by Abram et al. [3].

Few applications of this technique in IC engines have been found in the literature. Hasegawa et al. [5] employed this technique for the first time to investigate in-cylinder temperatures in an HCCI mode operated engine. Dy:YAG phosphor particles (4 μm) were used to measure the in-cylinder gas temperature. The particles were seeded into an optical Diesel engine (bore: 82.2 mm, stroke: 94 mm) running in HCCI mode at 1200 rpm. The engine was modified with a port-injection system to enable working with iso-octane/n-heptane fuel blends. The compression ratio (CR) and intake temperature were 12.2 and 363 K, respectively. The fuel/air equivalence ratio was 0.26. The laser sheet (355 nm, 80 mJ/pulse, 10 Hz) propagated horizontally through the cylinder via a full fused-silica ring. The temperature images of the vertical plane were collected with an ICCD camera coupled with a stereoscope. The camera exposure time was set to 100 μs, previously determined as suitable from lifetime measurements of the

---

same phosphor. The measurements were acquired at different timings during the engine cycle. The intensity ratio method was used to determine the temperature and the temperature calibration was previously carried out in a heated test cell on a metal rod coated with a layer of phosphor particles. Good agreement was found between the spatially-averaged temperatures evaluated from the measurements and the calculated average temperature based on the pressure trace. Single-shot temperature images show local temperature gradients with peaks temperature of 1100 K. The authors associate these fluctuations to the turbulent heat exchange with the boundary layers. Unfortunately, the single-shot pixel-to-pixel precision and the spatial resolution of these measurements are not reported in the paper. Also, authors were unable to obtain reliable temperature data near the TDC (between  $-15$  and  $15^\circ\text{CA}$ ), due to the interference produced by combustion-based luminescence at the long camera exposure time (100  $\mu\text{s}$ ). For these conditions, a phosphor with a shorter lifetime could have help to extend the measurements nearer to the combustion zone. The reliability of the measurements was also altered by damages caused by particles on the engine sealings after few hours of operation.

Phosphor thermometry imaging was also employed by Takada et al. to investigate the mixing processes in a Diesel engine [7]. The engine was equipped with a direct injection system injecting either n-heptane or iso-octane fuels. Injection start was phased at  $3^\circ\text{CA}$  BTDC while the engine was operated at 1200 rpm with  $\text{CR} = 13.2$  and intake temperature of 368 K.  $\text{BAM:Eu}^{2+}$  and  $\text{YAG:Dy}^{3+}$  particles (4  $\mu\text{m}$ ) were seeded into the engine as tracers to measure the temperature in the vertical plane intersecting the piston bowl axis, made of fused silica. The phosphor particles were excited with 355 nm Nd:YAG laser, and the phosphorescence was captured with an ICCD camera coupled with a stereoscope. Appropriate filters for each phosphor were used to exploit the intensity ratio method to determine the temperature. The temperature calibration was obtained from coated surface measurements in a heated test cell.

Temperature distributions in the piston bowl were obtained using  $\text{YAG:Dy}^{3+}$  under motored conditions. Under this condition, lower temperature regions located in the spray area, were observed. The authors attributed the temperature gradient to the spray mixing process coupled with heat transfer phenomena. Measurements in fired conditions were also presented. However, measurements were only possible up to TDC due to the strong luminescence from combustion. In this study,  $\text{BAM:Eu}^{2+}$  with a short luminescence lifetime was employed to reduce the background interferences. However, no results with this phosphor were presented [7]. It was also mentioned that the phosphor particles seeded into engine tend to stick on the engine walls, causing strong background interference. This issue was relieved by using  $\text{SiO}_2$  nanoparticle coated phosphor particles [7].

Recently, Neal et al. used  $\text{YAG:Pr}^{3+}$  particles (1.8  $\mu\text{m}$ ) for simultaneous temperature and velocity measurements in a Diesel engine [6]. The engine had a bore of 82 mm with a stroke of 76.2 mm and a  $\text{CR}$  of 12.3. It was operated at 1200 rpm with two different intake temperatures of 303 and 383 K. A 266-nm laser sheet was used for excitation of the phosphor combined with a double-pulse 532 nm laser for PIV. The laser sheets were directed horizontally through the liner windows and the phosphorescence and scattering signals were collected through a flat sapphire piston. The detection system was equipped with two ICCD cameras and a 50/50 beam splitter. A third camera, was used to collect Mie scattering images for PIV measurements. The temperature calibration was performed using the same detection system and measuring the luminescence of phosphor powder in a furnace.

High spatial resolution of the temperature and velocity fields was measured under motored conditions between 80 and  $30^\circ\text{CA}$  BTDC. The resulting spatial resolution was measured by imaging a 1951 USAF

---

target placed in the measurement plane. The final resolution was between 2–3 pixels, corresponding to 0.5 to 1 mm in the measurement area.

Less than 5% difference between the calculated average temperature based on a 0D model with adiabatic compression and the spatially-averaged temperature obtained from the measurements. Under these conditions, the in-cylinder temperature is supposed to be homogeneous, therefore a good accuracy of the calculated temperature is expected. Again, it was not possible to measure nearby the TDC due to the interference of the luminescence of particles sticking on the piston window.  $\text{Al}_2\text{O}_3$  nanoparticles were mixed with the  $\text{YAG:Pr}^{3+}$  particles to improve the seeding process by reducing particle agglomeration and thus to generate a homogeneous particle distribution. It was also noted that a certain minimum seeding density of 15 particles per interrogation region was required for the measurements; too high seeding densities, however, generated strong background signal from particles deposited on surfaces. All the publications discussed here, reported complications caused by particle deposition on the combustion-chamber walls. Particle deposition increases the background signal intensity. The deposited particles are directly or indirectly excited and the following luminescence affects the accuracy of the measurements. Also, the publications show that the choice of phosphor is extremely important. More precisely, it is preferable to choose a phosphor with a short luminescence lifetime, and a high luminescence quantum yield to allow discrimination against background luminescence (e.g., chemiluminescence and soot luminescence), and a high temperature sensitivity to enable precise measurements.

### 3.7 Engine applications: Potentials and challenges

In order to improve efficiency at lower fuel consumption and to reduce pollutant formation, modern IC engines employ novel combustion concepts usually near the limits of stable combustion. HCCI combustion, for example, is an effective way to attempt these requirements. In HCCI engines, fuel and air are premixed and the lean mixture is compressed to initiate auto-ignition. Because of the diluted mixture, the temperatures reached during the combustion are low, resulting in low  $\text{NO}_x$  concentrations and, since the mixture is homogeneously lean, soot formation is prevented [1]. However, this combustion strategy is limited to low-load operating conditions. This limitation is mainly due to the lack of control on the combustion phasing and the need to limit the pressure rise rate. The in-cylinder pressure-rise rate (PRR) increases with increasing equivalence ratio. At high-load, the PRR becomes so important that the acoustic oscillations induce excessive noise and engine knocking and might even damage the engine.

In HCCI engines ignition is determined by the chemical kinetics reaction rates of the mixture, which is controlled by time, temperature, and local mixture composition. Previous studies have shown that the temperature stratification of the mixture during compression affects the combustion-phasing and the PRR, offering a way to control knocking and damages in HCCI engines [1]. However, thermal stratification is governed mainly by turbulence flow and wall heat transfer effects, varying from cycle to cycle. A better understanding of these in-cylinder processes is needed to bring new combustion concepts to market. Measurements of the local temperature and velocity gradients near the end of compression are required to provide further insight and build predictive engine simulation models.

Current applications of temperature-velocity imaging diagnostics are limited to motored conditions, running with nitrogen [43–45]. Toluene LIF has been largely used to investigate the temporal evolution of the thermal stratification in optical accessible HCCI engine [41,79]. Only measurements up to 550 K

---

have been demonstrated due to the strong reduction of the toluene-LIF signal with temperature. In addition, this tracer is consumed by chemical reactions during the onset of combustion. Thermographic PIV based on phosphor particles is presented here as a new promising technique for simultaneous temperature and velocity measurements in IC engine. Phosphor particles could be used for investigations in fired condition, allowing measurements in fresh and exhaust gases. No quenching is expected, and particles are chemically resistant and survive to combustion [80–82]. This is particularly useful for the investigation of complex in-cylinder processes such as fuel/air mixing, thermal stratification, heat and mass transfer phenomena.

Previous applications of phosphor thermometry for gas-phase measurements in IC engines showed the main challenges of this novel technique:

- I. Selective signal detection: Suppression of interference from, e.g., flame luminescence, multiple scattering of signal. Reflections can be reduced using low reflectivity paint. Another approach is based on the application of a thin layer of soot from a rich diffusion flame before each measurement run.
- II. Laser scattering: The laser path into engine also needs to be carefully considered. A laser sheet dumped on the engine walls must be avoided in order to reduce a lot of scattering generating significant background signals.
- III. Particle deposition: Particle deposition on surfaces is a challenge when particles are seeded into a confined environment. This effect must be controlled to prevent signal contributions from unwanted locations. Particle deposition affects the gas temperature measurement near the wall. Because on the accumulation of particles on the wall (with a density much higher than in the gas phase) even weak scattered laser light can cause significant signal contributions.
- IV. Seeding system: Robust and reliable measurements require homogeneous and uniform seeding of particles with a controlled (optimized) and reproducible seeding density.
- V. Choice of phosphor: A compromise needs to be found between temperature sensitivity, signal intensity, luminescence lifetime, wavelength, and particles size. Additionally, particles must survive the combustion environment to allow for in- and post-flame measurements. A suitable candidate for engine measurements must have high temperature dependent emission spectrum, high quantum efficiency and a short lifetime.
- VI. Engine damage caused by particles: Seeding solid particles into an engine can cause serious damage to mechanical parts. Additionally, the optical access of the engine, generally made of fused silica, shows premature wear due to contact with particles. Hasegawa et al. mentioned that also sealings were damaged after a few hours of operation.
- VII. Calibration: the spectral response of the phosphor was found to depend on the specific conditions (fluence, number density, multiple scattering effects) showing the need to calibrate in similar condition and in particular in the gas phase at similar number density

## 3.8 Approach of the thesis

### 3.8.1 Specific objectives

---

The primary objective of this research is to investigate the application of simultaneous temperature and velocity measurements in IC engines using thermographic phosphors. This technique combines two laser-based diagnostics. The works found in the literature show clearly that this technique still needs development for its application in (IC) engines and some issues need to be resolved. In terms of velocity but also temperature, there are significant differences between Diesel and spark-ignition engines. Based on the literature review presented in the previous sections, a research strategy has been defined aiming at improving PIV-thermometry. More specifically, four major objectives have been identified:

- a. Identification of more suitable phosphors for engine experiments
- b. Development of a new characterization measurement system for aerosolized particles
- c. Characterization of phosphor materials for gas-phase measurements
- d. Selection and application of a phosphor in an engine to simultaneously detect temperature and velocity distributions under realistic operating conditions
- e. Development of a measurement methodology suitable for IC engines: determination and optimization of measurement accuracy and precision

### 3.8.2 Research methodology

In order to attempt the specific objectives listed before, a precise research methodology was adopted in this work. The initial stages of the research were dedicated to the selection of phosphor materials. The objective was to follow previous studies and employ phosphor materials already reported and successfully tested selecting three phosphor candidates. The next step was dedicated to the characterization of phosphors under controlled conditions. For this purpose, two characterization setups with different aims were built in this work. The first setup was based on phosphor-coated surface measurements in a well-controlled test cell. A qualitative approach was used in this part to screen and compare the different phosphor candidates. Afterwards, a second setup was developed, aiming at characterizing phosphor particles dispersed in aerosol. Here, a quantitative approach was used to determine accurate temperature calibration to be applied to engine measurements. All these topics are presented and discussed in the Chapter 4 of this thesis. Afterwards an experimental campaign was performed in the optical accessible engine available at IFPEN, applying the thermography PIV measurements under different test conditions. The optical setup, the results obtained and the evaluation of experimental precision and uncertainty analysis are presented in Chapter 5.

---

---

---

## 4 CHARACTERIZATION OF PHOSPHOR PARTICLES

In this chapter, the instrumentation and the methodology used for characterization and calibration of the phosphors is described together with the results obtained. The experimental arrangements are presented followed by a discussion on the relevant parameters that affect the measurement accuracy. The materials are characterized by spectrally-resolved measurements of both phosphor-coated surfaces and aerosolized particles. The latter characterization is intended to be more representative of the engine application. The luminescence and intensity-ratio response of phosphor particles to various parameters including temperature are measured resulting in a temperature-dependent calibration curve to be used in engine experiments. To assess the influence of experimental parameters, the particles were characterized performing parametric variations in term of seeding density, impact of the laser fluence and temperature.

### 4.1 Phosphor selection

The choice of phosphors tested was directed by the state-of-the-art of this technique. Previous applications in engines have shown a good potential but also some challenges linked to the choice of phosphors. The most promising phosphors were chosen based on the recent work by Fond et al. and Abram et al. [69,70]. Three commercially available phosphors were selected and further characterized in this work: BAM:Eu<sup>2+</sup>, ZnO and ZnO:Zn. A brief description of these phosphors is given below.

#### 4.1.1 BAM:Eu<sup>2+</sup>

Europium-doped barium magnesium aluminate (BAM:Eu<sup>2+</sup>) is a blue-emitting phosphor with a high quantum yield. Its luminescence properties are governed by 4f<sup>6</sup>5d → 4f<sup>7</sup> transitions of Eu<sup>2+</sup> [69]. BAM:Eu<sup>2+</sup> can be excited with UV radiation at 355 nm. This results in broadband emission centered at approximately 440 nm. The host lattice interactions taking place result in a temperature dependence of the phosphorescence spectrum, as shown in Figure 3-8. As the temperature increases, the emission band broadens and shifts towards the blue. This phosphor is thus suitable for thermometry using the intensity-ratio approach. In addition, the temporal emission response displays a temperature sensitivity over 700–1150 K, with luminescence lifetimes between 1 μs and 10 ns [69]. Some degradation occurs when the particles are exposed to temperatures above 700 K for 150 min [83]. However, the experiments conducted by Lipzig et al. show that BAM:Eu<sup>2+</sup> is able to resist higher temperatures for short periods of time without significant alteration of its luminescence properties [80].

#### 4.1.2 ZnO and ZnO:Zn

Zinc-oxide phosphors are direct band-gap semiconductors with a broad absorption spectrum at room temperature. This features allows to be easily excited with standard frequency-tripled Nd:YAG lasers (355 nm). The corresponding emission spectrum shows fast (few nanoseconds) UV emission around 387 nm and a slower broadband emission centered at 510 nm. Due to the significant temperature sensitivity, the UV emission peak at 390 nm is often used for thermometry purpose using intensity ratio method, as shown in Figure 3-8 (right). The broad emission at 510 nm can be used for thermometry using the lifetime method as shown in Figure 3-10.

Different kinds of zinc-oxide phosphors are available, however, previous applications for thermometry purpose have employed mainly zinc-oxide doped with zinc (ZnO:Zn) and gallium (ZnO:Ga). The red-shift of their UV luminescence with increasing temperature was previously exploited for surface temperature measurements using the intensity-ratio method [84]. Recently, ZnO was used for flow thermometry achieving high precision [70,85].

ZnO:Zn consists of a zinc oxide crystal with occasionally missing oxygen atoms that have been replaced by zinc atoms in the lattice structure. This is generally obtained by exposing ZnO material to a reducing atmosphere at high temperature to promote the formation of oxygen vacancies and to lead to an excess of zinc atoms in the crystal lattice.

The emission spectra of both phosphors show similar bandwidths but different peak center positions. Compared to ZnO, ZnO:Zn phosphor shows a second emission peak on the UV side of the spectrum and the peak center is shifted by 2.5 nm toward the visible light [70]. Also, some variations of the emission spectrum can be detectable from different production batch of the same ZnO:Zn due to the presence of impurities and a not-well controlled dopant concentration. These differences might affect the spectral shape as well as the emission temperature dependence. An overview over the main properties of these phosphors is presented in Table 4-1.

Table 4-1: Main properties of the phosphor materials used in this work for surface and gas-phase measurements.

Type of phosphor	Emission lifetime	Excitation wavelength / nm	Detected spectral lines/region / nm	Particle size / $\mu\text{m}$	Filters used for thermometry /nm
<b>BAM:Eu<sup>2+</sup></b>	1 $\mu\text{s}$	355	450	4	458 $\pm$ 6 400 $\pm$ 20
<b>ZnO:Zn</b>	< 1 ns	355	390	3.5	425 $\pm$ 15 387 $\pm$ 11
<b>ZnO</b>	< 1 ns	355	387	2	425 $\pm$ 15 387 $\pm$ 11

## 4.2 Characterization of phosphors on coated surfaces

### 4.2.1 Experiment

The experiments were performed in a high-temperature cell with optical access, allowing spectrally-resolved measurements of the phosphor coating emissions, under well-defined temperature conditions, Figure 4-1. With this cell it was possible to characterize the optical properties of phosphor coatings at temperatures up to 900 K in a confined temperature-controlled environment.

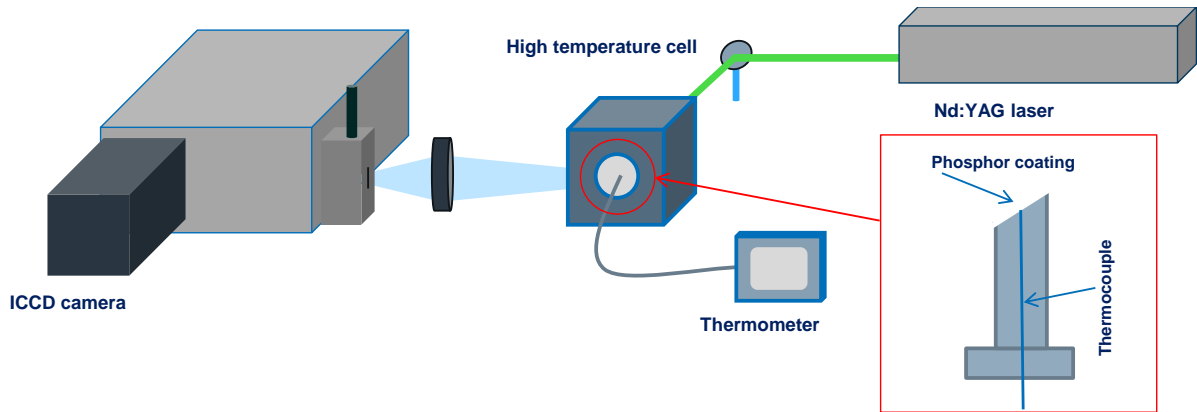


Figure 4-1: Experiment for spectroscopic measurements on phosphor-coated surfaces.

The investigated phosphors were blended with a specific binder and then sprayed on a metal surface to form a thin and homogeneous coating. The metal support was then placed in the high-temperature cell for the characterization. The samples were excited at 355 nm using the third harmonic of a 10 Hz Nd:YAG laser. The laser pulse energy was controlled via a polarizing beam attenuator coupled and detected with a power/energy meter (FieldMaxII-TOP, Coherent). The Gaussian profile of the laser beam was transformed into a uniform top-hat profile using a beam homogenizer. This was useful for an accurate study of the dependence of the phosphorescence emission on the laser fluence.

A spherical lens of 300 mm focal length was used to focus the phosphorescence emission into a spectrometer. The emission spectra were measured using a 300-mm focal length,  $f_{\#} = 4$  spectrometer (Acton SP-300, Princeton Instruments, 300 g/mm grating) coupled with an ICCD camera (PI-MAX, Princeton Instruments). The exposure time was set at 2  $\mu\text{s}$ , enough to collect the entire phosphorescence decay. The entrance slit width was set to 300  $\mu\text{m}$  corresponding to a spectral resolution of 1 nm, determined using a mercury lamp. The transmittance of the entire system was measured using a calibrated integrated sphere coupled to a tungsten lamp.

A K-type thermocouple was used to control the temperature of the coated surface during the measurements. The junction of the thermocouple was located in the center of the metal support, held in contact with the coating surface.

The investigated phosphors were coated on stainless metal part, using a chemical binder (HPC, Zyp-coatings), as shown in Figure 4-2. The HPC-binder is a water-based binder composed of magnesium aluminum silicate. Coatings produced with this binder dry at room temperature in few minutes and can handle temperatures up to 1500°C [86]. The binder and the phosphor powder were mixed together to obtain a uniform homogeneous paint. For one volume of binder, 20% volume of phosphor was added. The paint was then sprayed on the surface by an air-brush. Each coating was dried using a heat gun to prevent chemical reactions between the water contained in the binder and the metal surface. Several layers were deposited to generate a homogeneous and reproducible coatings with a thickness of 10–15  $\mu\text{m}$ .

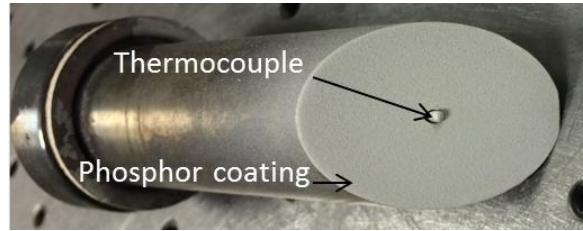


Figure 4-2: Example ZnO:Zn coating using a chemical binder and deposited on the surface by an air brush.

#### 4.2.2 Laser fluence effect

The influence of the laser fluence on the phosphorescence emission was investigated by varying the laser pulse energy during the recording of the spectral emission. For each laser fluence tested, the average of 50 samples was performed. This experiment was performed at 294 K room temperature and with fluences between 0.45 and 10 mJ/cm<sup>2</sup>. The emission intensity was calculated by integrating the emission spectrum over the emission wavelength.

The results for BAM:Eu<sup>2+</sup> are shown in Figure 4-3. The emission intensity increases linearly with the laser fluence until 2 mJ/cm<sup>2</sup>. Above 2 mJ/cm<sup>2</sup>, the emission intensity rate with laser fluence slowly decreases until 10 mJ/cm<sup>2</sup>. This phenomenon, referred as saturation, limits the luminescence emission intensity. The same behavior was earlier observed by Fond et al. [57].

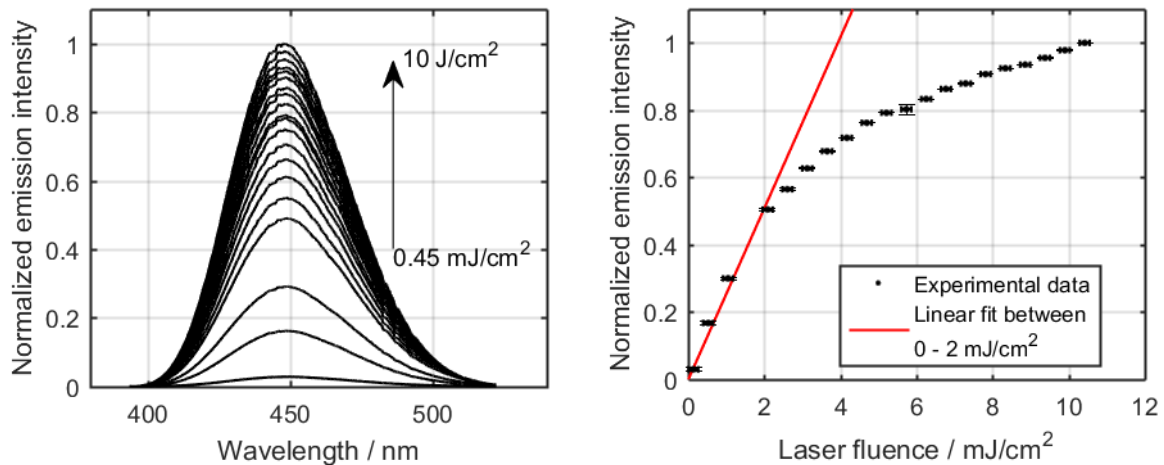


Figure 4-3: Fluence-dependence of the emission spectra (left) and the band-integrated emission intensity (right) of BAM:Eu<sup>2+</sup> at 294 K relative to the values at the maximum laser fluence (10 mJ/cm<sup>2</sup>). The error bars show the standard deviation obtained over 50 samples.

The influence of these observations on the intensity-ratio method were investigated. The intensity ratio was evaluated by convoluting the emission spectra with the transmission curve of the interferences filters centered at 400±20 nm and 458±6 nm. A weak dependence of the intensity ratio on the laser fluence was observed up to 10 mJ/cm<sup>2</sup> (Figure 4-4).

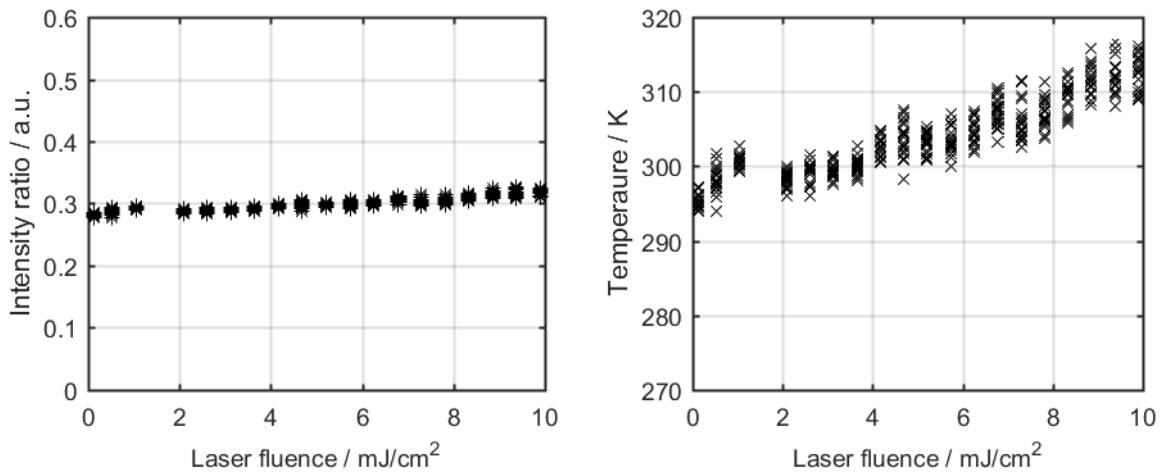


Figure 4-4: Intensity ratio as a function of laser fluence for BAM:Eu<sup>2+</sup>. The intensity ratio is obtained by applying the convolution of the emission spectra with the filters indicated in Table 4-1 (left). The measured temperature as a function of laser fluence (right). A set of 50 samples are presented here for each laser fluence.

The intensity ratio, presented in Figure 4-3, increases by  $\sim 7\%$  in the measured fluence range. Considering the ratio sensitivity to the temperature, which will be presented later in Section 4.6, the observed modification of the spectrum causes a deviation of about 20 K in the temperature calculation. It is not clear what the origin of this deviation is and two main hypotheses are drawn. The first is that the laser fluence has an impact on the surface temperature and therefore the variation in the ratio measured corresponds to an actual increase in surface temperature. The second is that this deviation is related to a modification of luminescence properties due to the increased laser fluence. In particular it can be related to the saturation effect observed in Figure 4-3. The comparison between the effect of the laser fluence and the effect of a temperature variation on the emission spectrum is presented in Figure 4-5. The difference in the shape between the spectrum obtained with higher fluence and the one obtained at +20 K suggests the saturation hypothesis is probably to be preferred.

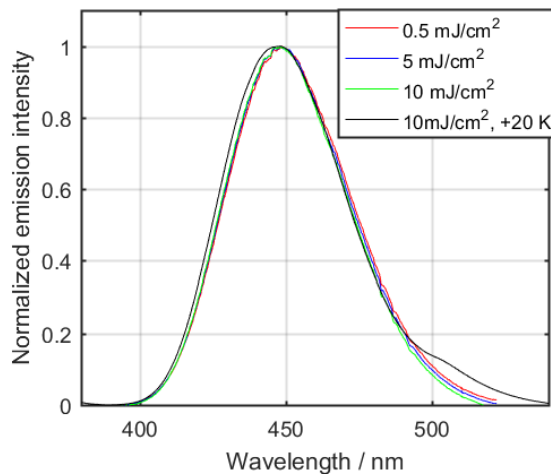


Figure 4-5: Comparison between the effect of the laser fluence and the effect of a temperature variation on the emission spectrum for BAM:Eu<sup>2+</sup>.

A similar saturation behavior was also observed for the ZnO emission spectra. Figure 4-6 shows the fluence-dependence of the emission spectra. The emission intensity increases linearly with the laser fluence up to 5 mJ/cm<sup>2</sup>. Above this value, saturation affects the linearity.

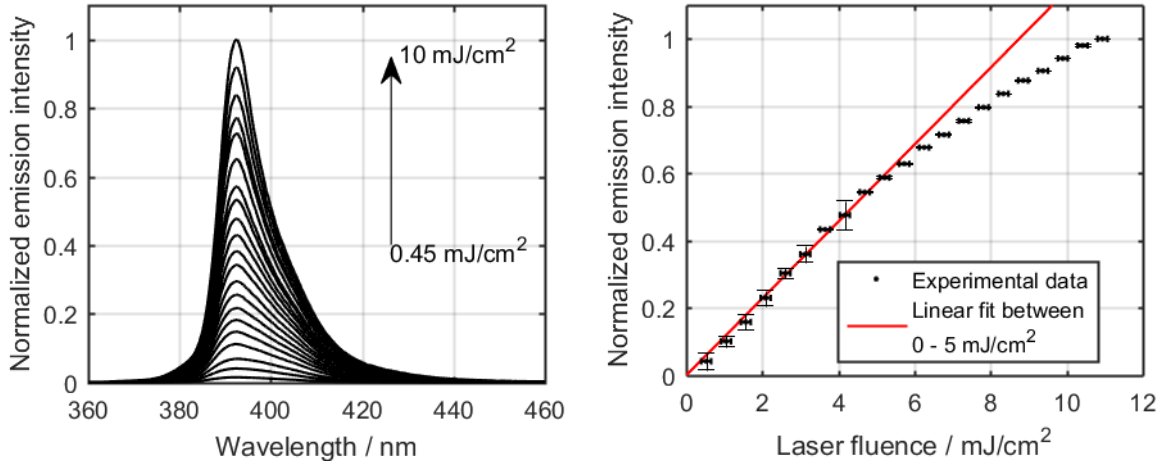


Figure 4-6: Fluence-dependence of the emission spectra (left) and the band-integrated emission intensity (right) of ZnO at 294 K relative to the values at the maximum laser fluence (10 mJ/cm<sup>2</sup>). Error bars show the standard deviation obtained over 50 samples.

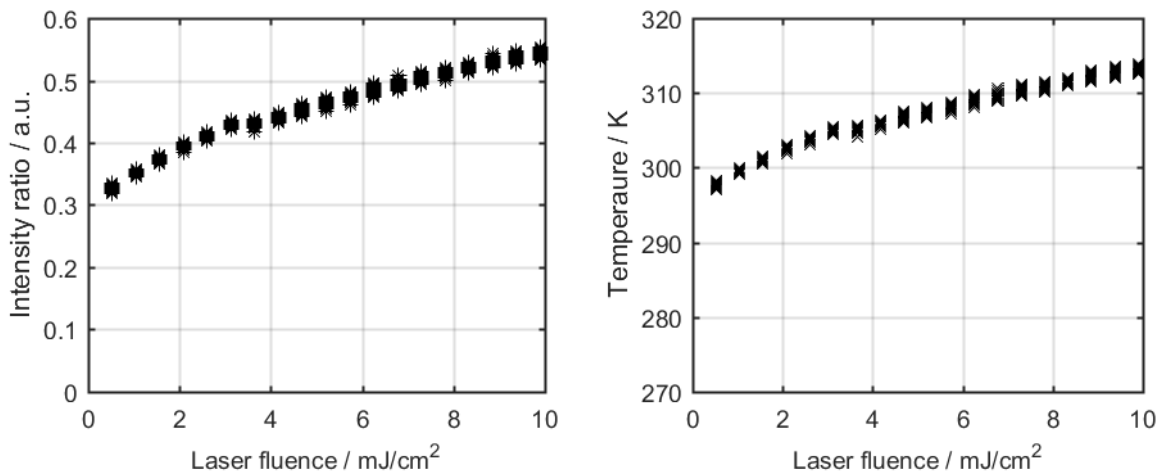


Figure 4-7: Intensity ratio as a function of laser fluence for ZnO (left). The intensity ratio is obtained by applying the convolution of the emission spectra with the filters indicated in Table 4-1 (left). The measured temperature as a function of laser fluence (right). A set of 50 samples are presented here for each laser fluence.

The laser-fluence dependence of the intensity ratio is shown in Figure 4-7. The intensity ratio was evaluated by convoluting the spectra with the interference filters presented in Table 4-1. The calculated ratio increases with the laser fluence as shown in Figure 4-7. Using the same approach used for BAM:Eu<sup>2+</sup>, the ratio sensitivity to temperature has been considered (presented later in Section 4.6). The modification on the emission spectrum due to the fluence variation causes a deviation of about 20 K in the temperature calculation. The effect of the fluence on the emission spectrum is presented in Figure 4-8. Increasing the laser fluence the emission spectrum appears to be red-shifted and it features differences in the shape.

As discussed for BAM:Eu<sup>2+</sup>, the variation of the emission spectrum could be attributed to the contribution of two factors: an increased surface temperature induced by the laser and saturation of the luminescence emissions at certain wavelength.

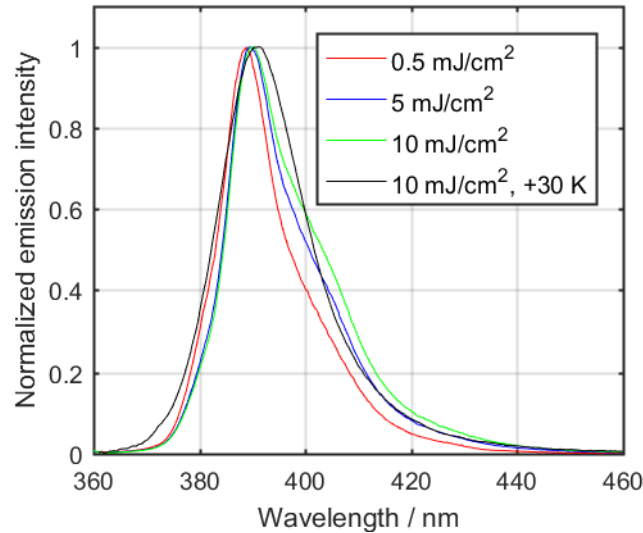


Figure 4-8: Comparison between the effect of the laser fluence and the effect of temperature on the emission spectrum of ZnO.

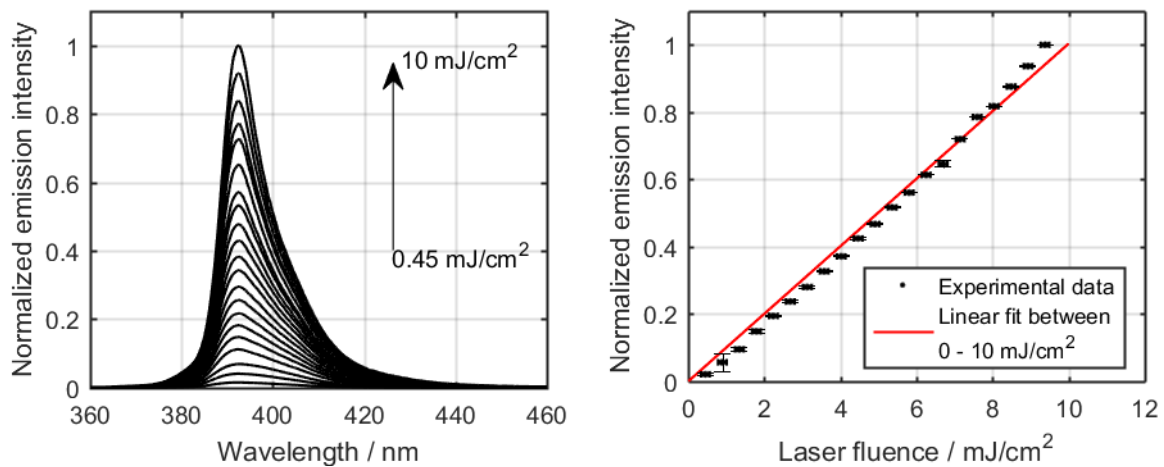


Figure 4-9: Fluence-dependence of the emission spectra (left) and the band-integrated emission intensity (right) of ZnO:Zn at 294 K relative to the values at the maximum laser fluence (10 mJ/cm<sup>2</sup>). Error bars show the standard deviation obtained over 50 samples.

A different behavior was observed for the ZnO:Zn phosphor. The emission intensity linearly increases with the laser fluence in the entire measured range up to 10 mJ/cm<sup>2</sup> as shown in Figure 4-9. The obtained intensity ratio oscillates around a constant value when increasing the laser fluence, as shown in Figure 4-10. The interference filters used for ratio calculation are presented in Table 4-1. The corresponding conversion to temperature leads to a temperature deviation of approximately 8 K. The comparison between the effect of the fluence and the effect of the temperature variation on the emission spectrum are shown in Figure 4-11. The shape of the spectrum slightly changes with increasing fluence leading to a

change in the intensity ratio and so on the temperature calculation. Even if the calculated intensity ratio oscillates around a constant value (Figure 4-10), the shape of the emission spectrum appears to be modified in a way that it cannot be explained by a simple variation of the coated-surface temperature. The emission spectrum obtained at +35 K appears to be different in shape compared to the spectrum at higher fluence suggesting a probable modification of the luminescence properties induced by the laser fluence.

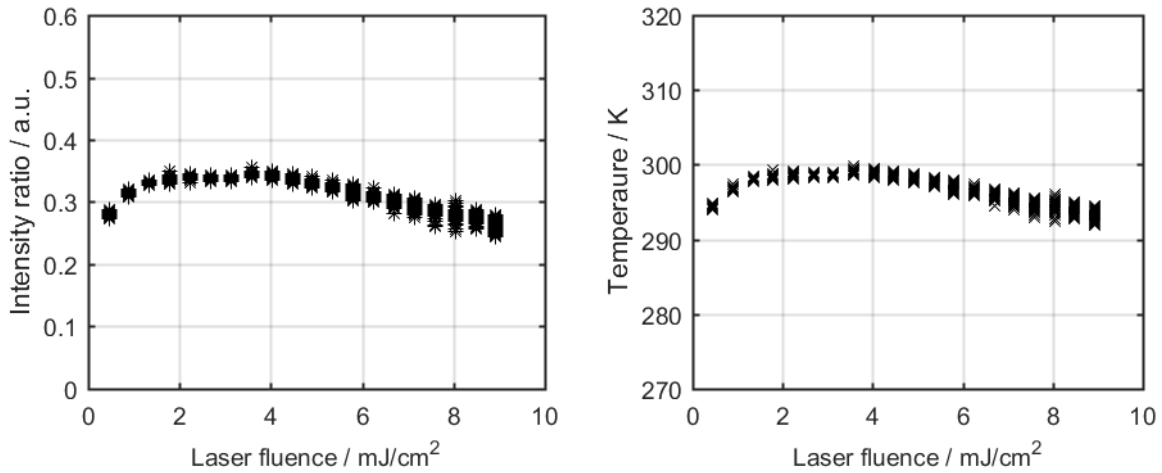


Figure 4-10: Intensity ratio as a function of laser fluence for ZnO:Zn (left). The intensity ratio is obtained by applying the convolution of the emission spectra with the filters indicated in Table 4-1 (left). The measured temperature as a function of laser fluence (right). A set of 50 samples are presented for each laser fluence.

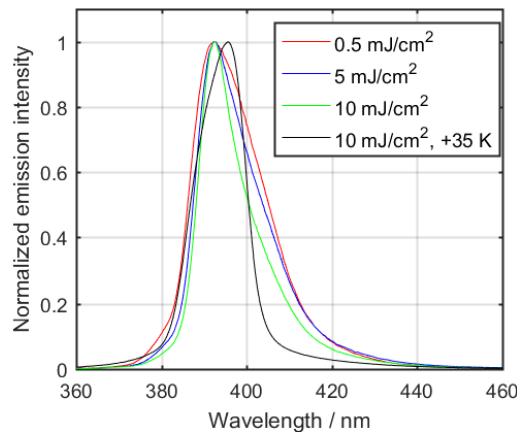


Figure 4-11: Comparison between the effect of the laser fluence and the effect of a temperature variation on the emission spectrum for ZnO:Zn.

This analysis shows that the dependence of the intensity ratio on the laser fluence is not the same for the three phosphors tested in this work. For the BAM:Eu<sup>2+</sup> and ZnO, the intensity ratio increases with the laser fluence, and if it is not taken into account, it leads to an error in the temperature measurements. The fact that the intensity ratio depends both on temperature and laser fluence has two main consequences when using these phosphors for thermometry purpose.

First, laser energy fluctuations need to be considered and corrected during the temperature measurements. Even the spatial fluctuations of the laser beam profile should be taken into account and corrected for. One way to avoid this problem can be the adoption of a top-hat laser beam profile or using a beam

homogenizer. The other point is that the shot-to-shot and spatial variations in fluence must be controlled during the calibration process. Multiple calibration curves at different fluence level are therefore needed to take into account this effect. This fact is probably associated to the observation that the various spectral bands show different fluence dependence. Therefore, in order to minimize the error in the temperature calculation due to the effect of fluence it is suggested to perform the intensity-ratio calibration in the similar fluence range that it will be used for the measurements. The intensity-ratio calibration method will be presented in Section 4.6.

### 4.2.3 Temperature dependence

In this section, the effect of the temperature on the emission spectra is presented. These results are important to see whether the phosphor materials is suitable for thermometry. The temperature sensitivity depends on how much the emission spectra change with temperature. To achieve higher measurement accuracy, 50 emission spectra were collected and averaged for each temperature investigated.

The normalized emission spectra of BAM:Eu<sup>2+</sup> are shown in Figure 4-12 as a function of temperature. The luminescence of BAM:Eu<sup>2+</sup> shows a blue-shift when the temperature increases. At room temperature, the emission peak is located at ~450 nm; when the temperature increases the spectrum broadens and shifts towards the UV region. The luminescence emission of this phosphor shows a quite large sensitivity to temperature throughout the 300–950 K temperature range.

As expected, the emission intensity decreases with increasing temperature due to thermal quenching. Figure 4-12 (right) shows the temperature dependence of the emission intensity. The intensity decreases by 20% from 300 to 700 K. Even if this phosphor is still sensitive up to 900 K, the emission intensity reduces by 80%.

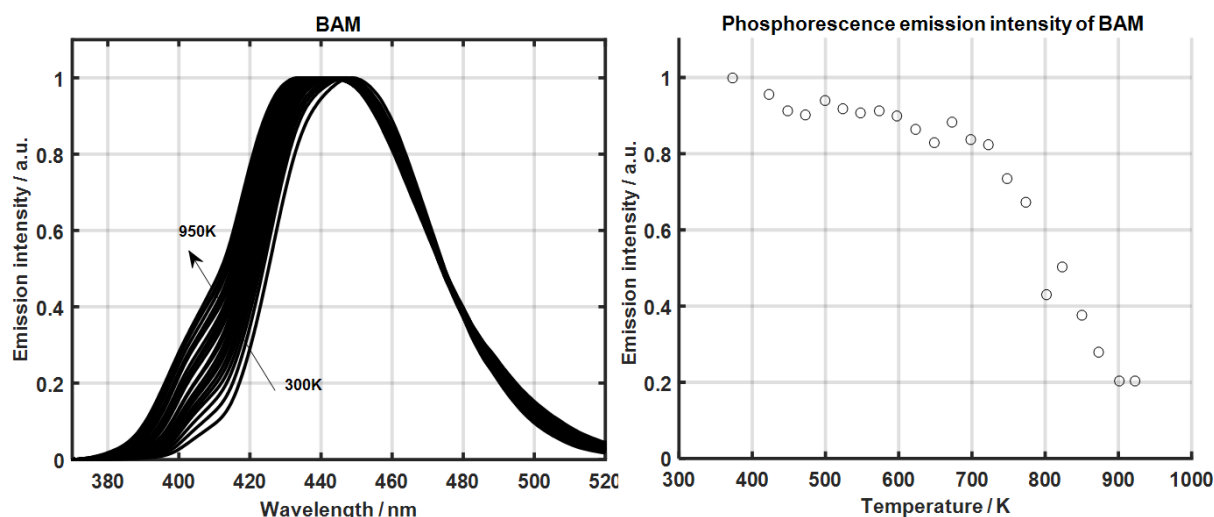


Figure 4-12: Temperature dependence of BAM:Eu<sup>2+</sup> emission spectra. Left: Spectra obtained at different temperatures normalized at each spectrum maximum value. The temperature interval between curves is ~25 K. Right: Temperature dependence of the band integrated (380–520 nm) emission intensity relative to the value at 300 K. Measurements are performed at 10 mJ/cm<sup>2</sup> laser fluence.

The results obtained with ZnO are shown in Figure 4-13. At room temperature, the emission spectra show a peak at  $\sim 390$  nm and a pronounced red-shift is observed when the temperature increases. The global luminescence intensity drops by more than 90% over the 300–900 K temperature range.

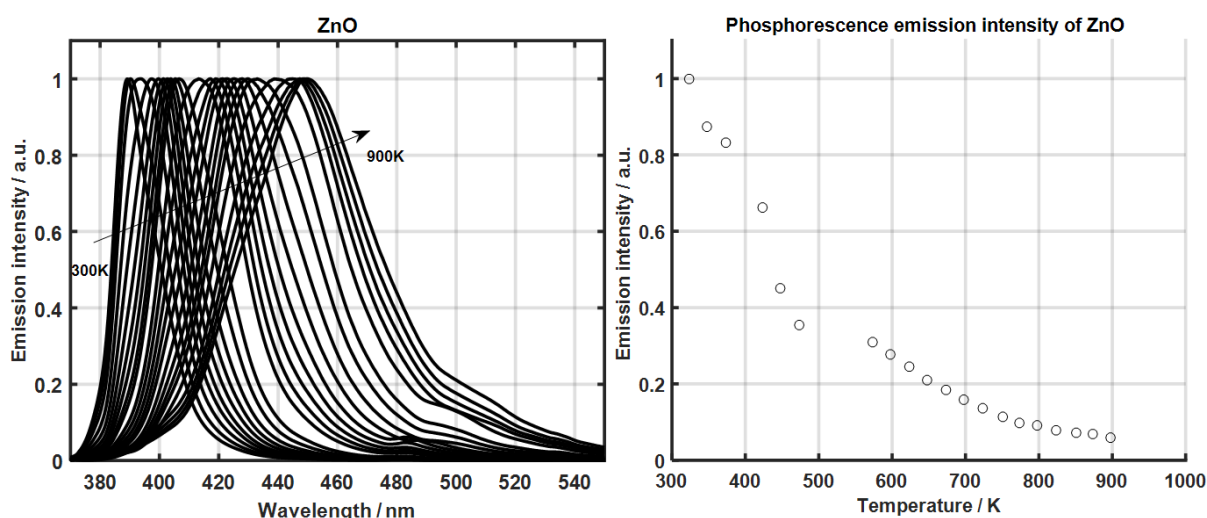


Figure 4-13: Temperature dependence of the ZnO emissions. Left: Spectra obtained at different temperatures normalized at each spectrum maximum value. The temperature interval between curves is  $\sim 25$  K. Right: Temperature dependence of the band-integrated emission intensity normalized to the value at 300 K. Measurements are performed at  $10 \text{ mJ/cm}^2$  laser fluence.

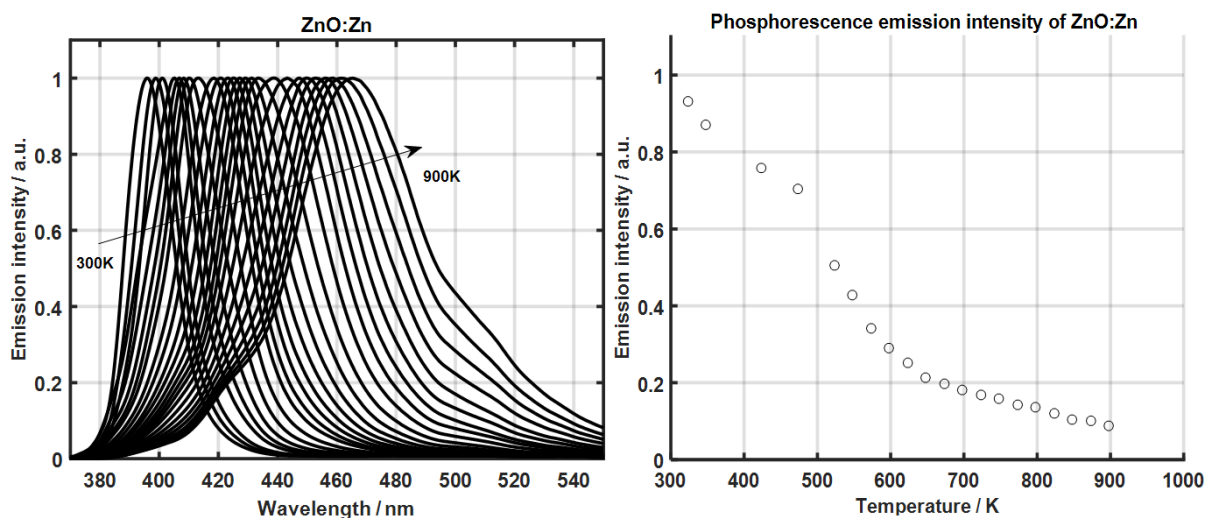


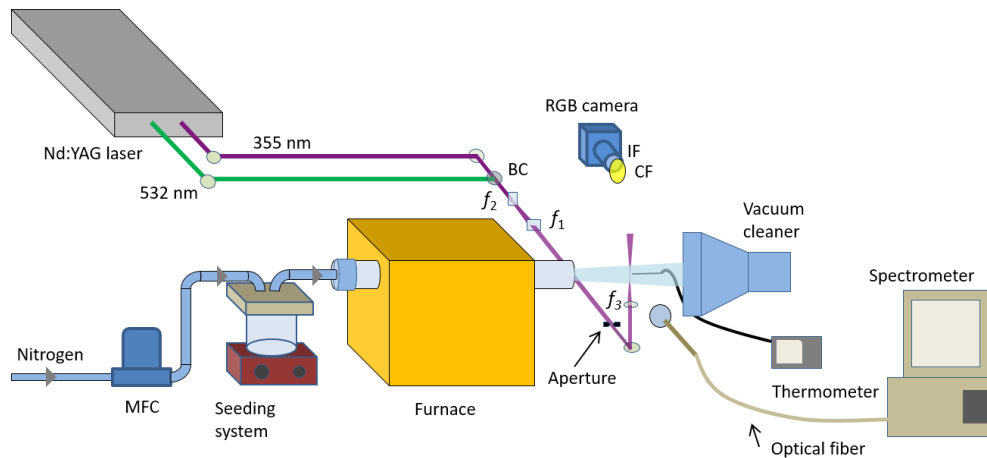
Figure 4-14: Temperature dependence of the normalized ZnO:Zn emissions. Left: spectra obtained at different temperatures normalized at each spectrum maximum value. The temperature interval between curves is  $\sim 25$  K. Right: temperature dependence of the band-integrated emission intensity relative to the value at 300 K. Measurements are performed at  $10 \text{ mJ/cm}^2$  laser fluence.

The ZnO:Zn phosphor shows the same behavior as ZnO. Figure 4-14 shows the temperature dependence of the emission spectra. The emission peak is located around  $\sim 393$  nm at room temperature. The ZnO:Zn spectrum is shifted by  $\sim 3$  nm towards the visible compared to the ZnO spectrum. The resulting shift is more pronounced at higher temperature, resulting in a slightly increased temperature sensitivity. On the other hand, a similar decrease in the total emission intensity was observed.

## 4.3 Characterization of aerosolized phosphors

### 4.3.1 Experiment

For characterization of the aerosolized phosphors, a high-temperature furnace was used to heat a gas flow seeded with phosphor particles. The investigated phosphors were seeded in a nitrogen flow using a custom-built seeding system containing a magnetic stirrer to agitate the particles. The seeding density was adjusted by changing the mass flow rate of the gas at the inlet of the seeder. The seeded gas flowed through a 17-mm diameter quartz tube positioned in the furnace. A K-type thermocouple was placed at the outlet of the quartz tube to measure the temperature of the heated gas. With this system, it was possible to reach particle temperatures up to 900 K. The schematics of the experiment is shown in Figure 4-15. Since the luminescence signal intensity of the phosphors is proportional to the particle number density [49], in these experiments the particle number density was directly measured using a dedicated particles counting system, described below.



Thermocouple	
Type K	1.5 mm
Spectrometer	
Horiba iHR320	$f = 300$ mm
Grating groove density	300 g/mm
Slit width	1 mm
Camera setup	
RGB Nikon D5100	2464×1632 pixels
Objective	Nikon 105 mm f/2.8
Pixel size	16×16 $\mu$ m

Optical setup	
Image area	65×45 mm <sup>2</sup>
Cylindrical lens	$f_1 = -150$ mm, $f_2 = 200$ mm
Spherical lens	$f_3 = 60$ mm
Laser sheet width	20 mm
Laser sheet thickness	0,8 mm

Filters and mirrors	
Filters	IF: 532 $\pm$ 5 nm CF: GG395

Figure 4-15: Experimental setup used for spectroscopic measurements of aerosolized phosphor particles.

### 4.3.2 Excitation system

The phosphor particles were excited at 355 nm using the third harmonic of a 10 Hz, Nd:YAG laser, with a pulse duration of 10 ns. The laser beam was expanded and focused using  $f = -150$  mm and  $f = 200$  mm cylindrical lenses to form an 800  $\mu$ m wide light sheet in the probe volume. A 0.8 mm slit aperture

---

confines the laser sheet into a rectangular shape that is relay-imaged into the center of the quartz tube with a spherical lens at a  $2f$  distance creating a nearly top-hat intensity profile. This spatial profile was measured with a beam profiler. The second harmonic (532 nm) of the same Nd:YAG laser was used to generate Mie scattering images for the particle counting system. The two laser beams were overlapped in the measurement plane using a dichroic beam combiner. The position of the laser sheet was adjusted to have the measurement plane in the horizontal axes of the quartz tube outlet, see Figure 4-16. A laser energy sensor was used to measure the energy of each laser pulse.

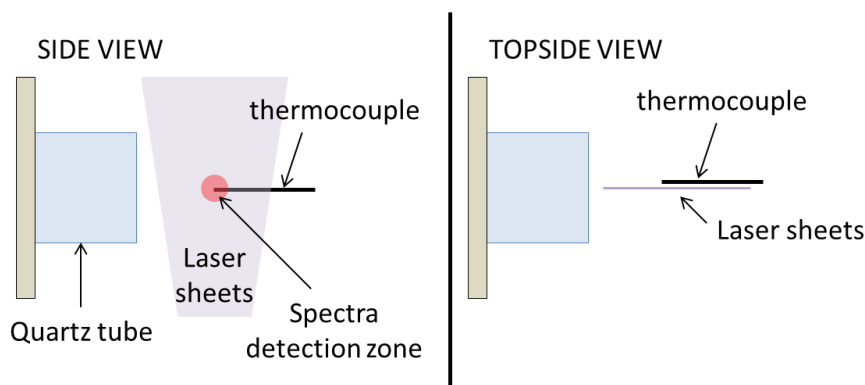


Figure 4-16: Schematics of the measurement plane for spectroscopic measurements of the aerosolized phosphor particles. The 0.8-mm-wide laser sheet intercepts the horizontal axis of the quartz tube outlet. The emission from the cross-section of the laser sheet with the horizontal axes of the quartz tube was imaged on an optical fiber and dispersed in a spectrometer. A type-K thermocouple placed in the center of the detection zone behind the laser sheet was used to measure the gas temperature.

#### 4.3.3 Detection system

Emission spectra were measured via an optical fiber connected to a spectrometer (Horiba iHR320) featuring a lens with focal length  $f = 320$  mm and aperture  $f\# = 4$  and the grating has 300 g/mm. The spectra are recorded with an interline-transfer CCD camera (exposure time: 1  $\mu$ s). The signal originating from the center of the laser sheet was focused with an  $f = 20$  mm spherical lens onto the face of an optical fiber. The light from the fiber was focused on the 1-mm entrance slit of the spectrometer. The resulting probe volume was 10 mm in diameter, see Figure 4-16. A pulse generator was used to synchronize the laser pulse with the spectrometer and the RGB camera used for particle detection.

The temperature of the heated flow was measured with a K-type thermocouple placed in the center of the detection zone slightly behind the laser sheet, Figure 4-16. The position of the thermocouple was chosen in order to avoid the luminescence of the particles that could stick on the thermocouple. The risk is to detect the higher luminescence coming from the excitation of the particles on the thermocouple. In this way, only the particles dispersed in the flow were excited by the laser sheet. The complete detection system was previously calibrated with the reference spectrum obtained using an integrated sphere within a tungsten halogen lamp.

#### 4.3.4 Particle preparation

---

The way how the particles are handled before their use is crucial for their application. The particle dispersion process depends on the particle properties, like size and shape, but also on the particle handling (e.g., moisture) and the type of seeder.

In order to have a more spatially homogeneous and constant seeding density, several operations are needed before using phosphor particles. The humidity contained in the phosphor powder tends to increase particle agglomeration reducing the flow ability. For this reason, the particles were mixed with aerosil nanoparticles. This flow aid, based on SiO<sub>2</sub> nanoparticles, helps the flowability and reduces the risk of agglomeration by increasing the surface roughness, thus increasing the particle separation. The mixed particles were then dried into an oven up to ~4 hours at ~150°C. This time was found to be sufficient to eliminate moisture containing in the powder to the required extent, thereby improving the particle seeding.

#### 4.3.5 Particle seeding

Particle seeding is a difficult task and it is largely based on empirical methods. The most frequently employed seeders are based on a fluidized bed where the powder is placed on a porous plate through which the gas flows. The particles are entrained from air flow through a porous plate constituted by micro-channels. The major drawback of this system is that the particles can agglomerate and clog the micro-channels. This phenomenon can result in an intermitting obstruction and liberation of the channels resulting in a non-homogeneous seeding with large particle agglomerates. This system can be improved with a rotating brush that permanently moves the particles on the porous plate.

Others types of seeders are based on the aerodynamic movement generated by the gas flow in the seeder itself. A reverse-cyclone seeder generates strong swirl in the vessel containing the particles. The quality of the seeding is improved by the centrifugal force acting to separate agglomerates helping a more spatially homogenous distribution.

The seeder used in this work is based on the mechanical agitation of the particles (Figure 4-17). The gas flows is directed downwards into a vessel filled with particles that are permanently agitated by a magnetic stirrer. The resulting aerosol moves to the outlet, which is placed in the top of the vessel. The aerosol flow-rate is adjusted by a mass-flow controller placed at the inlet seeder. A comparison between the two systems (the aerodynamic type and the fluidized bed) was done by seeding a sample air flow and the images obtained indicated that the second system provides a more homogeneous seeding and more constant in time. This system was therefore chosen to have a consistent and spatially homogeneous seeding.

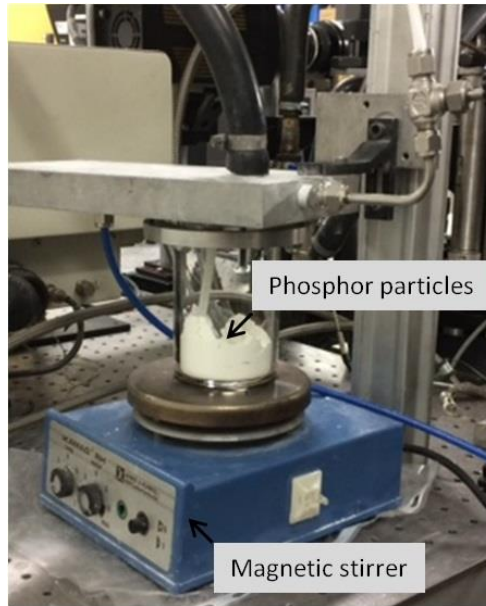


Figure 4-17: Particle seeder used in this work. The particles are mechanically agitated by a magnetic stirrer. This seeder generates a consistent and spatially homogeneous seeding.

#### 4.3.6 Particle counting system

A dedicated particle counting system was developed for this study. The aim of this system was to measure the number density of the phosphor particles in the probe volume, regardless of their size and shape. To determine the number of particles in the measurement volume, the Mie-scattering signal from the particles was imaged with a digital camera (Nikon D5100) at  $90^\circ$  from the excitation laser sheet via a  $f = 105 \text{ mm}$   $f_\# = 2.8$  lens and a  $532 \pm 5 \text{ nm}$  interference filter. The particles were illuminated using a frequency-doubled Nd:YAG laser operating at 10 Hz.

The phosphorescence emitted by the particles and reflected by the interference filter was found to interfere with the detection system. To prevent such interferences, a color-glass filter (OG515, Schott), at  $45^\circ$ , was positioned in front of the camera in order to prevent any interfering reflections with the spectroscopy system [49]. The collection apparatus provided a field of view of  $40 \times 30 \text{ mm}^2$  with a  $16\text{-}\mu\text{m}$  pixel size. This resolution was sufficient to resolve particle number densities at the order of  $10^{10}\text{--}10^{11}$  particles/ $\text{m}^3$ . Based on the fact that a particle including its flare was about 4 pixels in the raw image and considering that the particle images must be separated by at least two pixels from each other to be distinguished in the probe volume, the maximum number of particles that can be distinguished in the region of interest is in the order of  $1.3 \times 10^5$  particles and therefore the maximum measurable number density is about  $1.4 \times 10^{11}$  particles/ $\text{m}^3$ .

The laser energy was adjusted to avoid sensor saturation and provide the better signal-to-noise ratio on the image. Considering the aim of this calculation, which was mainly qualitative, all the detected particles were considered directly illuminated neglecting the effect of multiple scattering. The Mie-scattering images were post-processed via a Matlab algorithm presented in Figure 4-18. The procedure is described below:

- A cut-off filter of 15% of the maximum intensity peak is applied to the RAW images to remove low pixel intensities
- A region of interest (ROI) with a diameter of 10 mm corresponding to the dimension of spectrometer detection volume is defined in the images
- The images are binarized before applying a contour function to detect contour lines with the same intensity level (0.8 over a full range of 1)
- The number of elements surrounded by a contour plot is used as a measure of the number of particles in the measurement zone

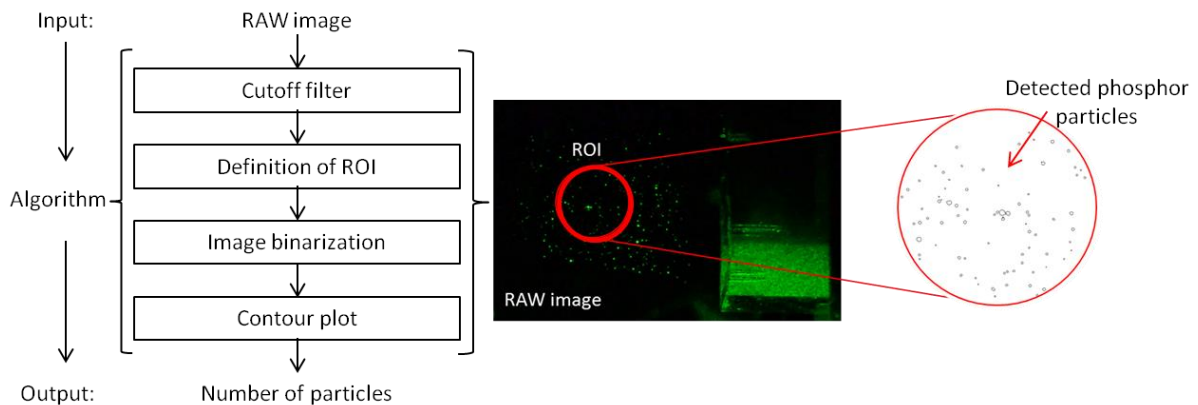


Figure 4-18: Basic principles of the algorithm developed for particle counting. The Mie-scattering images are post-processed to determine the number of particles in the probe volume.

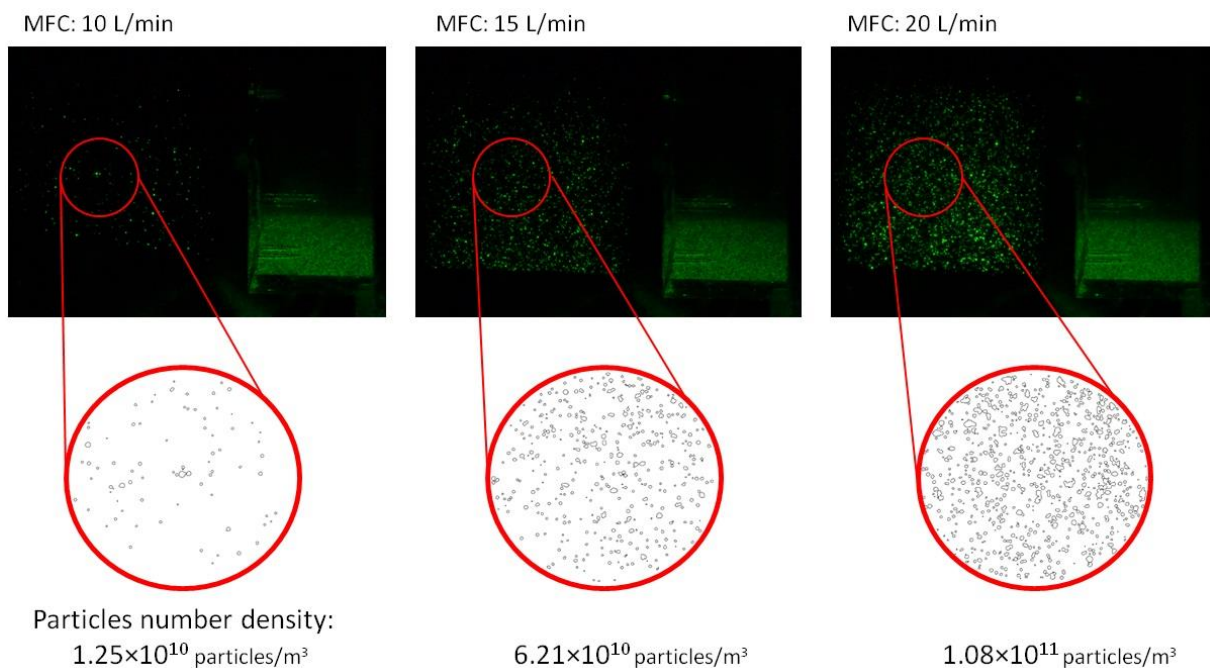


Figure 4-19: Different seeding densities obtained at different flowrates through the seeder.

The algorithm was validated by testing various seeding conditions, as shown in Figure 4-19. The seeding density was adjusted by changing the mass flow rate at the inlet of the seeder. A series of images were collected and then processed for each seeding condition in order to determine the seeding densities. The

---

counting algorithm calculated a range of seeding densities from  $10^{10}$  to  $10^{11}$  particles/m<sup>3</sup>. As it can be observed for the highest seeding density case, the size of the particles seems to be bigger. This fact is related to the spatial resolution of the system approaching its limit and merging together different particles. For the purpose of this thesis, this limit does not represent a problem since lower seeding densities will be used. In fact for thermographic PIV, a seeding density of  $10^{11}$  particles/m<sup>3</sup> is recommended to have good level of spatial resolution without altering the thermal properties of the probed gas [49].

## 4.4 Results obtained for aerosolized phosphor particles

### 4.4.1 Seeding density effect

To investigate the influence of the seeding density on the measured intensity ratio, the emission spectra were collected while simultaneously measuring the seeding density. This was possible thanks to the particle counting algorithm developed in this work. For fixed laser fluences, the seeding density was varied and the number of particles in the probe volume was measured. For this test a laser fluence of 20 mJ/cm<sup>2</sup> was chosen. This reference value was first chosen because it had already been used in the literature [49], and then the analysis of the effect of fluence presented later in this chapter showed that the effect of fluence is not expected to be significant.

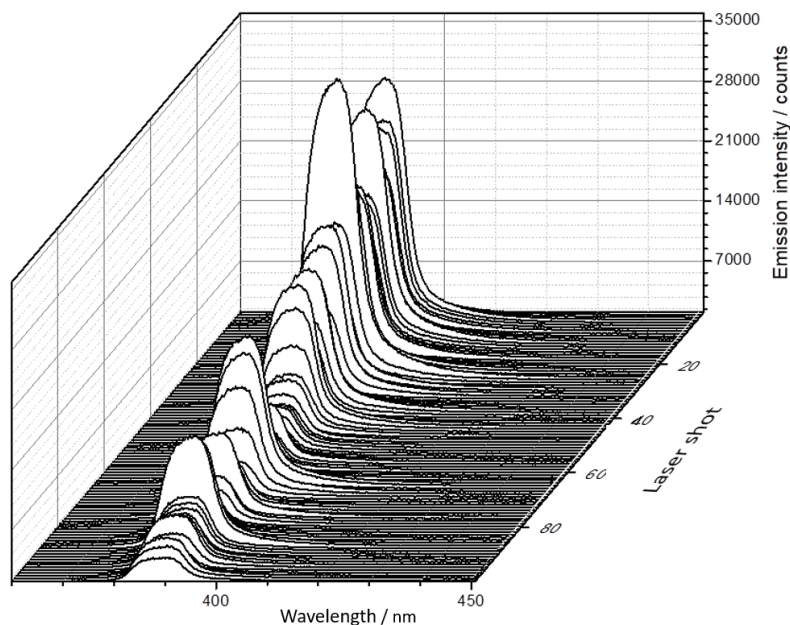


Figure 4-20: Time series of luminescence emission spectra of dispersed ZnO:Zn particles in aerosol for a fixed excitation fluence of 20 mJ/cm<sup>2</sup>. The measurements were made at constant ambient temperature of 25°C. The variation of the emission intensity is mainly due to the seeding density fluctuations during the measurements.

Figure 4-20 shows a sequence of 100 single-shot ZnO:Zn emission spectra measured at 25°C and at constant laser fluence of 20 mJ/cm<sup>2</sup>. The variations of the emission intensity are mainly due to the seeding density fluctuations during the measurements. With the knowledge of the absolute particle number density, the effect on the intensity ratio was studied. The evolution of the emission intensity during the measurements is presented in Figure 4-21 (left). The normalized emission spectra, presented in Figure

4-21 (right), shows that the seeding density has a negligible effect on the intensity ratio calculation, i.e., the evaluated particle temperature. This aspect is confirmed in Figure 4-22, where the dependence of the intensity ratio on the seeding density is presented. These results indicate that no effect on the measured temperature is expected for seeding densities up to  $1 \times 10^{11}$  particles/m<sup>3</sup>.

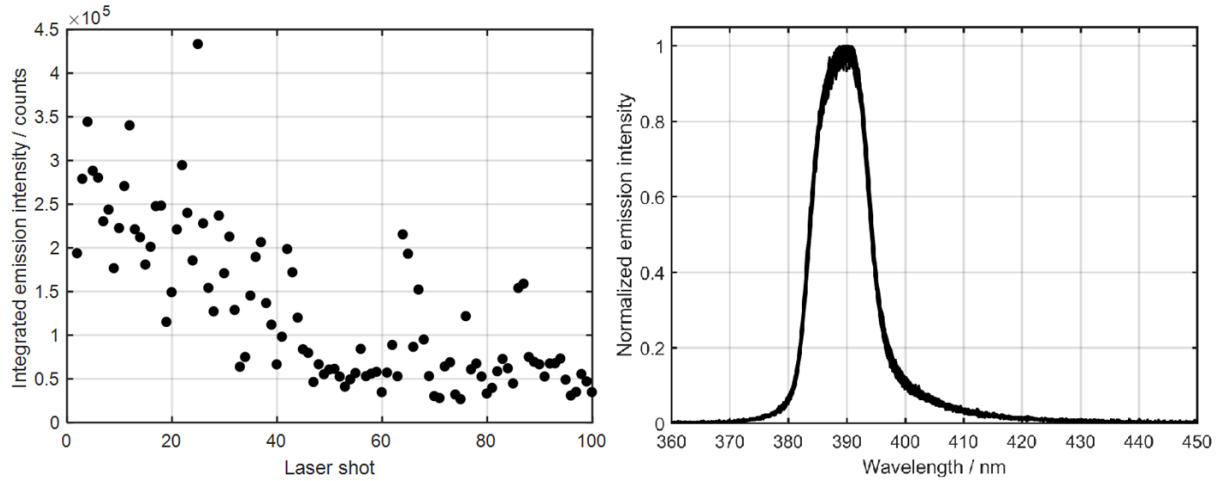


Figure 4-21: Effect of the seeding density on the luminescence intensity for ZnO:Zn particles. Left: Variation of the integrated emission intensity during 100 single-shot measurements at ambient temperature and at fixed laser fluence. The emission intensity is calculated by integrating the absolute emission spectrum over the 380–400 nm wavelength range. Right: The normalized emission spectra for the entire series of 100 laser shots.

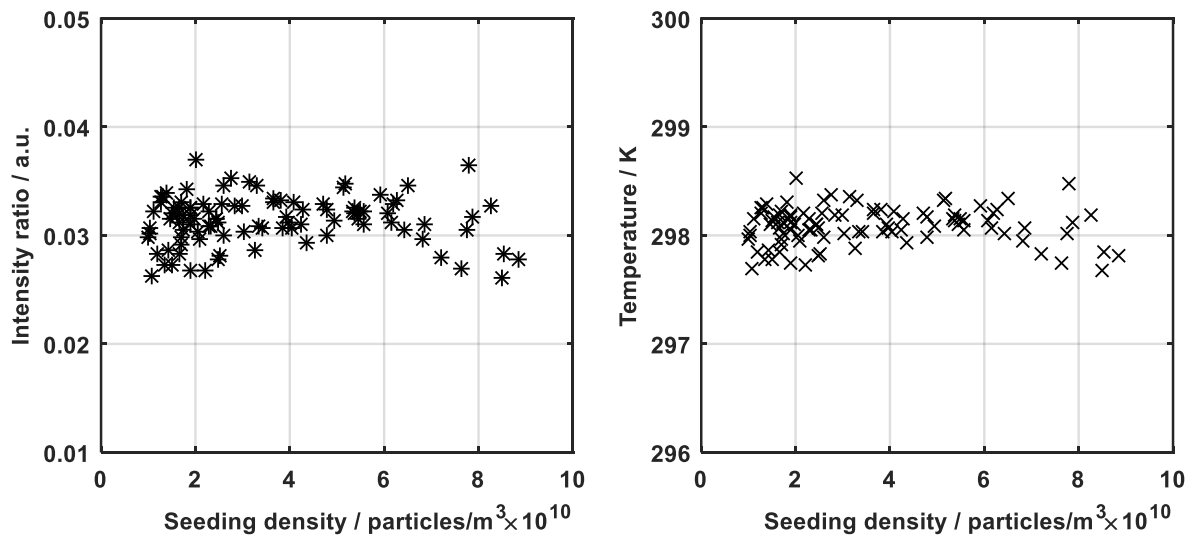


Figure 4-22: Left: Intensity ratio as a function of the seeding density for ZnO:Zn. Right: Measured temperature as a function of seeding density. The calibration curve for temperature determination is shown in Figure 4-40.

The correlation between emission intensity and seeding density was also investigated. As shown in Figure 4-23, it was found that the integrated emission intensity is a linear function of the seeding density. This aspect can be used to increase the signal level and thus the signal-to-noise ratio in a way to improve the measurements precision. Higher seeding densities, however, can alter the thermal properties of the probed gas inducing a source of error in the measurements. For PIV, a seeding density of  $10^{11}$  particles/m<sup>3</sup> is recommended to not deteriorate the spatial resolution [48]. A compromise needs to be found

to have a comparable resolution between the thermometry technique and PIV avoiding to alter the gas thermal properties [49].

The particles number density can also be used to correct the intensity fluctuations of the single-shot measurements. The correction obtained by dividing the emission intensity by the instantaneous seeding density is presented in Figure 4-23 (right). As expected, the corrected intensity level, shown in Figure 4-23 oscillates around a constant value, confirming that the intensity fluctuations are mainly due to seeding density fluctuations. Without the correction from the seeding density the luminescence intensity shows a strong variation of a factor  $\sim 12$ , as presented in Figure 4-23(right). After the correction the luminescence intensity variation is improved of about 80%. The other 20% of the intensity dispersion can be attributed to other source of error, e.g., the spatial variation of the laser fluence.

This correction from the seeding density is useful for the phosphor characterization to isolate the different bias affecting the luminescence emission intensity. In this work, in order to improve the signal-to-noise of the spectroscopic measurements were performed with the accumulation method, explained in the next section. Therefore, it was not possible to correct the emission spectrum for the instantaneous level of the seeding density. Another method was used to take into account the different level of seeding density: the peak intensity at 355 nm corresponding to the Mie scattering signal of the particles, was used as an indication of the seeding density. This approach was used to correct the absolute measured spectrum from the seeding density fluctuation.

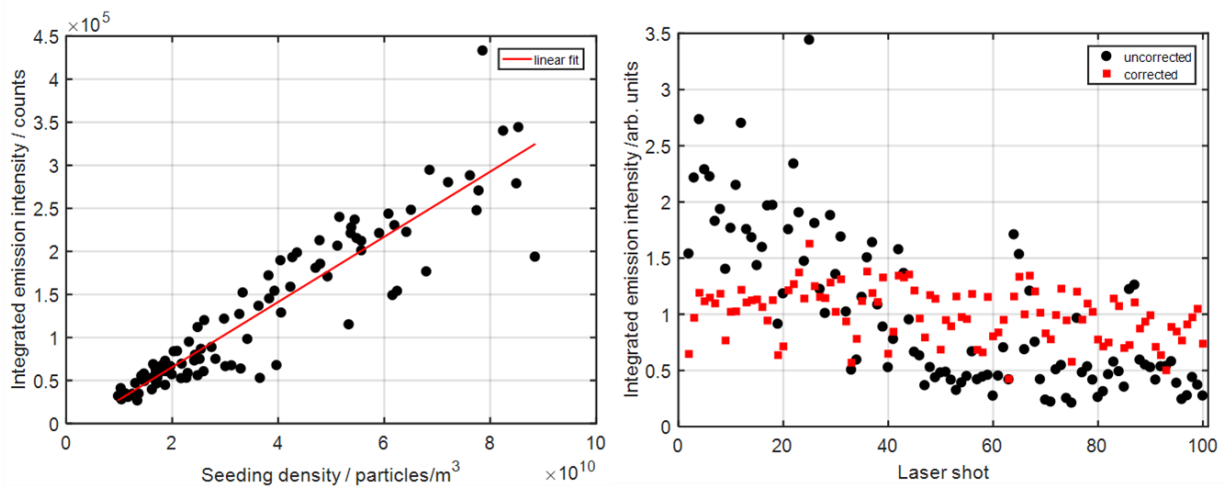


Figure 4-23: Dependence of the integrated emission intensity on the ZnO:Zn particle seeding density. Laser fluence: 20 mJ/cm<sup>2</sup> at 25°C. Left: Emission intensity as a function of seeding density. Right: Shot-to-shot variation of the integrated emission intensity before and after correction for the instantaneous seeding density.

---

#### 4.4.2 Laser fluence effect

The dependence of the emission spectra on the laser fluence was measured to analyze the impact on the intensity ratio. To increase the signal-to-noise ratio of the measurements successive spectra were accumulated on the CCD camera. In general, the shot noise is reduced by the square root of the number of spectra that are accumulated together [87]. In this study, 100 successive spectra were accumulated leading to an improved shot noise of a factor of ten.

Figure 4-24 shows normalized ZnO:Zn spectra obtained with laser fluences from 20 to 90 mJ/cm<sup>2</sup> at 300 and 470 K. The results show that the emission spectra do not depend on the laser fluence at 300 K. This results in a negligible impact on the intensity ratio and thus the temperature estimation. At higher temperature, a slight deviation of the emission spectra was observed, as shown in Figure 4-24 (right). However, the effect of the fluence on the spectra at higher temperature is not fully demonstrated. At higher temperature, the signal-to-noise ratio decreases as a result of a decrease in the luminescence intensity caused by thermal quenching. This fact leads to a decreased measurement precision at higher temperatures.

The results obtained using respectively ZnO and BAM:Eu<sup>2+</sup> phosphors are presented in Figure 4-25 and Figure 4-26. The impact of the laser fluence on the emission spectra is not significant in the investigated fluence range. The results presented here are quite in contradiction with the spectrum dependence on the laser fluence found for coated-surface measurements and discussed in section 4.2. It is not clear what is the origin of the different impact of the laser fluence on aerosol and surface measurements, therefore few hypotheses are presented. The first is that the effect of the laser fluence inducing surface heating has a negligible effect on aerosol measurements compared to the measurements performed on coated-surface (shown in section 4.2) and there is no impact on the emission spectra.

The second hypothesis is that the differences can be referred to a different light interaction between aerosol and surface measurements. In coated-surface measurements the higher particles number density can produce multiple scattering phenomena inducing an error in the detected spectrum [3]. Due to the higher number density, the light can be scattered from the neighbor particles and reflected/absorbed from the surface. The aerosol measurements are less affected by this phenomenon due to the relatively lower particles number density compared to surface measurements.

The third hypothesis is that the differences can be attributed to a variation of the luminescence properties of the phosphor material induced by the industrial manufacture. In fact, different batches of phosphor could have different physical properties (e.g., doping concentration, quantity of impurities, particles size and shape) depending of the manufacturer tolerances. This probable batch-to-batch variation can induce to a dispersion on the luminescence properties of the phosphor material. As the aerosol measurements were performed with a different batch of phosphors, this hypothesis needs to be considered. At this stage, the three hypotheses mentioned above need to be considered equally possible and further investigations need to be done.

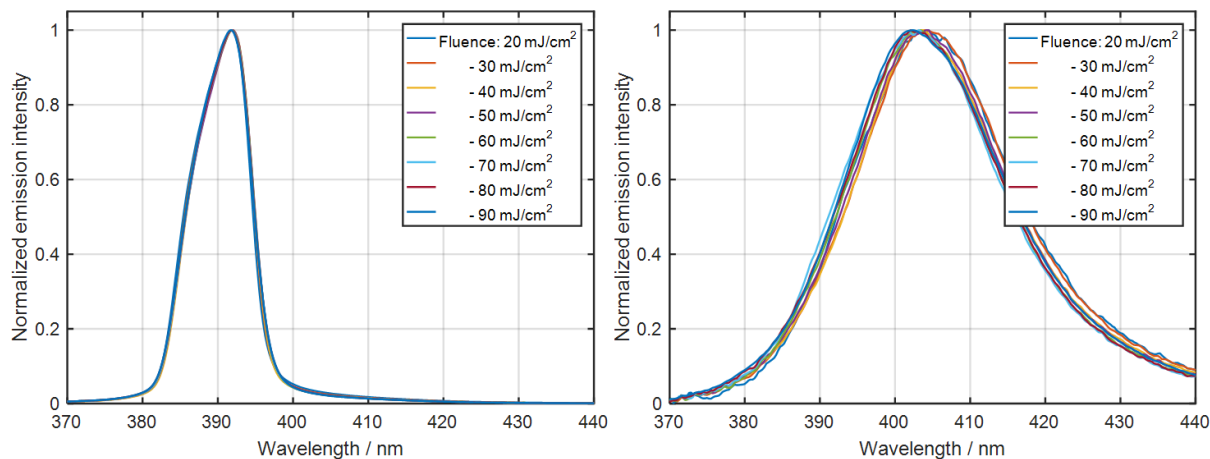


Figure 4-24: Normalized ZnO:Zn emission spectra for aerosolized particles at 300 K (left) and 470 K (right). Measurements with laser fluences ranging from 20 to 90 mJ/cm<sup>2</sup> are shown.

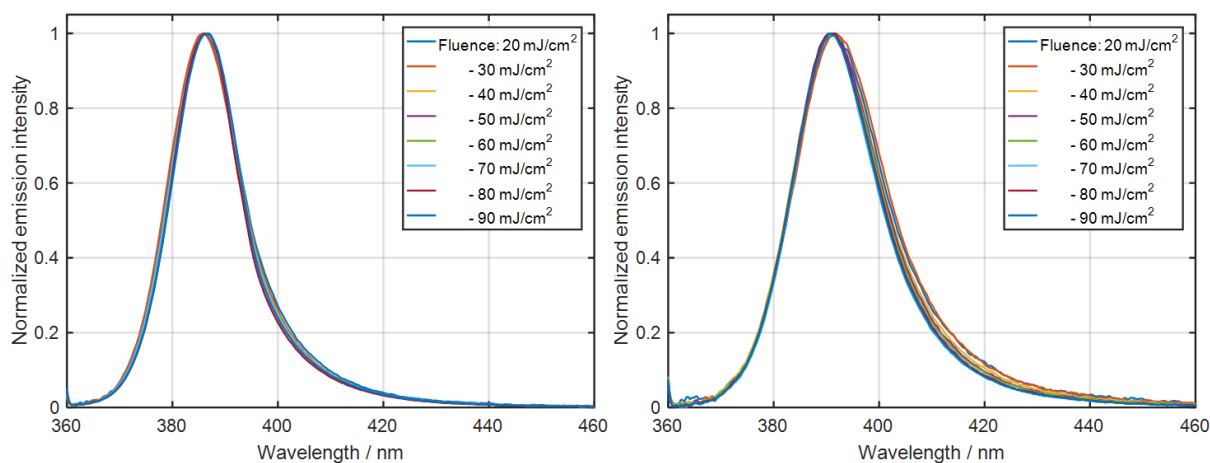


Figure 4-25: Normalized ZnO emission spectra for aerosolized particles at 300 K (left) and 450 K (right). Measurements with laser fluences ranging from 20 to 90 mJ/cm<sup>2</sup> are shown.

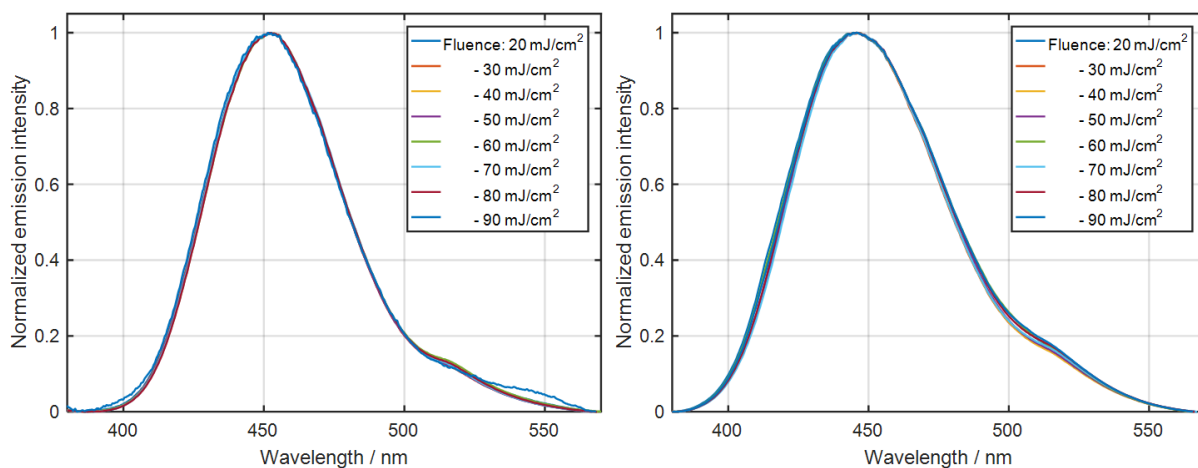


Figure 4-26: Normalized BAM:Eu<sup>2+</sup> emission spectra for aerosolized particles at 300 K (left) and 460 K (right). Measurements with laser fluences ranging from 20 to 90 mJ/cm<sup>2</sup> are shown.

#### 4.4.3 Temperature dependence

The impact of temperature on the phosphors's emission spectra are crucial for the determination of the calibration data that will be used in the engine measurements. The approach of this thesis is based on an *ex situ* temperature calibration. The calibration curve is obtained from the variation of the emission spectra as a function of temperature. The calibration curves are presented later in Section 4.6.

The emission spectra presented here are the result of the accumulation of 100 single-shot measurements. This was done to increase the signal-to-noise ratio, thus improving the detection of the emission spectra at elevated temperatures. The associated measurements uncertainty is presented in the Section 4.7. The temperature dependence of the emission spectra on the laser fluence was also evaluated over the 20–90 mJ/cm<sup>2</sup> range.

The temperature dependence of ZnO:Zn emission spectra is shown in Figure 4-27. As expected from the phosphor measurements on coated surfaces, the emission spectra shift with increasing temperature. The spectral shift observed in the aerosolized ZnO:Zn particles is much lower than that measured on the coated surfaces. A comparison between the emission spectra obtained in the aerosol and on surface is presented in the next paragraph. The emission peak, initially located at 392 nm at room temperature, shifts up to 425 nm at 780 K, as shown in Figure 4-27 (right). The dependence of the emission peak position on the laser fluence can be considered negligible. The normalized emission intensity drops with increasing temperature, as shown in Figure 4-28 (left). The emission intensities are normalized from the emission intensity obtained at 300 K with a laser fluence of 60 mJ/cm<sup>2</sup>. From 20 to 60 mJ/cm<sup>2</sup>, the normalized emission intensity increases, improving the signal-to-noise ratio of the spectra. A noticeable dependence of the emission intensity on the laser fluence is visible at constant temperature. Note that the emission intensity presented here was previously corrected for fluctuations in seeding density. As mentioned in section 4.4.1, the peak intensity at 355 nm corresponding to the Mie scattering signal of the particles was used as a qualitative estimation of the seeding density. However, this approach shows some limit, e.g., the super-linear increases of the emission intensity with fluence at ambient temperature, also visible in Figure 4-30 and Figure 4-32. Therefore, the results presented here could be affected by errors on the estimation of the seeding density. For this reason, a quantitative analysis of the seeding density during the measurements needs to be done in future.

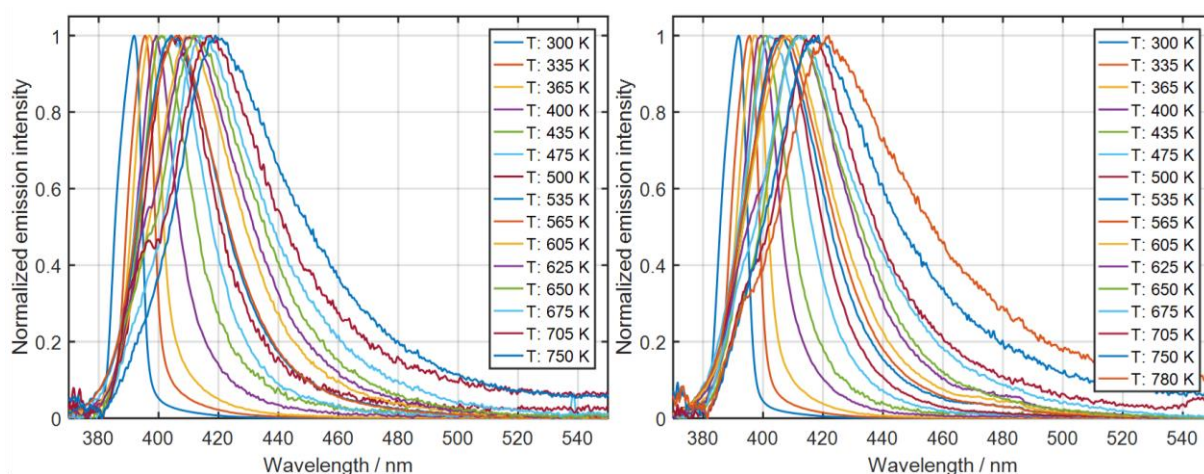


Figure 4-27: Normalized emission spectra of aerosolized ZnO:Zn particles measured at 20 mJ/cm<sup>2</sup> (left) and 80 mJ/cm<sup>2</sup> (right) from 300 K to 780 K temperature. As the temperature increases, the emission spectrum strongly shifts toward longer wavelengths.

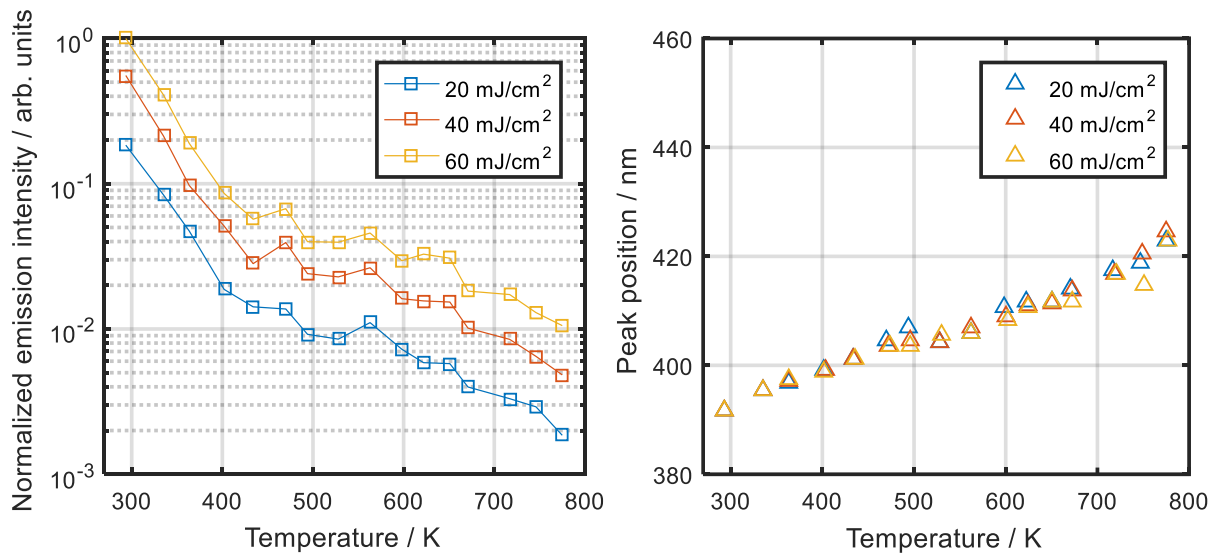


Figure 4-28: Left: Emission intensity as a function of temperature for aerosolized ZnO:Zn at 20, 40, and 60 mJ/cm<sup>2</sup>. Right: Temperature dependence of the wavelength position of the emission peak.

The same investigations for ZnO led to similar observations (Figure 4-29). The emission spectra of ZnO at room temperature appear to be shifted toward the UV region by about 4 nm compared to ZnO:Zn spectrum, as shown in Figure 4-30. ZnO shows a similar decrease in the total emission intensity as ZnO:Zn, as shown in Figure 4-30 (left). However, for the ZnO phosphor, due to the weak emission intensity, it was not possible to measure the emission spectrum at temperatures higher than 700 K. This result might be due to lower emission intensity at higher temperatures compared to ZnO:Zn. However, due to the qualitative approach on the estimation of the seeding density, it was not possible to compare the absolute emission intensity of both phosphors. Further analysis of the emission intensity per particles needs to be done in future.

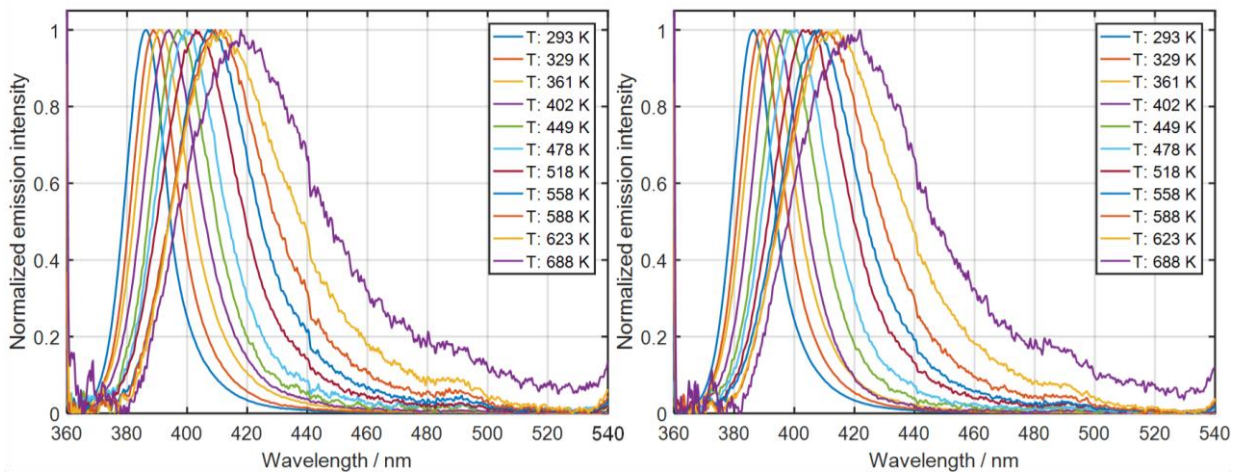


Figure 4-29: Normalized emission spectra obtained from aerosolized ZnO particles measured at 20 mJ/cm<sup>2</sup> (right) and 80 mJ/cm<sup>2</sup> (left) from 293 K to 688 K temperature. As the temperature increases, the emission spectrum strongly shifts toward longer wavelengths.

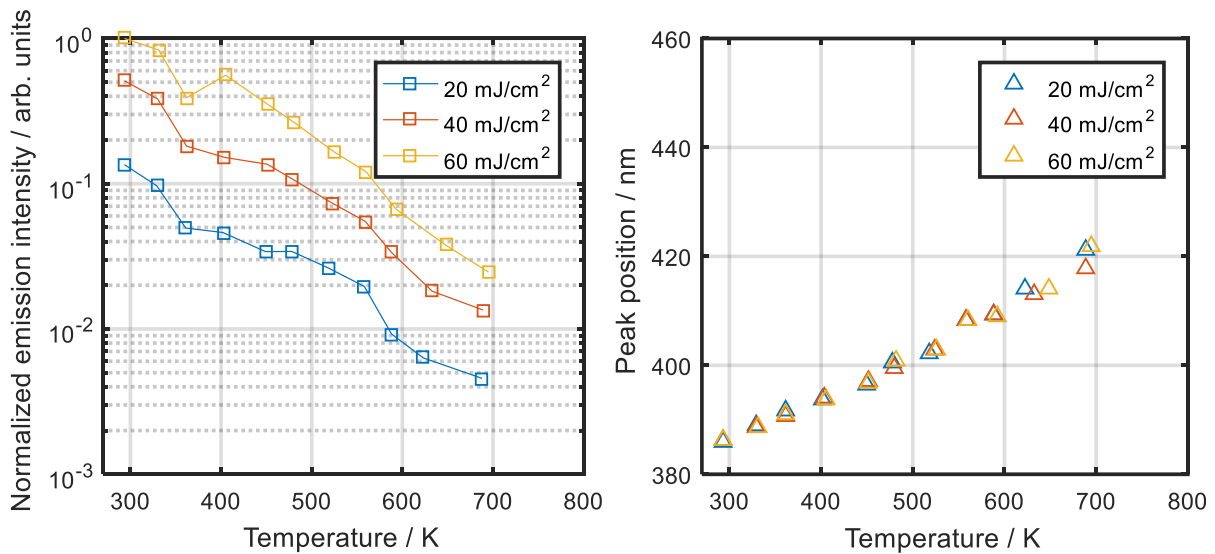


Figure 4-30: Right: Emission intensity as a function of temperature obtained for aerosolized ZnO at 20, 40, and 60 mJ/cm<sup>2</sup>. Right: Temperature dependence of the emission peak position.

For BAM:Eu<sup>2+</sup>, the normalized emission spectra are presented in Figure 4-31 for 306–720 K. As expected, the BAM:Eu<sup>2+</sup> spectra shift towards the UV with increasing temperature. The shift appears to be smaller corresponding to a smaller temperature sensitivity compared to the ZnO phosphors. At room temperature, the emission peak position is at 452 nm, at 700 K the emission peak is moved to 440 nm, as shown in Figure 4-32(right).

Figure 4-32(left) shows the temperature dependence of the emission intensity. The drop in the emission intensity with temperature is significantly lower compared to ZnO. Over the 300–700 K range, the intensity drop is on the order of 80%. The resulting emission intensity increases with the laser fluence as shown in Figure 4-32.

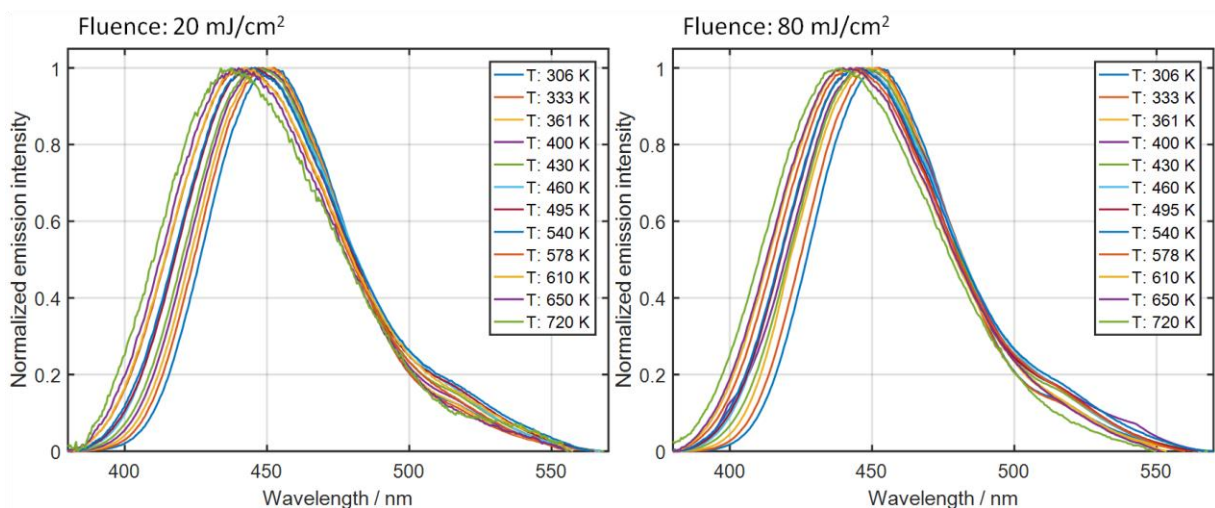


Figure 4-31: Normalized emission spectra for aerosolized BAM particles measured at 20 mJ/cm<sup>2</sup> (right) and 80 mJ/cm<sup>2</sup> (left) from 306 K to 720 K temperature. As the temperature increases, the emission spectrum broadens and shifts toward the UV.

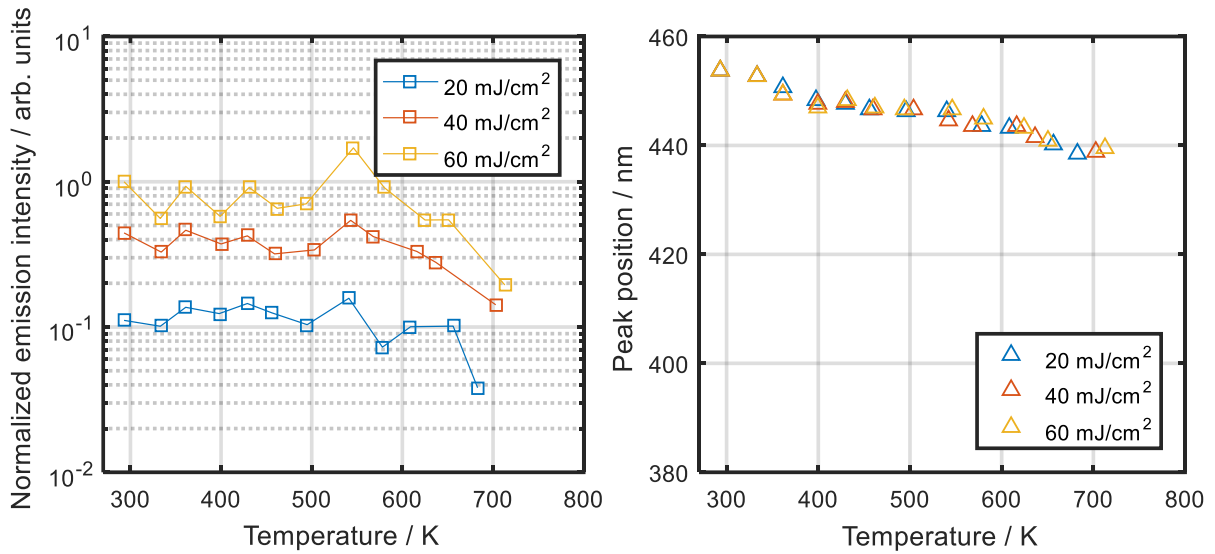


Figure 4-32: Normalized emission intensity as a function of temperature for aerosolized BAM:Eu<sup>2+</sup> (right). The experiments were conducted at 20, 40, and 60 mJ/cm<sup>2</sup>. Right: Temperature dependence of the emission peak position with temperature (right).

#### 4.5 Comparison of the performance of phosphors in surface and aerosol measurements

This section is dedicated to the comparison between the emission spectra measured in aerosol and on surface conditions. Moreover, the measured spectra are compared to other spectral data found in the literature. The results for surface characterization have been obtained using two different experimental arrangements. Setup 1 is described in Section 4.2., setup 2 corresponds to the aerosol characterization setup as described in Section 4.3 but where a coated surface has been placed in the measurement volume so that a surface characterization is carried out instead of the aerosol. In this configuration, the surface characterization is only carried out at ambient temperature

In the literature, results from different types of characterization methods are described. Särner et al. [71] used a coated surface for characterization similar to what is described in section 4.2. Abram et al. [70] characterize material disposed in a pile of powder.

Table 4-2: Excitation energy and laser fluence for different measurement conditions.

Measurement conditions	Type of phosphor	Laser fluence / mJ/cm <sup>2</sup>
Powder, Abram et al. [70]	ZnO:Zn, ZnO	2.5
Powder, Fond et al. [69]	BAM:Eu <sup>2+</sup>	1
Coated surface, Särner et al. [71]	ZnO:Zn	18
Aerosol	ZnO:Zn, ZnO, BAM:Eu <sup>2+</sup>	20–90
Coated surface (setup1)	ZnO:Zn, ZnO, BAM:Eu <sup>2+</sup>	0.5–10
Coated surface (setup2)	ZnO:Zn, ZnO, BAM:Eu <sup>2+</sup>	20

Figure 4-33 shows the comparison obtained for ZnO:Zn at 298 and 475 K. The spectra measured in the aerosol are shown in red solid lines. The dashed lines indicate the spectra obtained from surface measurements and the dot-dashed lines indicate the results from powder measurements.

At ambient temperature (Figure 4-33, left), the emission spectra obtained from surface and powder measurements show a broad emission band compared to the aerosol measurements, except for the surface measurements performed with setup 2 where the spectrum has the same narrow band but different peak position. This aspect suggests that using the same experimental setup for aerosol and surface measurements reduces the errors induced by different measurement setups. Also, the emission peak detected from each measurements shows a different wavelength position and this effect is more pronounced at higher temperature, shown in Figure 4-33 (right). At this stage, the reason why the emission spectrum changes from aerosol to surface or powder measurements is not clear and some hypotheses are proposed. The first is that the laser fluences used in the measurements have an impact on the shape of the spectrum as already discussed in Section 4.2; the measurements compared here for both systems have not been performed with the same laser fluence as shown in Table 4-2.

The second is that the multiple scattering phenomena occurring on surface and powder measurements can alter the shape of the emission spectrum, as explain in the section 4.4. Other reasons like batch-to-batch variation, temperature controlling system and spectrometer accuracy can also be responsible of the observed differences. In conclusion, further investigations are required to investigate the emission spectra of phosphors under different measurement conditions. For future measurements, an appropriate experimental setup allowing different measurement conditions (e.g., aerosol, coated-surface, powder) is suggested to minimize the measurement uncertainties.

Similar considerations can be done for the spectra comparison of ZnO and BAM:Eu<sup>2+</sup> presented in Figure 4-34 and Figure 4-35.

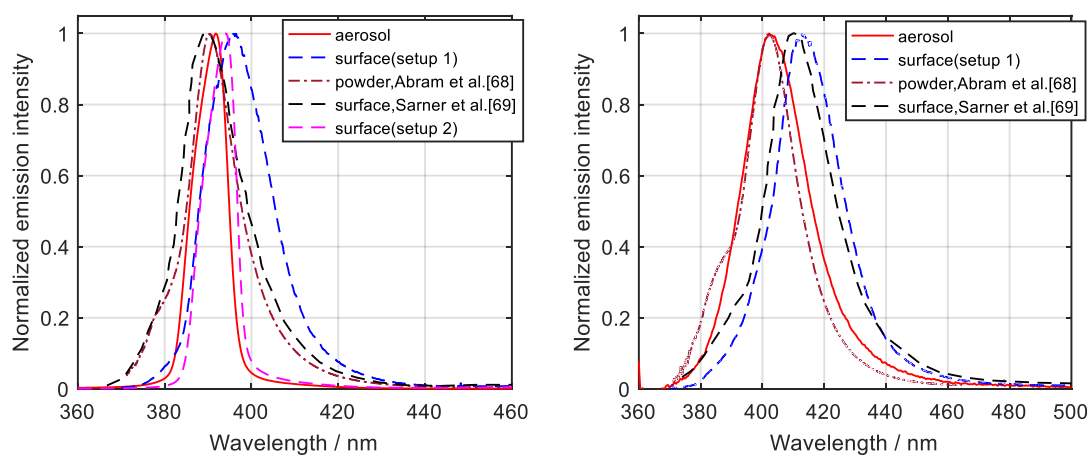


Figure 4-33: Comparison of ZnO:Zn emission spectra with the literature survey at 298 K (left) and 475 K (right). The red curves are the spectra obtained in the aerosol.

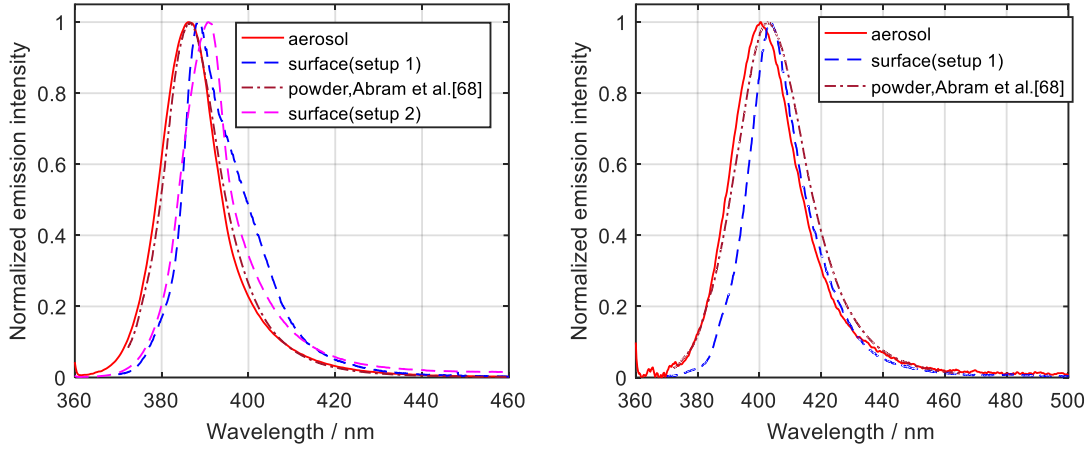


Figure 4-34: Comparison of ZnO emission spectra with literature data at 298 K (left) and 485 K (right). The red curves are the spectra obtained in the aerosol.

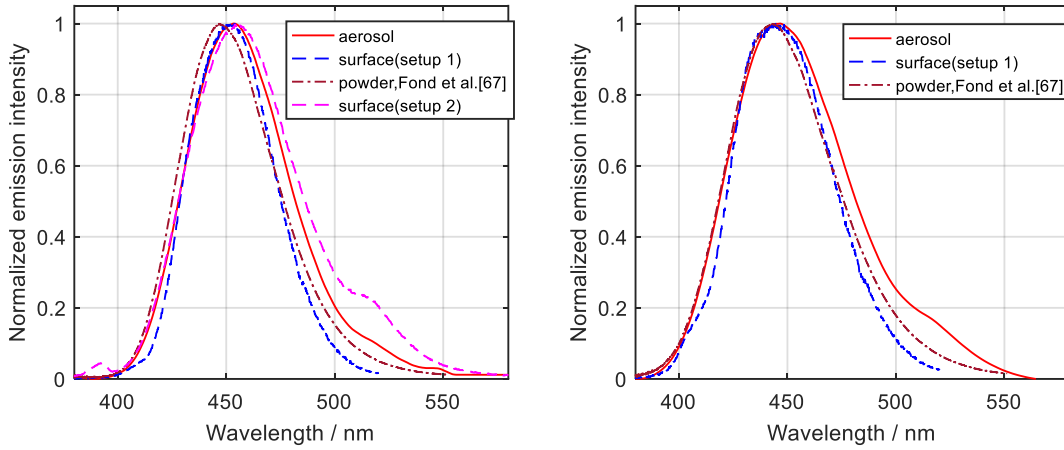


Figure 4-35: Comparison of BAM:Eu<sup>2+</sup> emission spectra with literature data at 298 K (left) and 500 K (right). The red curves are the spectra obtained in the aerosol.

## 4.6 Calibration procedure for two-color intensity-ratio method

The determination of temperature from the phosphorescence signal ratio requires calibration measurements that relate the intensity ratio to temperature. In this work, the calibration curves were calculated from the spectrally-resolved measurements based on the ratio of two signals obtained by convoluting the emission spectra with the transmission curves of the respective bandpass filters. At a given temperature, the collected signal on the channel  $S_j$  can be evaluated as follows:

$$S_j = \int QE(\lambda)\alpha_F(\lambda)I_s(\lambda, T) d\lambda \quad (16)$$

where  $\alpha_F$  is the transmission curve of the filter,  $I_s$  is the emission intensity,  $\lambda$  is the emission wavelength and  $T$  is the temperature. QE is the wavelength-dependent quantum efficiency of the camera that will be used for phosphorescence collection. The QE values were taken from the datasheet of the camera [88]. A fit of the measured intensity ratio is then used to evaluate the intensity-ratio images. The accuracy of the calibration curve depends on the accuracy of the determination of the particle temperature in the

---

calibration measurements and on the type of fitting method. It is important to note that the selection of the bandpass filters is not a simple task. In general, a compromise needs to be found between temperature sensitivity over a large temperature range while maintaining acceptable signal intensities on both channels.

#### 4.6.1 Selection of detection wavelengths

As discussed in the sections above, there are differences in the emission spectra of the phosphors depending on the two measurement conditions (coated surface and aerosol) that affect the temperature evaluation based on the intensity-ratio method. This aspect leads to an important source of error on the calibration that will be used for the engine measurements. Therefore, a comparison between the temperature dependence of the intensity ratio obtained from coated-surface and from aerosol conditions are analyzed to provide a temperature error estimation when using the emission spectra from coated-surface for gas phase measurements like engine conditions.

The temperature dependence of the intensity ratio obtained for the different phosphors from measurements on coated surfaces is presented in Figure 4-36. For the comparison coated-surface vs aerosol measurements, the interference filters were chosen to have a good temperature sensitivity over 300–700 K temperature range. For ZnO and ZnO:Zn the filters used are centered at  $425\pm 15$  and  $387\pm 11$  nm. For BAM:Eu<sup>2+</sup> the filters are centered at  $400\pm 20$  and  $458\pm 6$  nm. Note that ZnO phosphors show a stronger sensitivity to temperature compared to BAM:Eu<sup>2+</sup>.

From the intensity ratio curve obtained from coated-surface measurements, it can be seen that for a temperature variation of 1 K the corresponding change in intensity ratio is of the order of 5% for ZnO phosphors and only 0.2% for BAM over 300–500 K temperature range. For the filters used, ZnO and ZnO:Zn phosphors show similar sensitivity to temperature between 300 and 500 K.

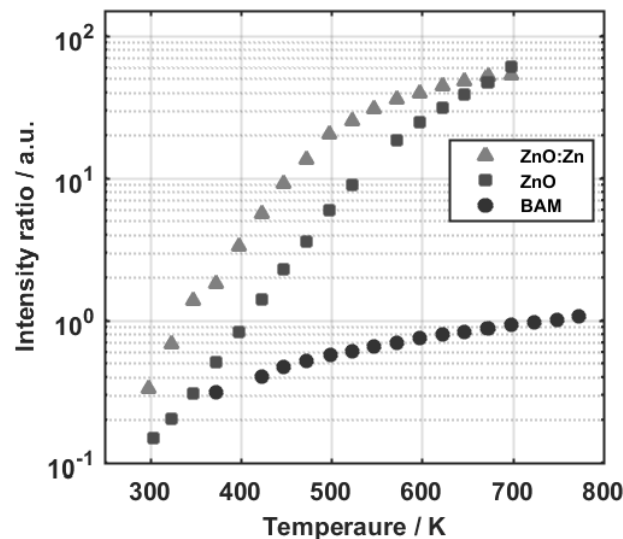


Figure 4-36: Temperature dependence of the signal intensity ratio of the selected phosphors obtained from measurements on phosphor-coated surfaces. The intensity ratio is obtained by applying the convolution of the emission spectra with the filters indicated in Table 4-1 (left).

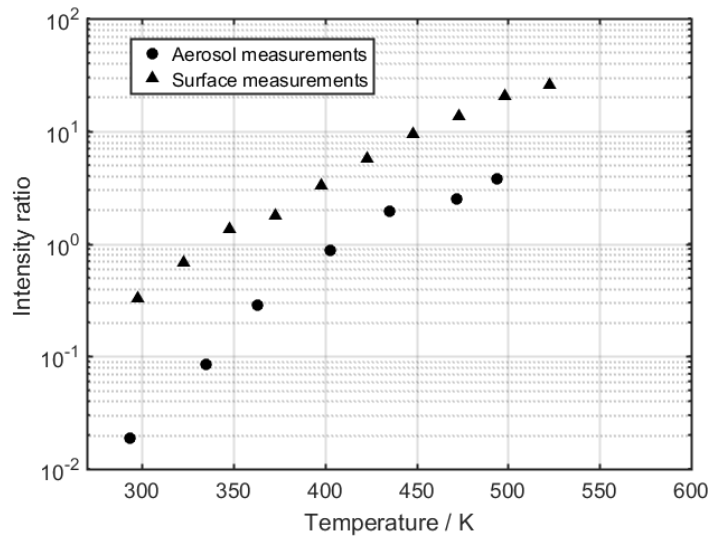


Figure 4-37: Comparison between the temperature dependence of the signal intensity ratio obtained in aerosol with the results obtained from measurements on ZnO:Zn-coated surfaces. The dots represent the resulting intensity ratio obtained from aerosol measurements. The triangles represent the intensity ratio obtained from surface measurements. The intensity ratio is obtained by applying the convolution of the emission spectra with the filters indicated in Table 4-1 (left).

Using the same selection of interference filters, the temperature dependence of the signal intensity ratio obtained from aerosol measurements can be equally calculated and compared with the temperature sensitivity estimated from surface measurements. This analysis was made for ZnO:Zn phosphor but it can be expanded also for the others phosphors as presented in section 4.5. The comparison between the temperature dependence of the signal intensity ratio obtained from surface and aerosol conditions with ZnO:Zn phosphor is presented in Figure 4-37. The signal intensity ratio curve obtained from aerosol measurements appears to be shifted towards the higher temperatures. An estimation of the temperature difference can be done using the signal intensity ratio curve obtained on surface to estimate the temperature of the aerosol measurements. From 300 to 500 K this shift is approximately constant and the temperature calculation is biased of approximately 80 K.

This estimation can be used to provide an idea of what would be the temperature error using the coated-surface measurements for the calibration purpose instead of aerosol measurements. Based on this analysis, for gas-phase thermometry, it is preferred to determine the calibration curve from aerosol measurements. Therefore, in this work, the calibration data for the engine measurements was determined using the emission spectra obtained from aerosol measurements.

Based on the results presented in section 4.5, ZnO:Zn phosphor shows a stronger sensitivity to temperature compared to BAM:Eu<sup>2+</sup>, providing increased temperature precision. Also, compared to ZnO, ZnO:Zn shows slightly higher luminescence intensities. In a harsh environment like an engine, it is preferable to choose a phosphor that shows strong sensitivity to temperature and strong emission. Therefore, ZnO:Zn was chosen as the most suitable candidate for engine measurements.

#### 4.6.2 Calibration data for temperature measurement

---

Following the characterization results from aerosol measurements, the calibration curve for the temperature calculation can be obtained. This curve has been obtained based on the optical setup that will be described in the next chapter for engine measurements. To better illustrate the choice of filters, the filter combination and the optical setup used for engine experiments is briefly introduced here.

To increase the luminescence signals over the two channels, and to enable the simultaneous installation of the PIV system required for T-PIV technique, a 45° dichroic mirror has been employed to separate the luminescence signal in the two channels, as shown in Figure 4-38. Also, two bandpass filters centered at  $507\pm 133$  nm and a dichroic long-pass with a cut-off at 410 nm (Chroma Technology) were chosen. Using this optical collection system, the two channels are only separated by the dichroic long-pass filter, maximizing the detected luminescence signal on both cameras.

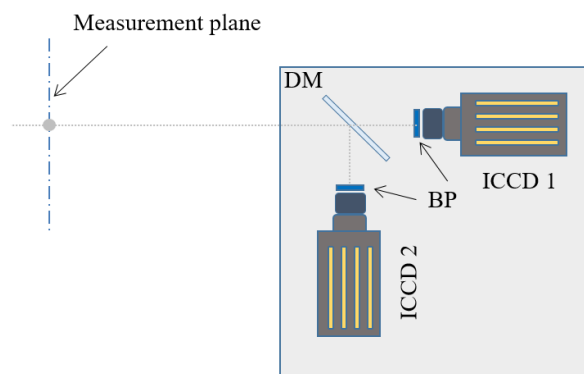


Figure 4-38: Camera arrangement for two-color imaging in IC engines.  
DM: Dichroic mirror, BP: bandpass filters.

The normalized emission spectra of ZnO:Zn with the transmission profiles of the filters used in this work are shown in Figure 4-39. The calibration curve is determined by convoluting the emission spectra with the transmittance of the interference filters and the dichroic mirror, Figure 4-40. The measured data points were then fitted using a quadratic curve and the confidence interval (dashed lines) was determined. The fit was used to predict the intensity ratio response as a function of the temperature. Based on the measured data points, this fit provides a quite well prediction of the temperature dependence of the measured ratio. The fitting process was performed using the least-squares method in a Matlab routine. The least-squares method is based on the minimization of the sum-of-squares and the resulting error is related to the squared term of the Gaussian distribution. This method is based on the assumption that the errors are normally distributed and follow a Gaussian distribution. In this work the resulting error from the fitting curve was evaluated at  $2\sigma$  (where  $\sigma$  is the standard deviation) corresponding to a 95% of the confidence interval. Almost all the measured points are contained in the confidence interval except few data points around 500 K, as shown in Figure 4-40. This small deviation can be attributed to an error on the temperature estimation of the spectroscopic measurements that will be presented in section 4.7. The curve shows that between 300 and 800 K, the intensity ratio of ZnO:Zn strongly depends on temperature. This filter combination was chosen to maximize the temperature sensitivity in the 600–800 K temperature range that is relevant near top dead center (TDC) under motored conditions.

It is important to note that the calculated confidence interval relative to the value of the ratio is smaller at higher temperatures due to the better quality of the fitting in this temperature range. On the other hand, at lower temperatures the measured points are more scattered causing an increase of the confidence

interval. This fact is mainly due to the combination of filters chosen to maximize the signal on both channels at higher temperatures. As shown in Figure 4-39, at lower temperatures the convoluting signal on the red channel is smaller relative to the blue one leading to larger uncertainties on the ratio calculation.

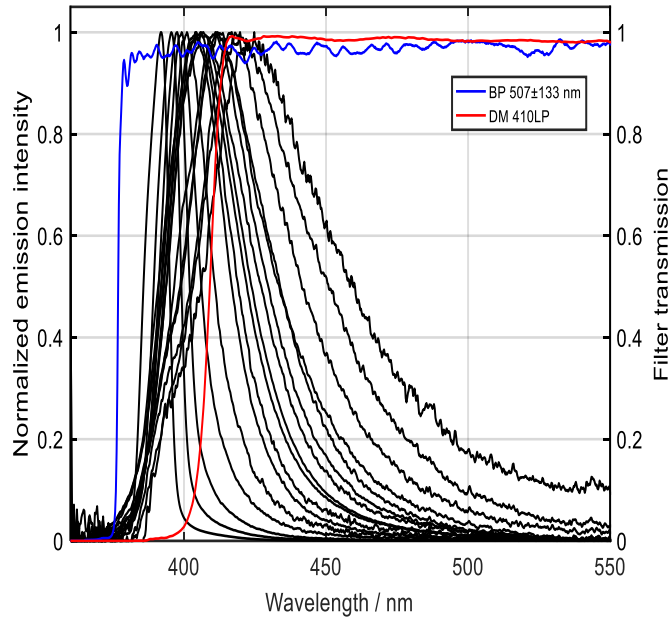


Figure 4-39: Normalized ZnO:Zn emission spectra recorded at different temperatures for aerosolized particles at 50 mJ/cm<sup>2</sup> laser fluence. The transmission profiles of the filters used for the calibration are shown in color. Blue: bandpass 507±133 nm, red: dichroic mirror 410LP.

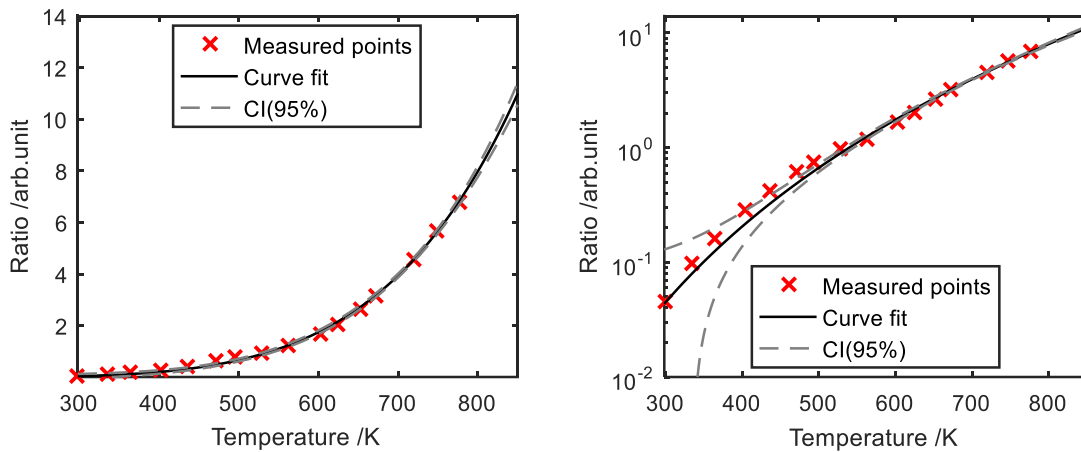


Figure 4-40: Left: Temperature calibration data for ZnO:Zn for the filter combination shown in Figure 4-39 with a quadratic fit to the measured data points (crosses). The dashed lines show the corresponding confidence interval of the calibration curve. Right: The same ratio curve on logarithmic scale to better visualize the differences between measurements and fit at low temperatures.

## 4.7 Uncertainty analysis

For the aerosol experiments, the measurement uncertainty was evaluated based on the repeatability of the emission spectra with the objective of estimating the resulting temperature error induced on the calibration curve. The calibration curve was calculated from the spectral data obtained in aerosol condition. For this reason, the uncertainty related to the collection of the spectra is directly related to the error on the calibration curve and therefore to the engine temperature measurements.

#### 4.7.1 Measurements uncertainty

A sequence of 100 single-shot measurements obtained with ZnO:Zn at 308 K flow temperature is presented in Figure 4-41. The red curve, shown in the figure, is the emission spectrum obtained by the accumulation of 100 successive spectra. The corresponding uncertainty was evaluated based on the dispersion of the single-shot measurements. The confidence interval was calculated to assess the measurements uncertainty. For  $N$  measurements the confidence interval of 95% is calculated by

$$U_{0.95} = \frac{2\sigma}{\sqrt{N}}, \quad (17)$$

where  $\sigma$  is the standard deviation [89].

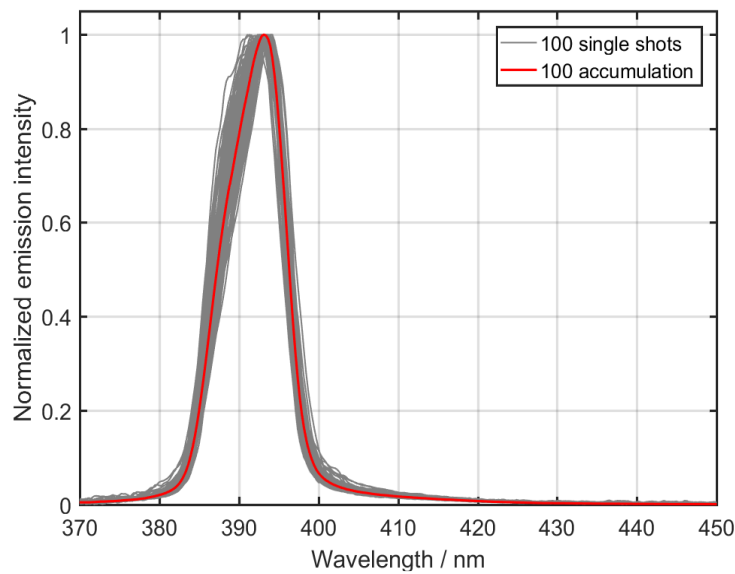


Figure 4-41: Sequence of 100 single-shot measurements obtained in aerosol condition with ZnO:Zn at 308 K. The red curve is the spectrum obtained by accumulating 100 successive spectra on the camera chip.

This approach was used to evaluate the corresponding temperature uncertainty of the measurements. The single-shot measurements were converted to temperature using the calibration curve obtained from the accumulation spectra in aerosol condition after convoluting the spectra with the filters spectral data, presented in Table 4-1. In Figure 4-42, the blue crossed points represent the resulting temperature from single-shot measurements. The red points show the resulting temperature calculated from the average of  $N$  single-shot measurements. The dashed line is the temperature determined from the accumulation of 100 spectra. After 100 measurements the calculated temperature converges to a constant value of 305 K with the corresponding confidence interval of 1.5 K, shown in Figure 4-42 (right). The confidence interval is improved by a factor of 2 when the number of samples is increased from 40 to 100. The

calculated confidence interval can be used as an estimation of the uncertainty related to the calibration curve thus the temperature evaluation.

The single-shot temperature uncertainty can also be estimated from single-shot measurements. Considering the temperature sensitivity obtained in aerosol (presented in section 4.6), the shot-to-shot fluctuation on the measured spectrum shown in Figure 4-41, corresponds to a temperature variation of about  $\pm 12$  K at 308 K.

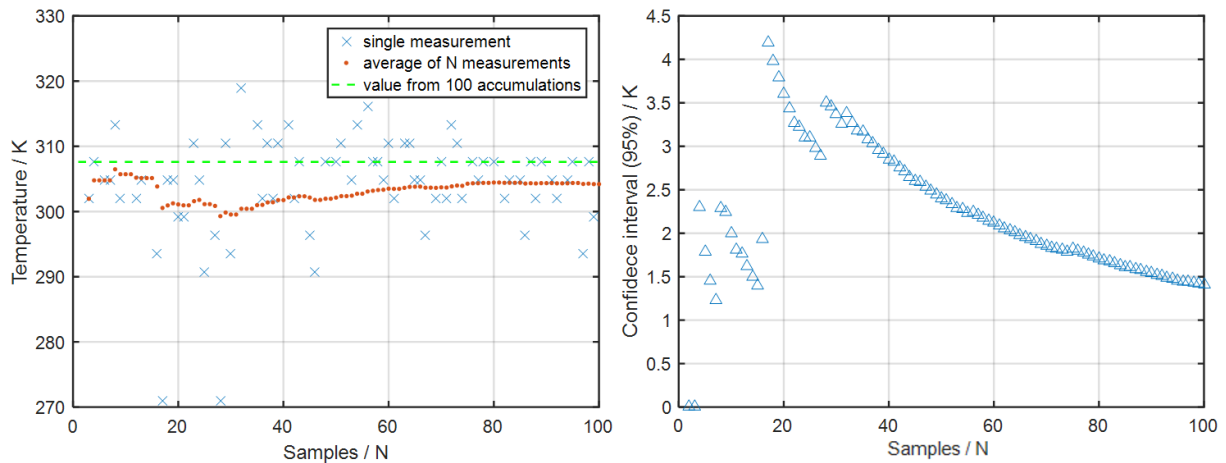


Figure 4-42: Left: Temperature evaluation from single-shot measurements using ZnO:Zn particles at 308 K (left). The blue crosses represent the resulting temperature from single-shot measurements. The red points show the resulting temperature calculated from the average of  $N$  single-shot measurements. The dashed line is the temperature evaluated from the accumulation of 100 spectra. Right: The corresponding confidence interval based on the average of  $N-1$  measurements as a function of the number of samples evaluated.

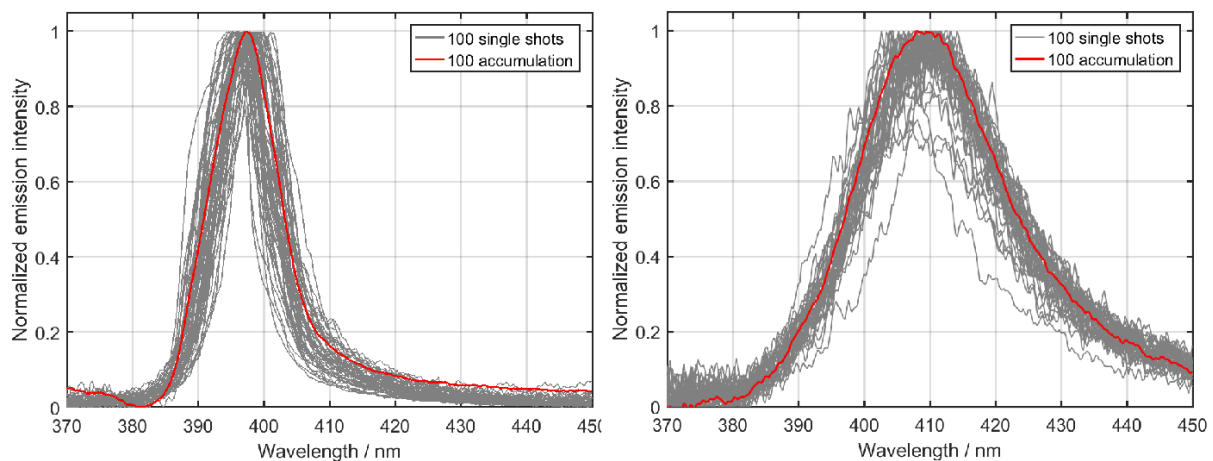


Figure 4-43: Sequence of 100 single-shot measurements obtained in gas-phase condition with ZnO:Zn at 375 K (left) and 600 K (right). The red curve is the spectrum obtained by accumulating 100 successive spectra on the chip of the camera.

The same measurements were also performed at 375 and 600K. At higher temperature the measurement uncertainty increases due to the drop of the luminescence intensity and the consequent lower SNR. Figure 4-43 shows the dispersion of the single-shot measurements obtained at 375 and 600 K. At these temperatures the corresponding confidence interval is respectively of 5 and 7 K.

Figure 4-44 shows the results obtained with ZnO at 305 and 600 K. At 600 K some double peak structure appears in the spectrum. This feature might be the consequence of some cold particles recirculation in the hot jet. Their contribution in the spectrum, due to the relatively higher luminescence intensity is strongest compared to the intensity level of hottest particles. This also contributes to the increase of the measurement uncertainty. The corresponding confidence interval is 5 K at 305 K and 7 K at 600 K. Figure 4-45 shows the results obtained with BAM:Eu<sup>2+</sup>. Using BAM:Eu<sup>2+</sup> particles, the shot-to-shot signal variation is smaller compared to the case with ZnO. This fact is mainly due to the weaker temperature dependence of the spectra combined with relatively higher luminescence intensity at higher temperatures. At 610 K some of the emission spectra of BAM:Eu<sup>2+</sup> shows a pronounced second peak around 510–520nm. This second emission peak might be generated by some impurities contained in the phosphor material.

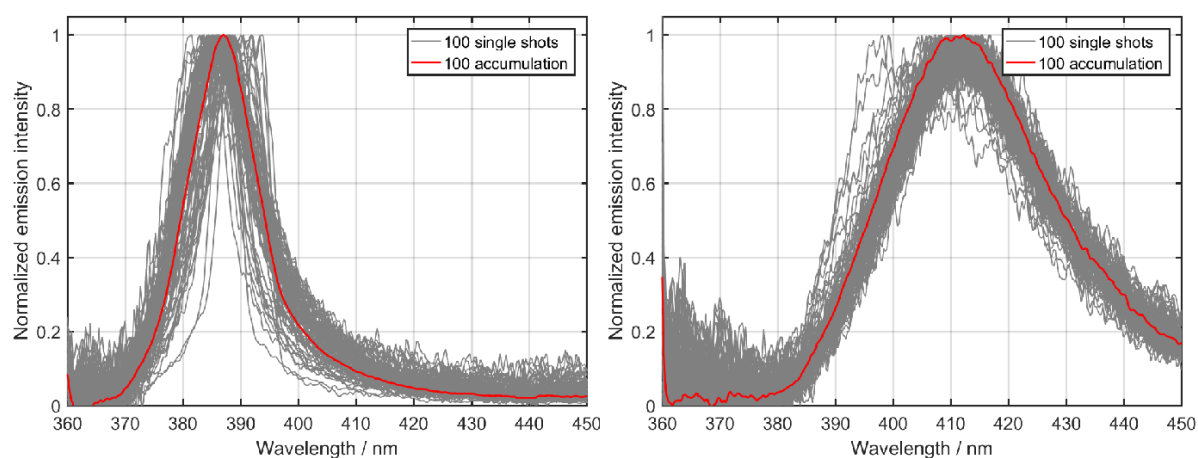


Figure 4-44: Sequence of 100 single-shot measurements obtained in aerosol condition with ZnO at 305 K (left) and 600 K (right). The red curve is the average of 100 spectra.

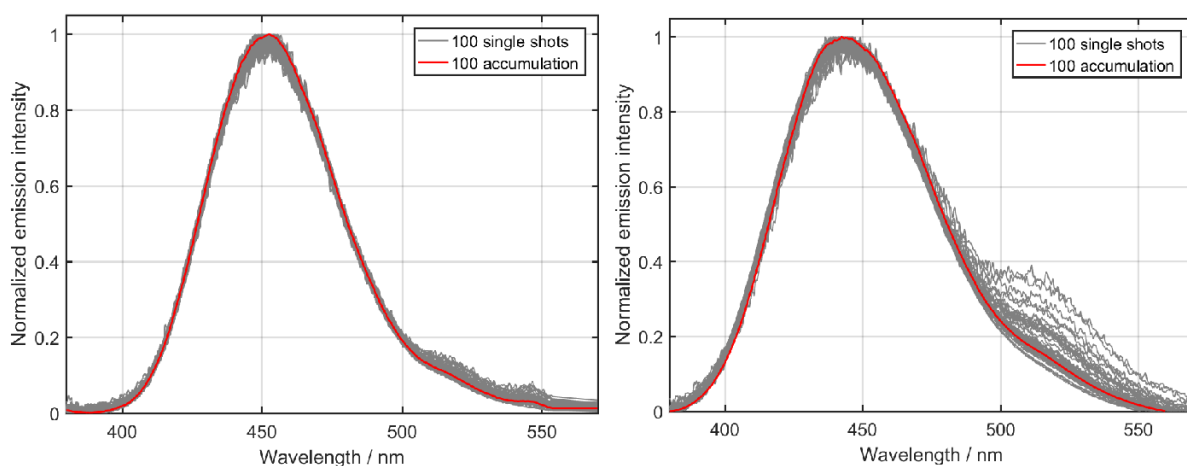


Figure 4-45: Sequence of 100 single-shot measurements obtained in aerosol condition with BAM:Eu<sup>2+</sup> at 305 K (left) and 610 K (right). The red curve is the average of 100 spectra.

---

---

---

## 5 APPLICATIONS OF THERMOGRAPHIC PIV IN AN IC ENGINE

This chapter contains the results regarding the application of thermographic PIV in an optically-accessible IC engine. Thermographic PIV is applied under motored conditions to evaluate the performance of the measurement technique. ZnO:Zn phosphor particles are used as a tracer for temperature and velocity fields. Time-averaged and single-shot images are presented demonstrating the feasibility of the technique in a confined harsh environment. The obtained temperature fields are compared with simulated bulk-gas temperatures from a zero-dimensional model-based simulation. The reliability and consistency of the results is also investigated by performing additional measurements applying parametric variation to the boundary conditions, in presence of spray injection and under fired condition.

### 5.1 Context

In this work, a pent-roof gasoline engine was chosen as an experimental test case where strong tumble motion of the in-cylinder gases is known to significantly affect heat losses [90,91]. On one hand, tumble is known to increase the burning rate and thus the thermal efficiency of an engine. On the other hand, tumble increases the wall heat transfer and thus heat losses decreasing the thermal efficiency of an engine. Understanding the interplay of fluid motion and heat losses is therefore critical for optimizing engine efficiency. Therefore, thermographic PIV is an ideal method to assess both quantities simultaneously. A pent-roof engine geometry, however, limits the optical access to only a part of the combustion chamber. Measurements close to top dead center (TDC) are therefore not possible because in this phase, the piston blocks the windows in the cylinder liner.

### 5.2 Experiment

#### 5.2.1 Characteristics of the optically-accessible engine

A four-valve double over-head camshaft (DOHC) four-stroke research engine manufactured by IFPEN was used for the experiments. The engine is described in detail in Ref. [92]. The engine is a single-cylinder direct injection spark-ignition (DISI) engine with a bore of 77 mm, a stroke of 85.8 mm, and a displacement of 399.5 cm<sup>3</sup>. The engine is equipped with a tumble intake port, a pent-roof cylinder head, and a flat piston crown. The injector and spark plug are centrally mounted in the symmetry plane between the intake valves and the exhaust valves. Optical access is provided through a fused-silica cylinder liner. This element limits the permitted in-cylinder pressure and the maximum thermal load. This configuration can therefore be used only in motored conditions or in skip-fired mode.

The intake port of the cylinder head can be equipped with a particular tumble adapter to change the aerodynamic flow into engine. This tumble adapter is shown in Figure 5-1. A pronounced rotating flow can be generated by this intake configuration. The shape of the adapter generates an ~15% increase of the tumble movement compared to experiments without the adapter. This was previously verified with experiments on a static flow bench [92]. In this work, thermographic PIV was applied on two configurations: reference and increased tumble conditions respectively without and with tumble adapter.

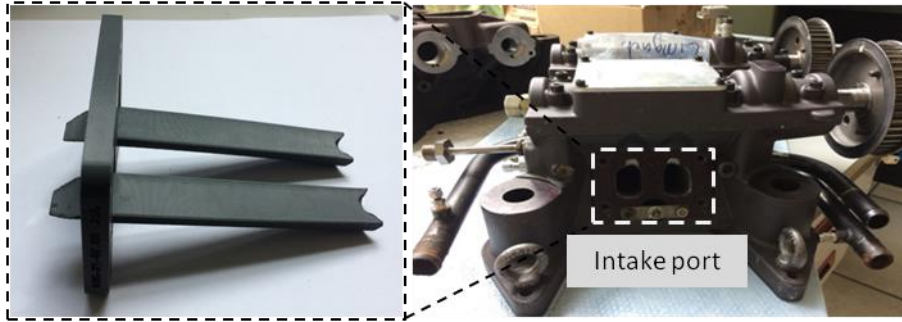


Figure 5-1: Detail of the tumble adapter used to increase the level of rotating flow into engine. The adapter can be introduced into the intake port.

The intake ducts were equipped with a heating jacket to increase the gas temperature at the intake port. Two configurations were studied during this work: A reference and an increased temperature condition at 298 and 333 K, respectively. The operating conditions and the main characteristics of the test engine are listed in Table 5-1.

Measurements were conducted at 1200 rpm, which corresponds to a cycle frequency of 10 Hz. A crank-angle encoder was used to measure the engine speed and the crank-angle position. These signals were used to synchronize the lasers and the cameras to obtain images at a determined crank-angle degree ( $^{\circ}\text{CA}$ ). The synchronization and the triggering of the signals were controlled via the dedicated test-bench software SynAll.

The water cooling system and the oil circuit of the engine were preheated to  $50^{\circ}\text{C}$  for 30 min before each measurement run. Afterwards, the engine was motored for several cycles before acquiring images to reach stationary thermal conditions as indicated by the stable gas temperature measurements of the thermocouples placed at the intake and exhaust manifolds.

Table 5-1: Main characteristics of the optical engine used in this work.

<b>Engine characteristics</b>			
Engine speed	1200 rpm	Exhaust valve close (EVC)	$13^{\circ}$ before TDC
Intake pressure	0.7 bar	Valve event duration	
Intake temperature	298 K, 333 K	- Intake	$186^{\circ}$
Displacement	$399.5 \text{ cm}^3$	- Exhaust	$207^{\circ}$
Geometric CR	10.5:1	<b>Injection specifications</b>	
Bore	77 mm	Injector type	Bosch HDEV 5.2
Stroke	85.8 mm	Operating pressure	200 bar
Con. rod length	144 mm	Injection duration	1 ms
Valve diameter intake/exhaust	28 mm, 25.3 mm	Injection timing	$170^{\circ}\text{CA}$ , $220^{\circ}\text{CA}$
Valve lift intake/exhaust	9.5 mm	Number of holes	5
		Spray angle	$110^{\circ}$

TDC denotes the gas exchange top dead center, IVO and EVC are calculated at 0.7 mm valve lift

### 5.2.2 Particle seeding system

The in-cylinder flow is seeded with 3.5- $\mu\text{m}$  diameter ZnO:Zn phosphor particles (GK30, Phosphor Technology) upstream of the intake manifold in order to generate an homogeneous particle distribution into the engine. The seeding system was the same as the one used for the characterization setup described in section 4.3. The particles were mixed with Aerosil nanoparticles and then dried into the oven at 150°C for at least 4 h to avoid particle agglomerations, following the procedure described in the section 4.3.

The air mass flow rate needed for the seeding system is lower than the total air mass flow needed from the engine. Therefore, a sonic nozzle of 1 mm diameter was used to independently control the flow through the seeder. The total mass flow coming into the engine is therefore the sum of the mass flow passing through the seeder and the main mass flow passing through the intake plenum, which is controlled by another sonic nozzle. The total mass flow rate was controlled downstream (inlet of the intake manifold) by pressure and temperature measurements. The size of the sonic nozzle was adjusted to provide the same particles seeding density as the one used for aerosol characterization (cf. discussion in section 4.3). It is important to note that the seeding density is varying during engine cycle due to the piston displacement and therefore the sonic nozzle adjustment was performed to generate the right amount of seeding density at 180°CA (corresponding to bottom dead center, BDC). The particle seeding density was measured using the particles counting system described in section 4.3. Seeding densities from  $\sim 1 \times 10^{11}$  to  $\sim 3 \times 10^{11}$  particles/ $\text{m}^3$  at 180 and 330°CA were measured respectively when a sonic nozzle of 1 mm in diameter was used. This range of seeding density was found to provide the best compromise in term of spatial resolution between PIV and phosphor thermometry measurements. An example Mie scattering image of the seeded in-cylinder flow obtained at 180°CA is shown in Figure 5-2(right).

### 5.2.3 Optical measurement system

For thermometry, the phosphor particles were excited using the third harmonic of a Nd:YAG laser (Spectra-Physics, Quanta-Ray CGR-150), operated at 10 Hz. At this repetition rate, the frequency-tripled output of the laser at 355 nm was adjusted to 20 mJ/pulse, which corresponds to a laser fluence of 50 mJ/ $\text{cm}^2$  in the measurement volume. The laser beam was formed into a laser sheet using the combination of cylindrical lens ( $f_2 = -100$  mm) and a spherical lens ( $f_1 = 1000$  mm) to form a 500- $\mu\text{m}$  thick light sheet when entering the engine cylinder. The laser sheet was adjusted to provide a vertical viewing plane intersecting with the axis of the engine cylinder, as shown in Figure 5-2. The full arrangement of the optical setup is shown in Figure 5-3.

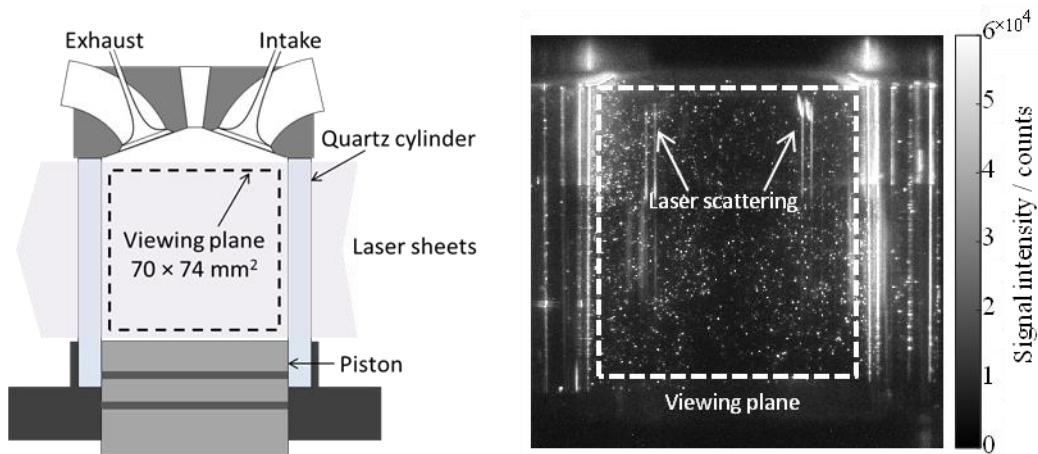


Figure 5-2: Schematics of the optically accessible cylinder (left) with the laser light sheet passing through the fused-silica cylinder liner. Raw Mie scattering image of the particle-seeded in-cylinder flow at 180°CA. Note the multiple laser scattering from the various surfaces of the cylinder liner interfering in the viewing plane.

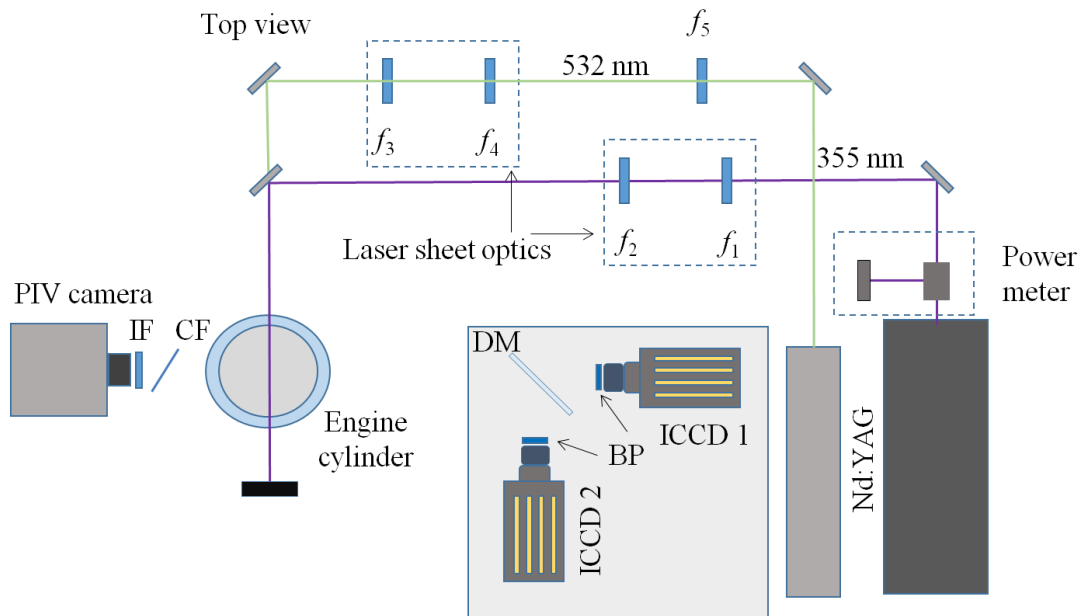


Figure 5-3: Experimental setup used for in-cylinder temperature and velocity measurements.

The phosphorescence signal was collected by two intensified CDD cameras (PIMAX2, Princeton instrument, 16 bit, 1024×1024 pixels) equipped with 50 mm  $f/1.2$  Nikon lenses. Since the luminescence lifetime of the ZnO:Zn is on the nanosecond scale, the exposure time of the cameras was set to 100 ns. This ensures that the camera collects the signal during the entire phosphorescence decay. The two ICCD cameras were equipped with two interference filters centered at  $507 \pm 133$  nm. A dichroic mirror (long-pass 45° mirror at 410 nm) was used to separate the two wavelength bands used for thermometry measurements and to direct the respective phosphorescence light to either cameras.

Table 5-2: Characteristics of the filters and cameras used in this work.

<b>Optical setup</b>		<b>Type of phosphor</b>	<b>Particle size</b>
Image area	75×80 mm <sup>2</sup>	ZnO:Zn	3.5 μm
Laser sheet width	80 mm		
Laser sheet thickness	0.5 mm	<b>Thermometry cameras</b>	
Cylindrical lens	$f_2, f_3 = -100$ mm	ICCD binned 2×2 – PIMAX2	512×512 pixels
Spherical lens	$f_1 = 1000$ mm	Objective	Nikon 50 mm <i>f</i> /1.2
	$f_4 = 1100$ mm	Pixel size	208×208 μm <sup>2</sup>
	$f_5 = 2000$ mm	Spatial resolution (Target USAF)	280 μm
<b>Filters and mirrors</b>		<b>PIV camera</b>	
Dichroic mirror	T410lpxt	High speed CCD – Photron SA1	832×1008 pixels
Filters	BP: 507 ± 133 nm	Objective	Nikon 50 mm <i>f</i> /1.2
	IF: 532 ± 10 nm	Pixel size	102×102 μm <sup>2</sup>
	CF: OG515		

The resulting transmission curves of the filter/dichroic mirror combination are shown in Figure 4-39 and the respective details are given in Table 5-2. It is important to note that for dielectric mirrors, the spectral reflection characteristics depend on the angle of incidence and the polarization of the light. Therefore, the deviation in incident angles on the mirror – that is unavoidable in an imaging arrangement – changes the effective wavelength characteristics compared to the specified ideal values. The resulting change in bandpass characteristics for both detection channels influences the evaluation of signal ratio. For future measurements it is recommended to choose a filter combination where this effect does not influence the detection range (i.e., the bandpass filters should be well-separated spectrally from the edge of the dielectric filter). In this work, the errors induced by the angle-sensitivity of the dichroic mirror were not taken into account.

During readout, 2×2 pixels binning was chosen to increase the signal-to-noise ratio (SNR) by reducing shot noise. Figure 5-4 shows an assessment of the linearity of the detector. The test was performed by imaging light from a LED inside an integrated sphere. Considering stable emission of the light source, the measurements were performed with various neutral density filters in front of the cameras to cover the entire dynamic range of the camera. The left frame in Figure 5-4 shows results without pixel binning for three gain levels between 150 and 250 (255 being the maximum setting). The figure shows that a linear response was only observed up to ~18000 counts, (approximately 20% of the total dynamic range). The expected increase in count rate by a factor of 4 after 2×2 binning resulted in a linear access to the entire dynamic range of the camera read out and was thus used for thermography experiments in our case.

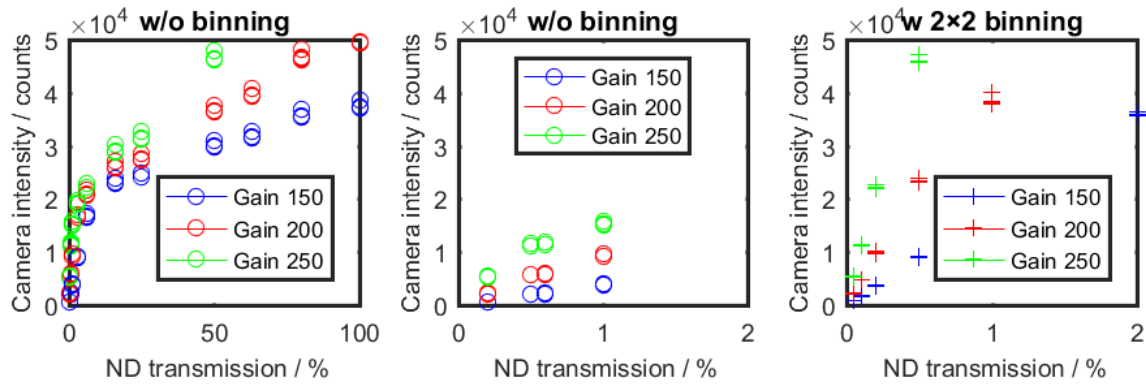


Figure 5-4: Linearity tests of the intensified cameras. The results are obtained from measurements with an LED-illuminated integrating sphere for different gain settings and with 2×2 binning (right).

The detector with 2×2 binning provides a field of view of 70×74 mm<sup>2</sup> with a 208 μm projected binned pixel size, as shown in Figure 5-2. The spatial resolution of the temperature imaging setup was measured by imaging a 1951 USAF resolution target placed in the measurements plane. The obtained spatial resolution was found to be approximately 353 μm. Note that this spatial resolution is not the final spatial resolution of the temperature maps because of the data processing discussed later in section 5.4.

Severe vignetting was observed when imaging near TDC. The vignetting was mostly due to the piston partially blocking the detection solid angle. To avoid this phenomenon, the two cameras were mounted on a metal lifter plate. For crank angles near TDC, the cameras were lifted so that their axes were aligned with the center of the measurement zone. Thanks to this adjustment, vignetting was significantly reduced.

### 5.3 Particle image velocimetry (PIV) system

For PIV, a dual-cavity, frequency doubled Nd:YAG laser (Hawk-duo, Quantronix) was operated at 2.5 kHz with a pulse separation of 30 μs. The laser energy was adjusted to 5 mJ/pulse for all the measurements. The 532 nm laser beam was formed into a laser sheet using the combination of cylindrical lens ( $f_3 = -100$  mm) and a spherical lens ( $f_4 = 1100$  mm). The thickness of the laser sheet was adjusted to match the thickness of the 355 nm sheet with a third spherical lens ( $f_5 = 2000$  mm) placed ahead the laser sheet optics. The 532 nm laser sheet was overlapped with the 355 nm laser sheet using a high-reflectivity 355 nm, high-transmissivity 532 nm dichroic beam splitter.

The Mie scattered light was imaged using CMOS camera (Photron SA1.1, 12 bit, 1024×1024 pixels) equipped with a 50 mm  $f/1.2$  Nikon lens and a 532±10 nm interference filter. The PIV camera was placed at the opposite side of the engine cylinder compared to the thermography detection setup (Figure 5-3). A color glass filter (Schott OG515), suppressing wavelengths lower than 515 nm was placed at 45° in front of the camera (CF in Figure 5-3) [49]. This filter was used to suppress reflections from the interference filter placed on the opposite side.

The camera was operated at 5 kHz, corresponding to an image dimension of 832×1008 pixels with a projected pixel size of 102 μm. The corresponding timing diagram with exposure times and gate delays used for cameras and lasers synchronization with the engine timing (main trig) is shown in Figure 5-5.

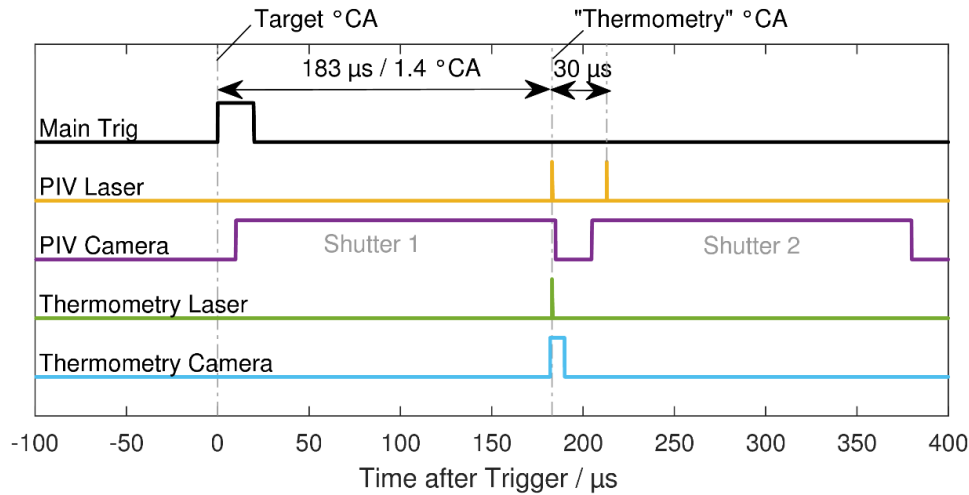


Figure 5-5: Timing diagram for triggering and exposure settings for cameras and lasers.

## 5.4 Image processing and measurements strategy

### 5.4.1 Image processing

The image processing leading to temperature images followed the procedure shown in Figure 5-8. The first step is background subtraction. For each analyzed crank angle degree a background image was measured for each camera based on the signal averaged from 200 engine cycles with the laser running without particle seeding. Then, the averaged background images were subtracted from the luminescence intensity images taken with the respective ICCD cameras. Examples of raw luminescence images before and after background subtraction are shown respectively in Figure 5-6 and Figure 5-9. It is important to note that in the central part of the images, the particles appear less sharp. This effect was found to originate from the wear of the cylinder surface caused by the friction between the particles and the piston rings on the cylinder walls.

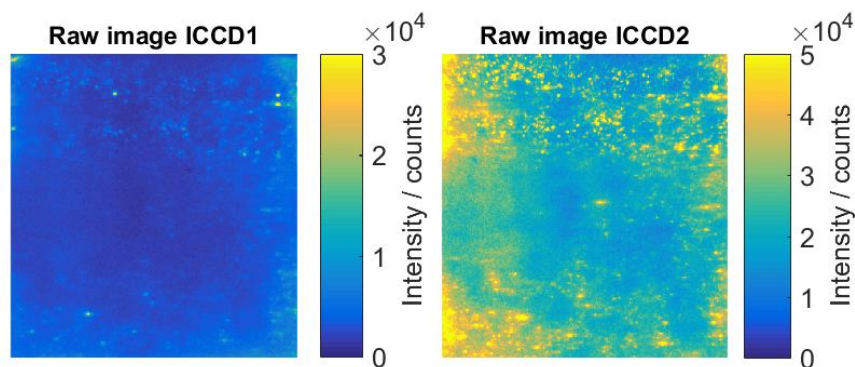


Figure 5-6: Example of single-shot raw phosphor luminescence images taken from camera 1 and 2 at 240°CA.

Both cameras are then mapped on each other to provide images with the same coordinate reference system. This is especially important when using two-color intensity ratio method. Because in phosphor thermometry the luminescence originates from small discrete particles, already a minor misalignment

---

of both images strongly affects the ratio image. The image mapping was performed based on measurements of a double-sided calibration plate (LaVision 106-10) positioned in the measurement plane to not only map the two cameras used for phosphor thermometry but to also align the measurements with the PIV measurement. The acquired images from both phosphor thermometry cameras were post-processed by DaVis 8.0 (LaVision) to create a mapping matrix that is then applied to the luminescence images.

Cut-off filters were applied after background subtraction from both camera images: the pixels having a count level lower and higher of respectively  $th_{\text{slow}}$  and  $th_{\text{high}}$  were not considered for the ratio image calculation. The pixels below  $th_{\text{slow}}$  were excluded because the local signal is considered to be caused by reflections and multiple scattered signal and thus to ensure that the ratio was calculated only on direct phosphor luminescence. On the other hand, pixels with intensities above  $th_{\text{high}}$  were excluded because the respective luminescence levels were too close to the saturation threshold of the detector causing non-linear signal response. The cut-off thresholds were set the 10 and the 90% of the dynamic range of each camera. Afterwards, a  $5 \times 5$  pixel median filter was used to reduce the noise amplitude in the images. The size of the median filter was chosen as a compromise to improve the signal-to-noise ratio and limit the reduction in spatial resolution. As discussed later in the paragraph, with this filter the final spatial resolution was better than 2 mm.

The ratio image is calculated by pixel-by-pixel division of the two post-processed images. While inhomogeneities in the laser light sheet distribution cancel (they are the same in both images), local variations in the signal detection with the two cameras (such as vignetting effects and variations in pixel sensitivity) affect the ratio. To correct for this effect, a (specific case) of flat-field correction is applied to the ratio image. The ratio measured under the conditions of interest is divided by the signal ratio measured at  $180^\circ\text{CA}$ , where the in-cylinder temperature distribution is expected to be close to uniform. Figure 5-7, shows the ratio images obtained before and after this correction. It is interesting to note how this correction enables to reduce the horizontal asymmetric variation of the ratio. As a matter of fact, the observed asymmetry of the ratio, is not expected to be related to inhomogeneities of the in-cylinder temperatures. Otherwise, this effect is supposed to be caused by the angular dependence of the transmission/reflection properties of the dichroic mirror used to separate the two channels (cf. Figure 4-39 and discussion in section 4.6). Therefore, the correction used in this work allow to minimize the temperature error distribution induced by the dichroic mirror.

In order to relate the measured ratio to the temperature measurement, the calibration curve shown in Figure 4-40 is adopted by employing the following approach: The temperature at  $180^\circ\text{CA}$  is derived from a 0D simulation (Simcenter Amesim) described later in the chapter. Considering the expected accuracy of 0D simulation at this crank angle ( $180^\circ\text{CA}$ ), this value is used as reference temperature. The spatially-averaged ratio obtained at the same crank angle is then used to normalize the calibration curve to this value for the reference temperature. The resulting normalized calibration curve is then used to convert the ratio images to temperature images.

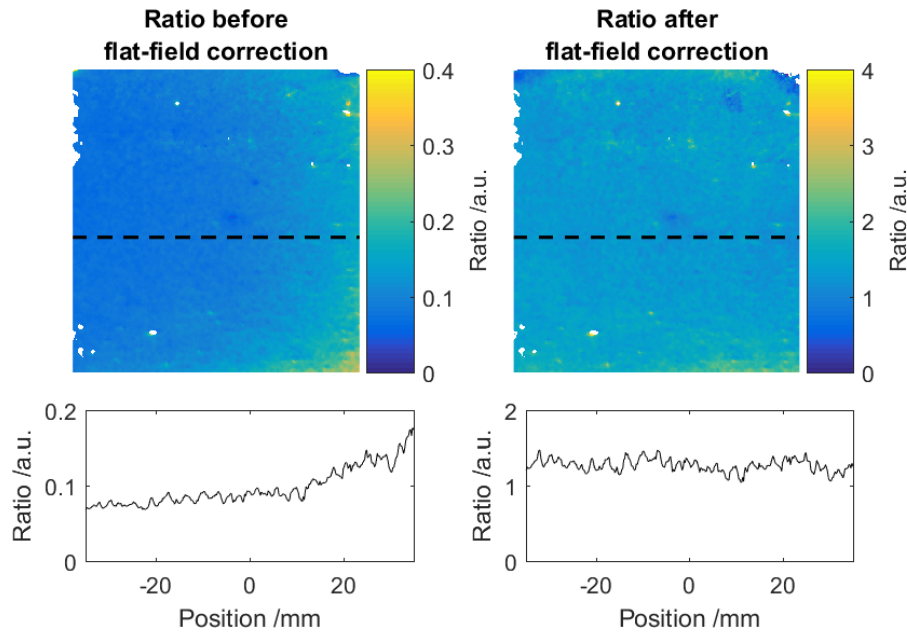


Figure 5-7: Example of ratio images obtained with the image processing algorithm using the single-shot phosphor luminescence images shown in Figure 5-6. The ratio image before (left) and after (right) flat-field correction is presented. In the bottom, the horizontal ratio profiles corresponding to the dashed line on both images are plotted. Measurements are taken at 240°C.

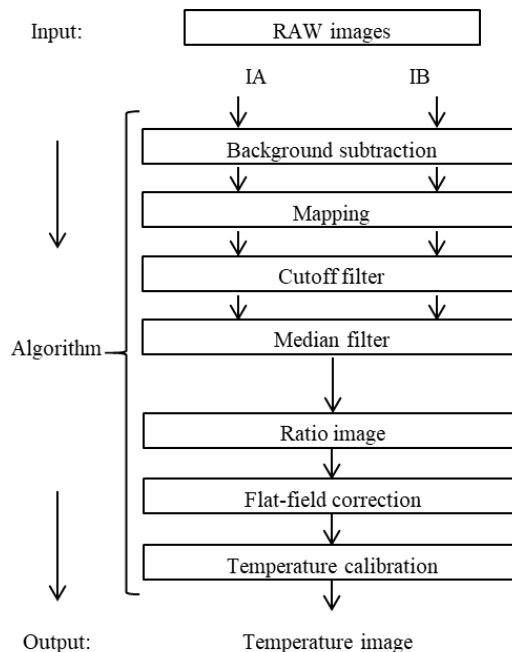


Figure 5-8: Image processing algorithm used to convert raw phosphor luminescence images into temperature fields. The algorithm is based on the two-color intensity ratio method.

An example of the image processing at 240°C is presented in Figure 5-9, where the luminescence images are background-subtracted, the resulting ratio and the corresponding temperature image are shown. The spatial resolution of the temperature image was obtained by applying the image processing algorithm to 1951 USAF target image. It was found that the temperature images have a spatial resolution

between 1.4 and 1.6 mm, corresponding to 7–8 pixels. The spatially-averaged bulk temperatures were calculated in a  $298 \times 24$  pixel region in the temperature images, as shown in Figure 5-9.

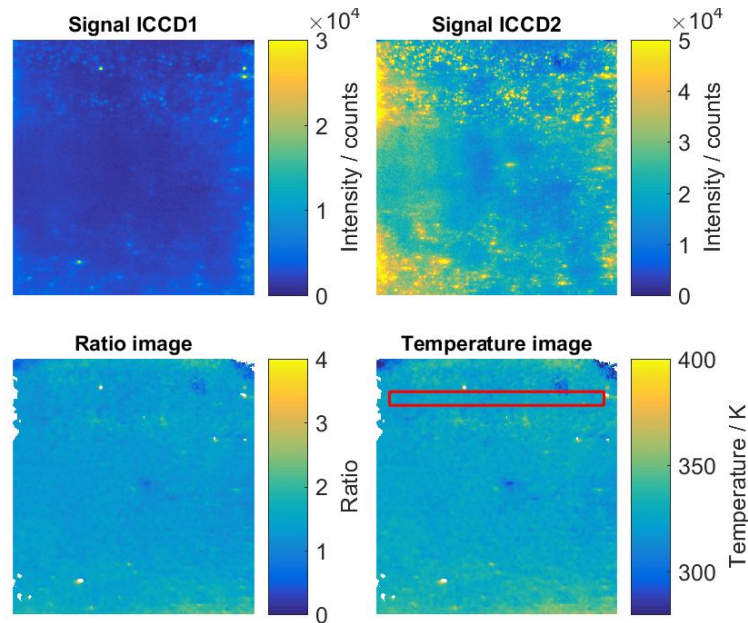


Figure 5-9: Example of image processing data results: Single-shot background-corrected luminescence images from camera 1 and 2 (top), the corresponding flat-field-corrected ratio image and the temperature image (bottom). The data correspond to an engine timing of  $240^\circ\text{CA}$ . The rectangle in the temperature image outlines the region considered for determining the temperature precision in comparison with spatially-averaged bulk temperature calculations.

For PIV, the Mie scattering images were mapped to have the same coordinate reference system as the temperature images. This was done by post-processing in DaVis. PIV images were then processed using a multi-pass cross-correlation algorithm (DaVis 8, LaVision) with iteratively decreasing the interrogation window size from  $64 \times 64$  to  $16 \times 16$  pixels and 50% overlap, leading to a final vector resolution of  $1.6 \text{ mm}^2$ .

## 5.5 Measurements strategy

The measurements were performed at an engine speed of 1200 rpm with a sampling rate of 10 Hz between  $180$  and  $540^\circ\text{CA}$ . Data sets were acquired at fixed crank angle over 200 consecutive engine cycles. The measurement sequence was applied for data collection:

- **Background image collection:** Background images are taken over 200 consecutive engine cycles taking into account the scattering of laser light in the absence of particles.
- **Particles seeding activation:** Particles seeding is activated and the engine is operated for 5–10 cycles until the seeding system operates steadily. Mie scattering images are used to monitor the homogeneity of the particle distribution.
- **Temperature and velocity image collection:** Once the seeding is stabilized, temperature and velocity images over 200 consecutive engine cycles are taken. This is the actual measurement phase.

After each measurement sequence, a visual inspection on the wear of the transparent cylinder is carried out because particles tend to stick to the cylinder wall and the friction with the graphite piston rings blackens the cylinder walls. In general, after three measurement sequences, it was necessary to dismount the cylinder for cleaning. A comparison among a new transparent cylinder, a cylinder used for three measurement sequences and a cleaned cylinder is presented in Figure 5-10.

Additionally, the cylinder head walls were coated with low-reflectivity black paint to reduce interfering luminescence generated from particles attached to the surface at each cleaning procedure.



Figure 5-10: Wear of the transparent cylinder after the acquisition of three data sets corresponding to 600 engine cycles. Note the intensity of black traces on the cylinder walls.

In order to evaluate the consistency of the phosphor thermometry results, measurements were conducted in a series of engine operating conditions. As a first step, only the temperature measurements were performed under two intake temperature conditions: reference ( $T_{\text{intake}} = 298 \text{ K}$ ) and increased intake temperature ( $T_{\text{intake}} = 333 \text{ K}$ ). In the second step, the temperature measurements are combined with PIV (T-PIV) and two engine configurations were studied: reference (tumble = 1.1) and increased tumble (tumble = 1.25). In the second case, an aerodynamic insert was added to the intake port with the aim of modifying the in cylinder motion. The tumble number refers to the methodology presented in Ref. [92] and the higher is the number the stronger is the tumble motion.

A further experiment was performed by applying T-PIV by measuring in presence of a fuel spray directly injected within the chamber. Finally, the ability of the particles to survive combustion event was tested by performing measurements in fired condition. The test cases are summarized in Table 5-3.

Table 5-3: Table of studied test cases for temperature and velocity measurements.

Test cases	Intake temperature	Tumble	Engine conditions
<i>Reference</i>	298 K	1.1	Motored
<i>Increased <math>T_{in}</math></i>	333 K	1.1	Motored
<i>Increased tumble</i>	298 K	1.25	Motored
<i>Direct Injection</i>	333 K	1.1	Motored – Injection
<i>Particles survivability</i>	298 K	1.1	Fired

---

## 5.6 Experimental results

### 5.6.1 Reference condition

Measurements were performed at the reference condition with an intake temperature of 298 K. The temperature images were acquired during the compression and expansion strokes under motored conditions over 200 engine cycles. The time-averaged in-cylinder temperature images are shown in Figure 5-11. The measured temperature fields are presented from 200 to 500°C<sub>A</sub> with an interval of 20°C<sub>A</sub>. During compression and expansion, the field of view changes according to the piston position preventing measurements between 330 and 390°C<sub>A</sub>. The piston with rings is illustrated by a grey rectangle, in Figure 5-11. The white zones on the images show the areas where local poor particles number density and/or higher intensity pixels prevent from any temperature processing.

In order to verify the temperature spatial distribution the horizontal temperature profiles, obtained along the red dashed line in Figure 5-11 is shown in Figure 5-12. The time-averaged temperature images show a uniform in-cylinder temperature distribution, however some systematic non-uniformities are observed. Some features like vertical and horizontal lines are caused by artefacts due to the progressive wear of the cylinder surfaces, as shown in Figure 5-11. Other features include some areas where the background correction was not sufficient to eliminate laser scattering as shown in Figure 5-2. This effect is related to the fact that particle sticking and cylinder wear progressively increases during the experiments, and the related effects cannot be corrected for by background subtraction.

As expected, the in-cylinder temperature increases during compression and decreases during expansion stroke. A comparison to the predicted in-cylinder temperature obtained from 0D simulation will be presented in section 5.7.

While the horizontal temperature profile is flat across the cylinder in the first and in the last part of the compression and expansion stroke, a gradient is progressively appearing when approaching TDC (at 320 and 330°C<sub>A</sub>). The horizontal temperature profiles show higher gradients both in the center and towards the cylinder walls. These temperature stratification is probably the consequence the increase of gas-wall heat transfer when approaching TDC, due to the higher temperature of the in-cylinder gases. Also, these gradients can be related to the increased uncertainty of the technique at these conditions. Indeed, the luminescence signal decreases with increasing temperature reducing significantly the signal to background ratio on both the cameras, inducing higher uncertainty on the temperature evaluation. This statement seems contradictory to the analysis of the measurement uncertainty due the calibration performed earlier in the manuscript, the latter being lower at higher temperature. This is due to the fact that various sources of error participate to the global measurement uncertainty of the temperature, and in the present case they appear to compete between each other. These measurement uncertainty issues will be discussed in more details later in section 0.

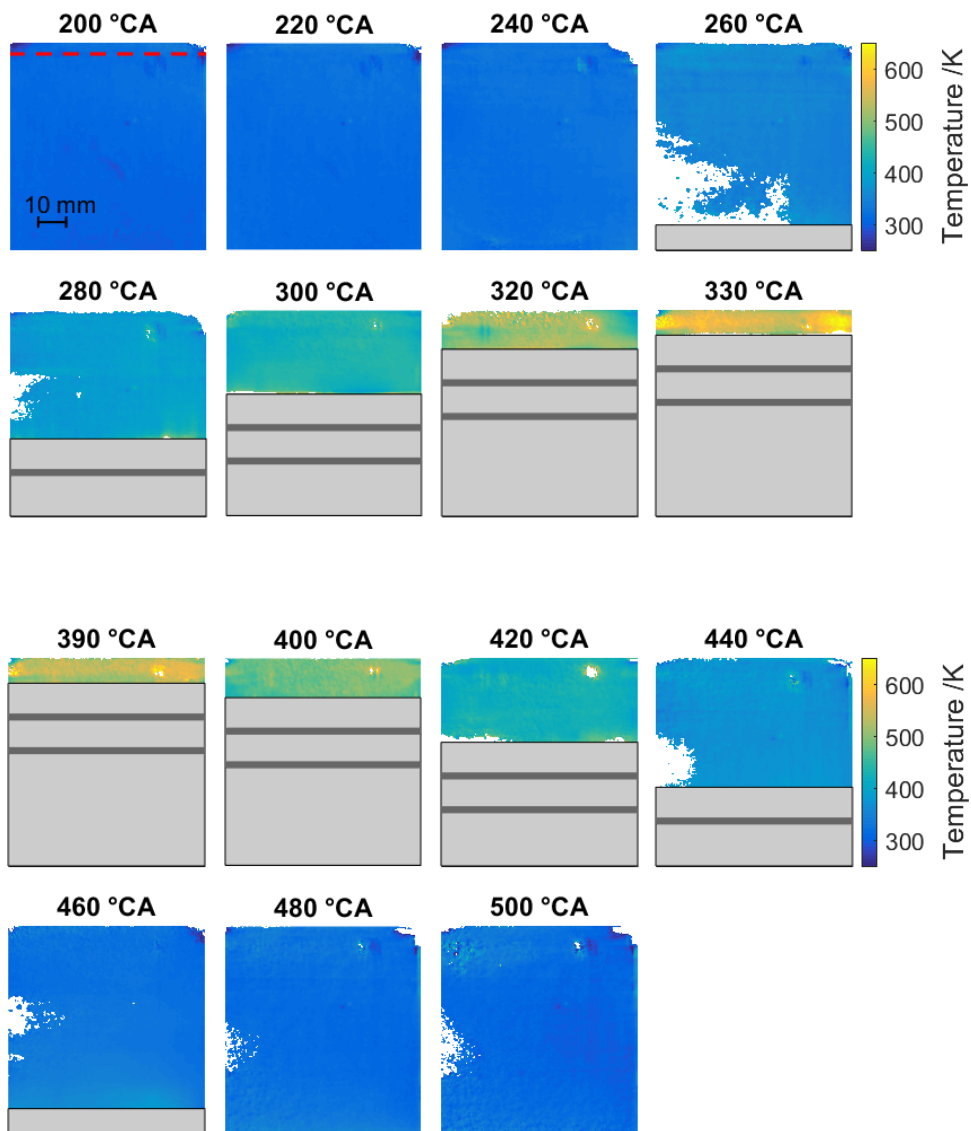


Figure 5-11: In-cylinder time-averaged temperature images taken in motored operation at the reference condition at various crank angles during compression and expansion. The piston is shown in grey. It blocks the optical access between 330 and 390°CA.

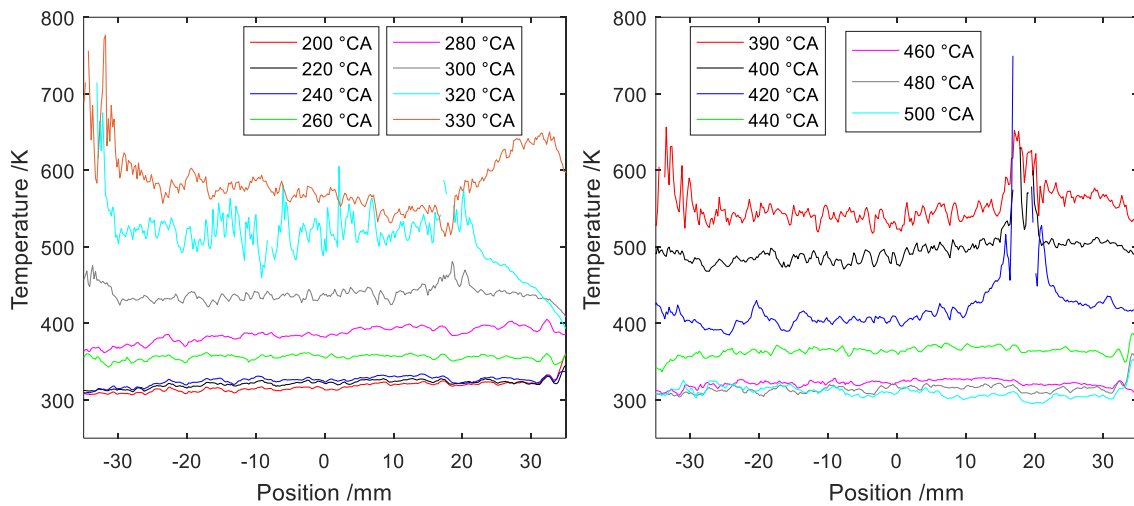


Figure 5-12: Horizontal temperature profiles for the reference condition during the compression and expansion. The temperature profiles are extracted from the time-averaged temperature images from Figure 5-11.

Single-shot temperature images are presented in Figure 5-13. As for the time-averaged images, also the single-shot images show an increase of the temperature as the piston approaches TDC. Compared to time-averaged images, similar homogeneity of the temperature field is observed. Small inhomogeneities are observed near TDC (at 400 and 420 °CA) that are not visible in the corresponding time-averaged images. This aspect can potentially be attributed to the stronger cycle-to-cycle variation of the temperature field. Also, at these temperatures, due to the signal thermal quenching the images are characterized by a lower signal-to-noise ratio. While for the ensemble averaged temperature maps the stochastic noise is canceled, single-shot temperature maps are affected by lower temperature precision. In single-shot temperature maps, temperature variation corresponding to the particles distribution can be observed. This aspect is considered an artifact of the measurement technique related to a not perfect spatial mapping between the images from the two cameras. One solution to reduce the sensitivity to the image alignment is to perform measurements with the cameras slightly out of focus. In this way, blurry images minimize the non-perfect alignment of the two images. This method could be a solution for future engine measurements.

In general, it can be concluded that the technique provides reliable results also in single-shot measurements, even though the results are more sensitive to particle distribution and image alignment.

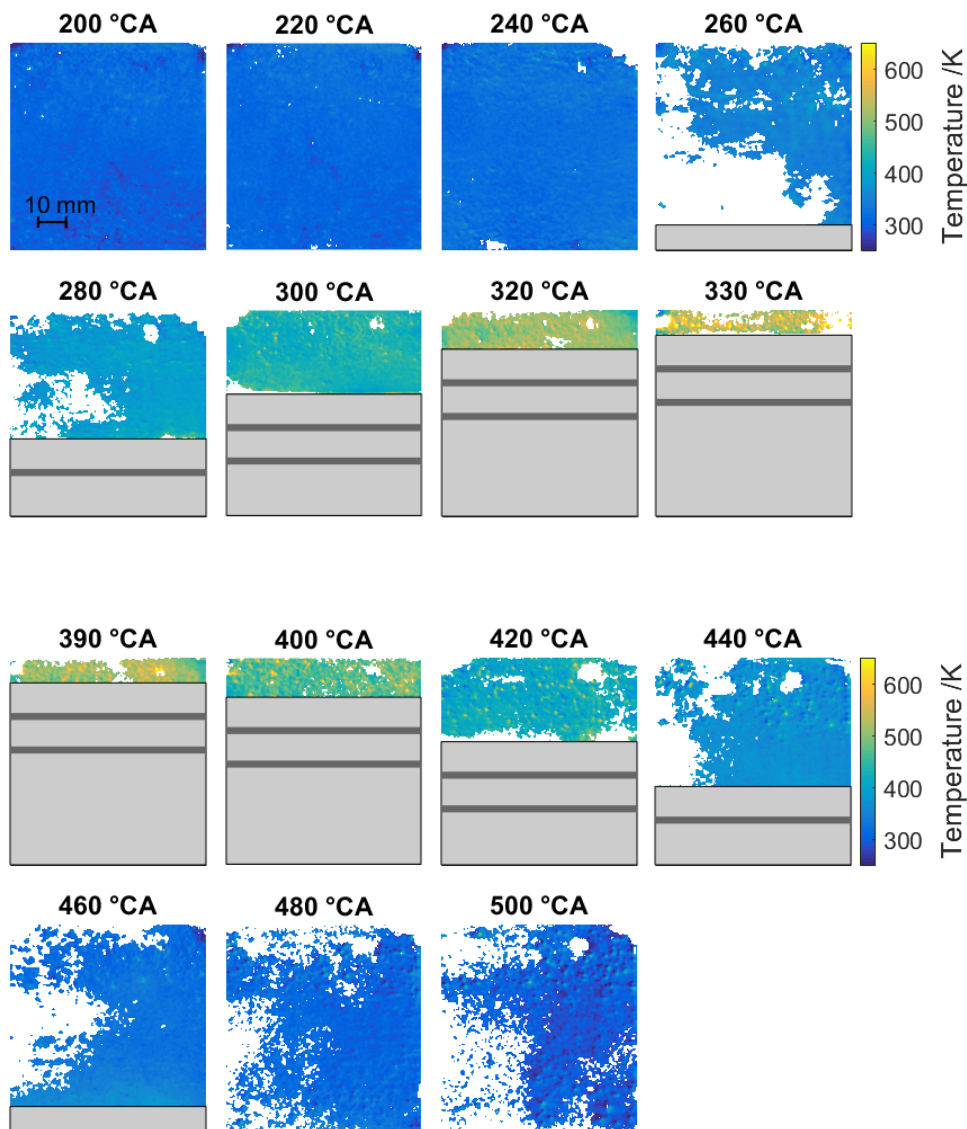


Figure 5-13: In-cylinder single-shot temperature images taken in motored operation at the reference condition at various crank angles during compression and expansion.

### 5.6.2 Increased intake temperature condition

Figure 5-14 shows time-averaged temperature images obtained at increased intake temperature. They show an almost uniform in-cylinder temperature distribution similar to the previous test case. Consistent with the increase of the intake temperature at BDC, the time-averaged temperature measured is increased of approximately 35 K. This aspect of particular importance because the flat-field employed in this case was the same employed for the reference temperature case.

As for the reference test case, some systematic gradients are observed close to the TDC. Near TDC, compared to the reference test case, a higher temperature is observed in the center of the cylinder compared to the regions close to the cylinder walls, as presented in Figure 5-15. At 330°CA, a strong temperature gradient in the order of 200 K from the cylinder axis to the cylinder wall is shown in Figure

5-15. It is difficult to understand how much of this gradient corresponds to real gas temperature variations, as discussed in the previous section it is probably caused by artifacts of the measurement technique. Some of this could be attributed to particle aggregation at the engine walls affecting the accuracy of the measurements. The emission from these particles increases during subsequent measurements and therefore their contribution to the signal is not entirely corrected with the constant background image. An example of particle deposition on the piston surface affecting the temperature field is visible at 240 and 260°CA.

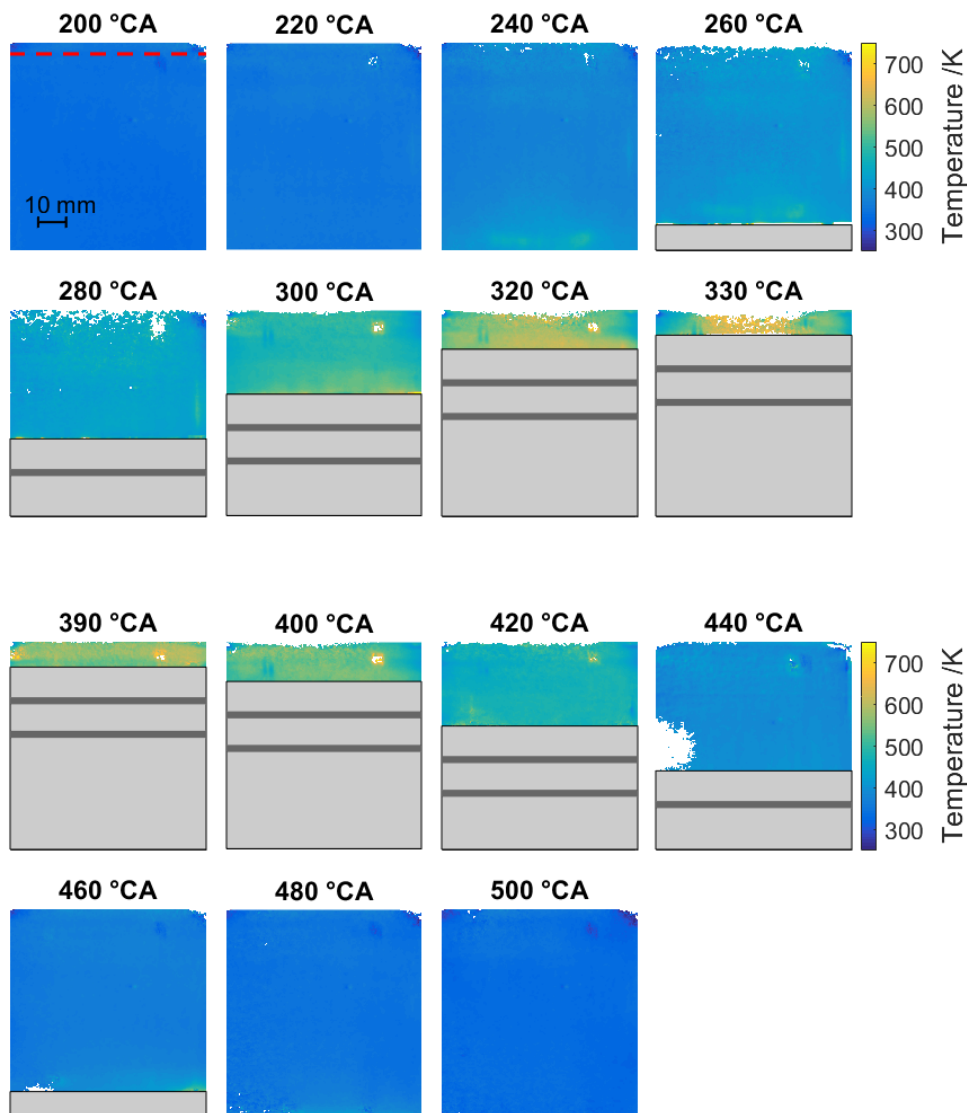


Figure 5-14: In-cylinder time-averaged temperature images taken in motored operation with increased intake temperature at various crank angles during compression and expansion.

Single-shot temperature images for the increased intake temperature condition are presented in Figure 5-16. As for the time-averaged images, also the single-shot images show an increase of the in-cylinder temperature as the piston approached TDC. The quality of some single-shot temperature images is also affected by the low particle density in some regions. Further development on the particle seeding system

is required to improve the way how particles are seeded into engine. A more homogeneous and constant particles seeding would improve the quality of single-shot and average temperature images.

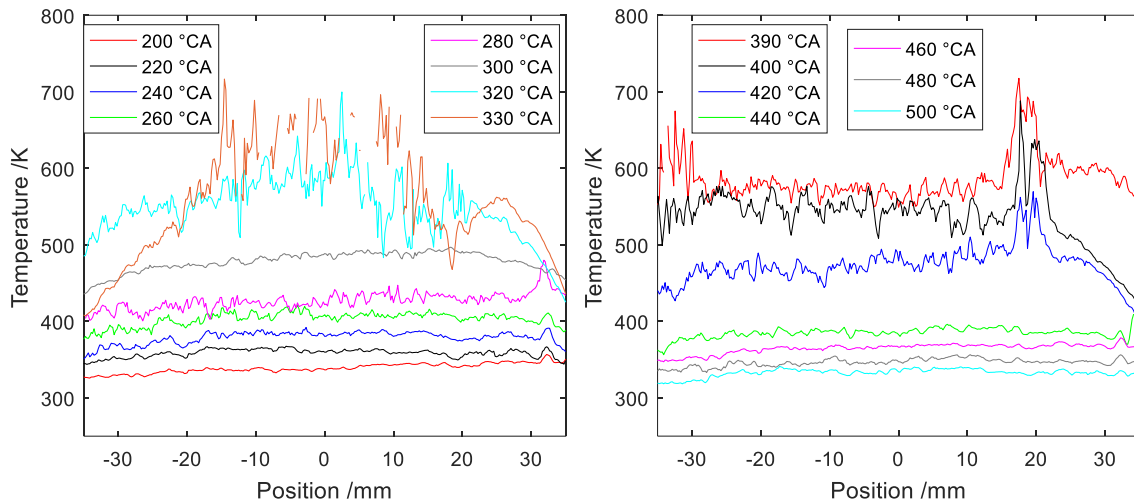


Figure 5-15: Horizontal temperature profiles for increased intake temperature condition during compression and expansion. The temperature profiles are extracted from the time-averaged temperature images of Figure 5-14.

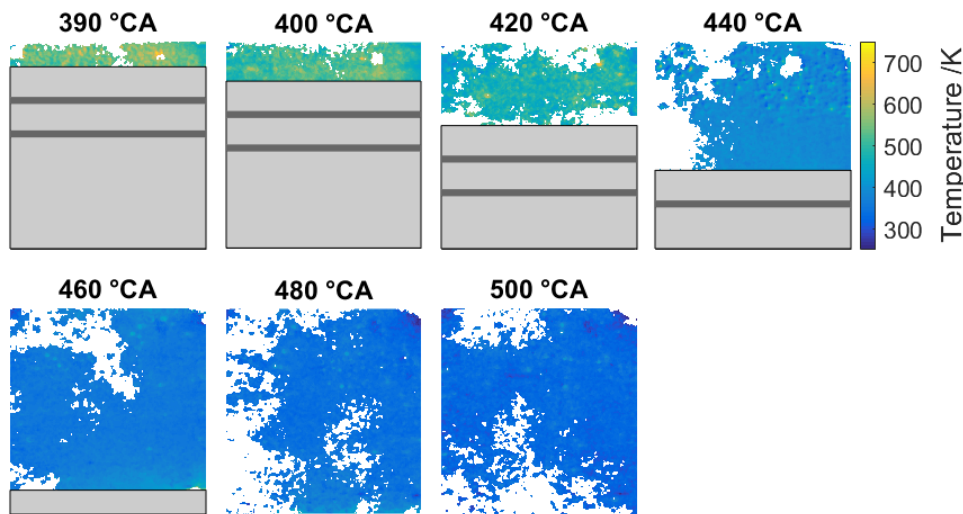


Figure 5-16: In-cylinder single-shot temperature images taken in motored operation with increased intake temperature at various crank angles during compression and expansion.

### 5.6.3 Temperature and velocity fields at the reference condition

Simultaneous in-cylinder time-averaged temperature and velocity fields are presented in Figure 5-17 putting in place the T-PIV diagnostics. These measurements were performed from 180 to 520°CA with an interval of 40°CA. Note that the temperature image obtained at 180°CA is completely uniform due to the fact that the image itself is used as a reference image: all the images, including this one are divided by the reference image which is used as a particular case of flat field (see section 5.3). Also in this case, strange features appear on the temperature images, very probably corresponding to interference from time-varying background signal.

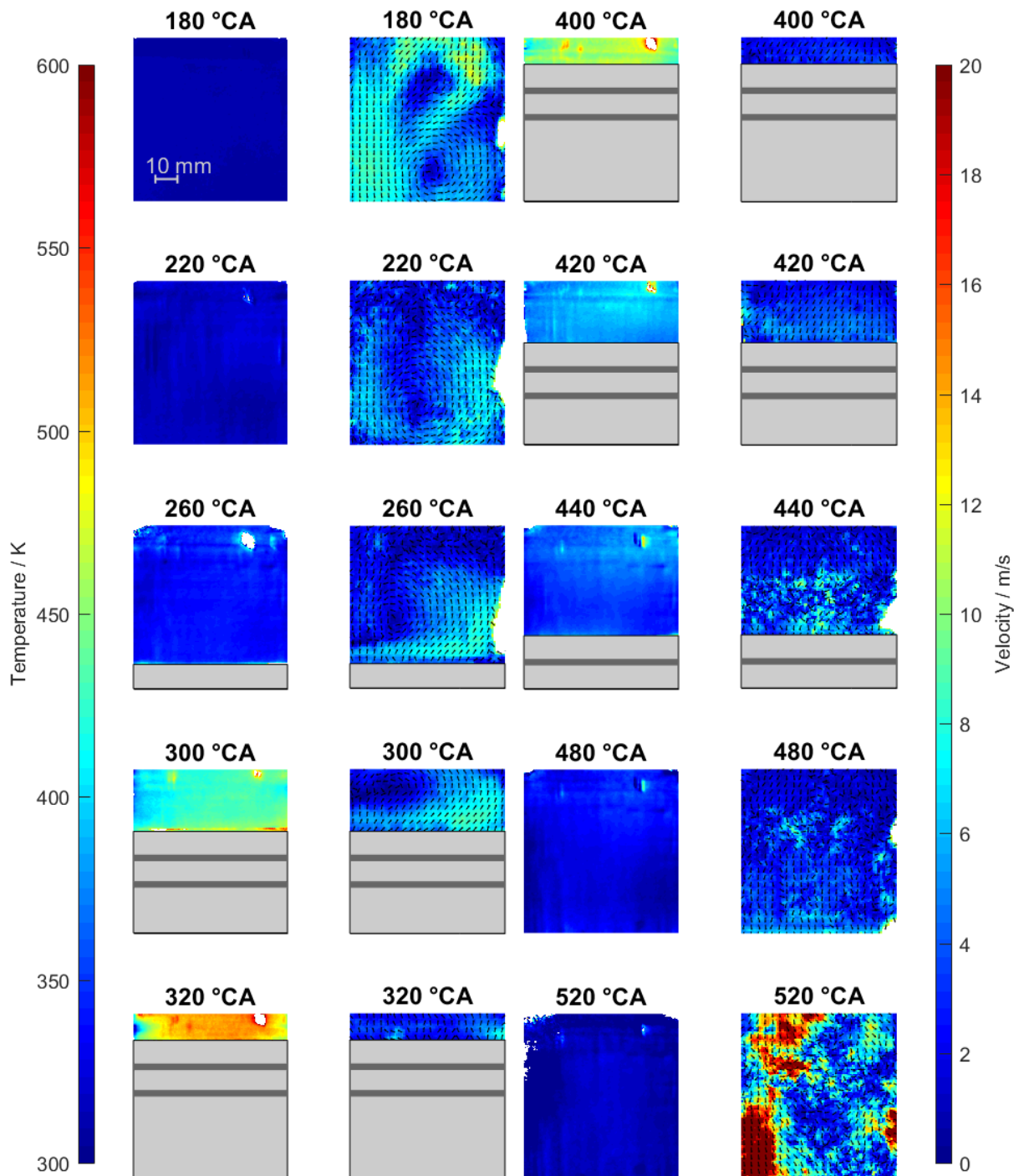


Figure 5-17: In-cylinder time-averaged temperature and velocity images taken in motored operation at the reference conditions at various crank angles during compression and expansion.

The temperatures measured are consistent with the results obtained previously. Even though this result is expected, since the thermography setup has not been changed, these experiments have been performed at different times of the test campaign and their consistency proved the robustness and the repeatability of the diagnostics.

---

The time-averaged velocity fields in Figure 5-17 show a coherent structure that is rotating around a horizontal axis moving across the cylinder bore. As expected, the four-valve pent-roof cylinder head combined with the specially designed intake runners generates a strong tumble flow. The tumble flow motion is visible during the all compression stroke until TDC is reached. After TDC, the tumble motion disappears since it breaks up into small turbulent structures, as a consequence of the reduction of available space. High turbulence levels near TDC are one of the most important parameters in SI engine development in order to improve combustion speed and thermal efficiency. At 520°C, the exhaust valve is open and a reversed flow from the exhaust to the cylinder is visible. Under motored conditions, the in-cylinder gas pressure drops below 1 bar at the end of the expansion stroke due to thermal losses during the compression; this pressure difference promotes a reverse flow at early exhaust valve lift.

#### 5.6.4 Temperature and velocity fields with increased tumble

The measured time-averaged temperature and velocity images for engine operation with increased tumble are presented in Figure 5-18. The temperature images show a uniform temperature distribution almost similar to the reference test case in Figure 5-17. A comparison between both test cases (reference and increased tumble), is presented in the following section, where the spatially-averaged bulk temperatures are compared to the results obtained with 0D simulation.

The velocity fields obtained from reference and increased tumble cases presented in Figure 5-19 and Figure 5-20, as expected, show differences on the tumble flow structure. In general, the tumble adapter should provide higher gas velocity during the intake stroke increasing the tumble flow motion; this is confirmed by the measurements. Also, the resulting tumble motion center has changed compared to the reference test case, as shown when comparing the cross point position on the dashed lines in Figure 5-19, Figure 5-20 and Figure 5-18. To compare the obtained tumble motion with the reference case, some velocity profiles are presented in Figure 5-21. The graphs show the y-component of the velocity vectors measured along the dashed lines indicated in Figure 5-19 and Figure 5-20. The y-coordinate of the dashed lines was chosen to intercept the approximate center of the tumble motion where the y-component of the velocity is the maximum. For the increased tumble case the velocity profile changes with a slightly increase in intensity depending on the horizontal position. However, the in-cylinder flow motion is more complex to be analyzed in 2D maps, therefore the estimation of the tumble motion is straight forward using simple 2D PIV diagnostics. Further measurements would be needed to well understand the way how the tumble adapter impacts the in-cylinder flow motion. However, this measurement would be out of the main scope of this thesis. This parametric variation, demonstrated the sensitivity of the technique to a flow modification.

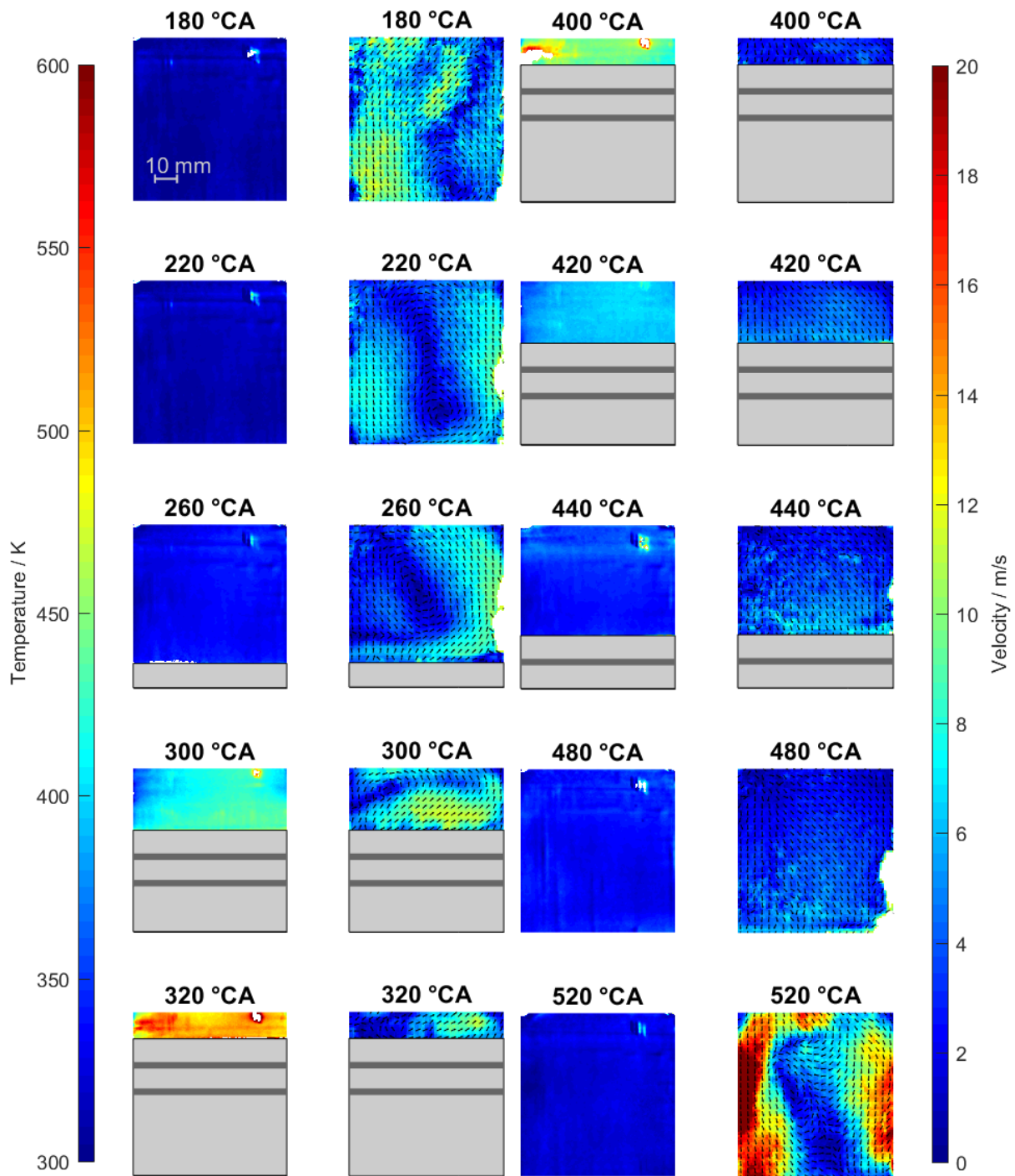


Figure 5-18: In-cylinder time-averaged temperature and velocity images taken in motored operation with increased tumble at various crank angles during compression and expansion.

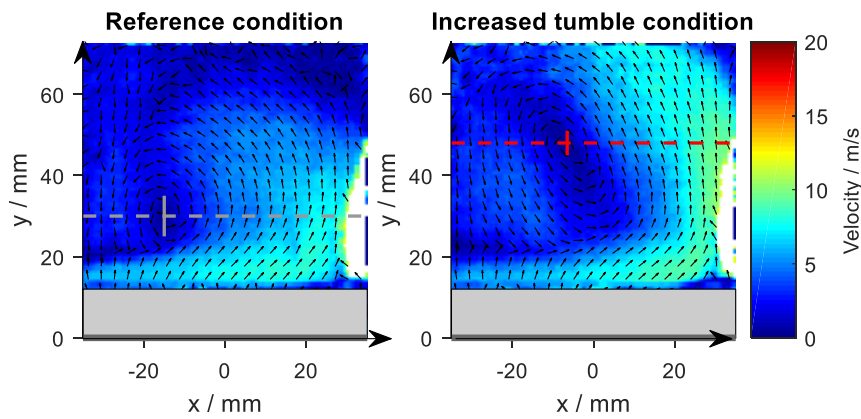


Figure 5-19: Comparison between PIV measurements performed at 260°C for the reference case (left) and increased tumble case (right). The dashed lines in the images shows the horizontal position used to extract the velocity profiles plotted in Figure 5-21.

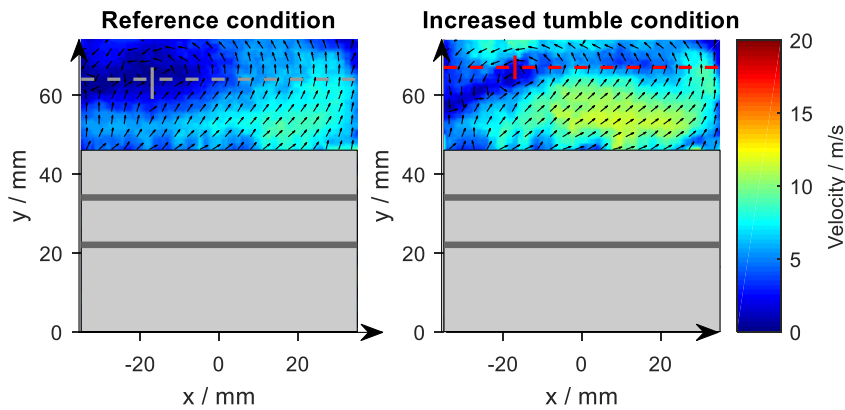


Figure 5-20: Comparison between PIV measurements performed at 300°C for the reference case (left) and increased tumble case (right). The dashed lines in the images shows the horizontal position used to extract the velocity profiles plotted in Figure 5-21.

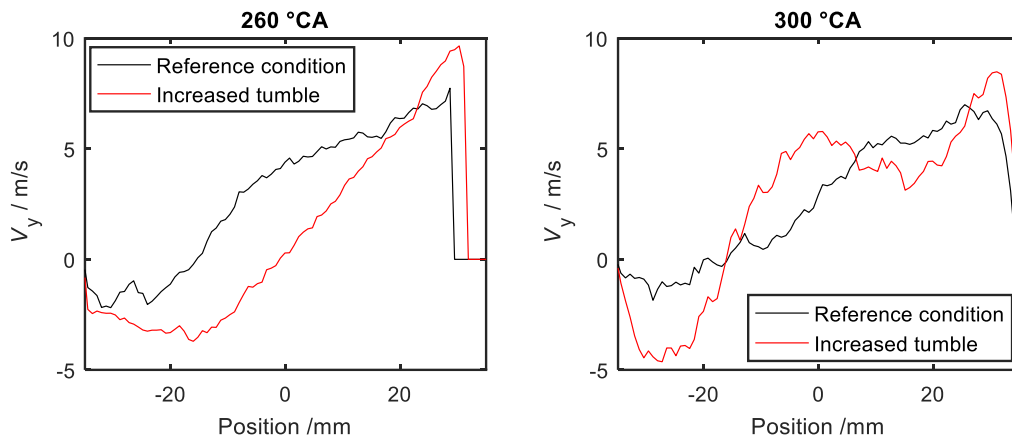


Figure 5-21: Horizontal velocity profiles obtained by PIV measurements at 260°C (left) and 300°C (right). The  $y$ -component of the velocity related to the coordinate positions crossing the horizontal tumble axis (cf. the dashed lines in Figure 5-19 and Figure 5-20) is plotted. In black is indicated the reference case and in red the results obtained in increased tumble case.

---

## 5.7 0D simulation of in-cylinder temperatures

### 5.7.1 Model description

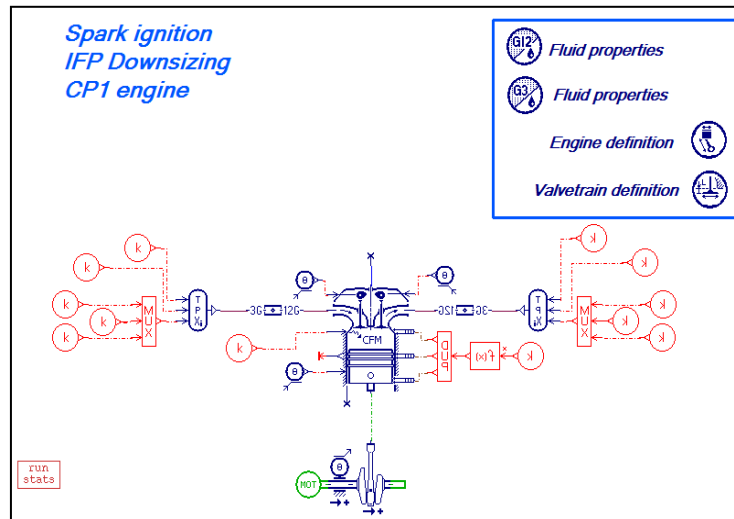


Figure 5-22: Simcenter Amesim sketch of the single-cylinder SI optical engine used in this work [92].

The accuracy of the phosphor thermometry measurements is evaluated by comparison with the results of simulations based on a 0D model-based software (Simcenter Amesim). In motored operation, the in-cylinder temperature distribution is expected to be homogeneous except for the zones near the cylinder walls where heat transfer is not negligible. Under these conditions, the in-cylinder bulk temperature can be calculated with good accuracy with a 0D model-based simulation. Without combustion, the temperature variation during the engine cycle is based on the thermodynamic calculation following the perfect gas law and the energy balance at the boundaries. The heat exchange at the wall was taken into account by the Woschni correlation [93]. More details about the simulation can be found in the papers of Lafossas et al. [94] and Richard et al. [95].

In this work, the commercially available single-cylinder component (taken from the existing program library) was used to simulate the in-cylinder temperature evolution during the engine cycle. The characteristics of the optical engine, e.g., geometry, valve lift, and valve timing were integrated in a single-cylinder SI engine sketch, presented in Figure 5-22. Before running the model, a series of boundary conditions were set up:

- **Intake conditions:** Intake conditions are provided from intake pressures and temperatures recorded during the engine measurements by thermocouples and pressure sensors at the intake and exhaust manifolds. Intake temperature and pressure traces averaged over 200 engine cycles are presented in Figure 5-23.

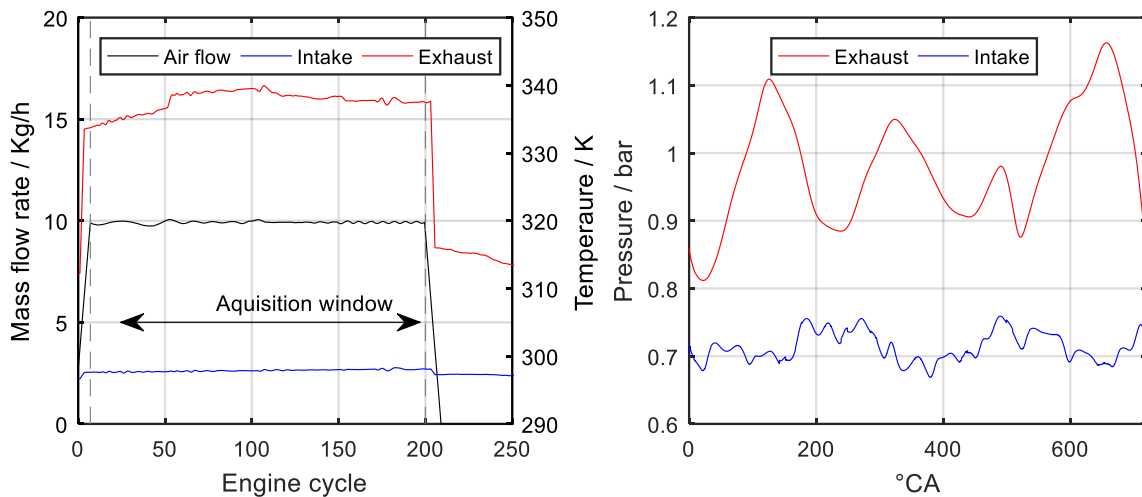


Figure 5-23: Boundary conditions used for the simulation model. Left: Measured intake and exhaust temperature together with the intake mass flow rate. Right: Measured intake and exhaust pressure traces. The values shown in the graphs are averaged over 200 engine cycles.

- **Exhaust conditions:** The exhaust boundary conditions were determined from the measured pressure and temperature traces at the exhaust manifold averaged over 200 engine cycles shown in Figure 5-23.
- **Gas composition:** Dried air was considered for the in-cylinder gas composition, since experiments were performed in motored conditions without fuel injection.
- **In-cylinder wall temperature:** The in-cylinder wall temperature was determined by phosphor thermometry. The internal surface of the quartz cylinder was coated with a thin layer (5–7  $\mu\text{m}$ ) of ZnO:Zn. It was excited with the third harmonic (355 nm) of a Nd:YAG laser and the phosphorescence was detected by a photomultiplier with 1 MHz bandwidth. A bandpass filter (505 $\pm$ 10 nm) was placed in front of the photomultiplier to discriminate the temperature-dependent phosphorescence emission at 510 nm (emission peak used for lifetime-based thermometry, cf. Figure 3-10) against scattered laser light. The phosphorescence lifetime was recorded and converted to temperature using the appropriate calibration curve (lifetime vs. temperature). The experimental setup is shown in Figure 5-24. For more details about the apparatus and the calibration, see Refs. [96,97]. The measurements were performed at various crank angles over 500 engine cycles under motored conditions. The results show that the in-cylinder wall temperature is approximately constant during the engine cycle. The measurements reveal an in-cylinder wall temperature of 84°C with an associated standard deviation of 5°C. This temperature was included in the model to account for heat transfer.

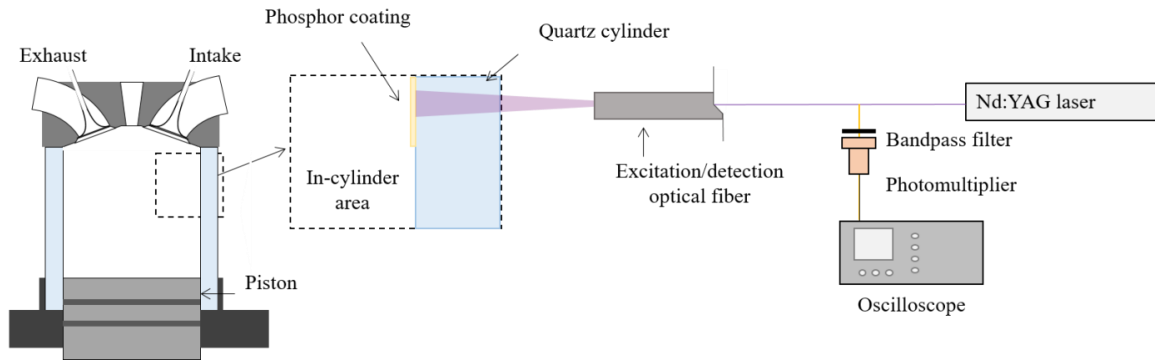


Figure 5-24: Experimental arrangement for the measurement of the in-cylinder wall temperature in the motored engine via phosphor thermometry.

Once boundary conditions were defined, some of the model parameters were adjusted to provide the best match with the measurements. Especially, the heat-transfer coefficients used in the Woschni correlation were adjusted to have the best match between experimental and model in cylinder pressure curve. The result of this fitting is presented on the left hand side of Figure 5-25. Good agreement was thus reached between the simulated in-cylinder pressure trace and the measured one. The corresponding calculated in-cylinder temperature for 298 K intake temperature, is presented in Figure 5-25 (right). Note that the local minimum of the temperature at the end of the expansion stroke (after exhaust valve opening) is probably not correctly predicted by the model. Between 480 and 520°CA, flow reversal occurs at exhaust valve opening due to the lower in-cylinder pressure compared to the pressure in the exhaust manifold. Under these conditions, heat exchange could be overestimated and not well taken into account, resulting in erroneous simulations of the in-cylinder gas temperatures.

This model was used to evaluate the in-cylinder temperature for the reference case ( $T_{\text{intake}} = 298 \text{ K}$ ) as well as for the case with increased intake temperature ( $T_{\text{intake}} = 333 \text{ K}$ ). Initializing the model with different tumble levels resulted in the same in-cylinder temperature curve. In this model, the tumble only affects the combustion analysis which is deactivated for motored engine operation. Therefore, the in-cylinder temperature curve obtained for the reference condition was also used to compare the measurements obtained with increased tumble level.

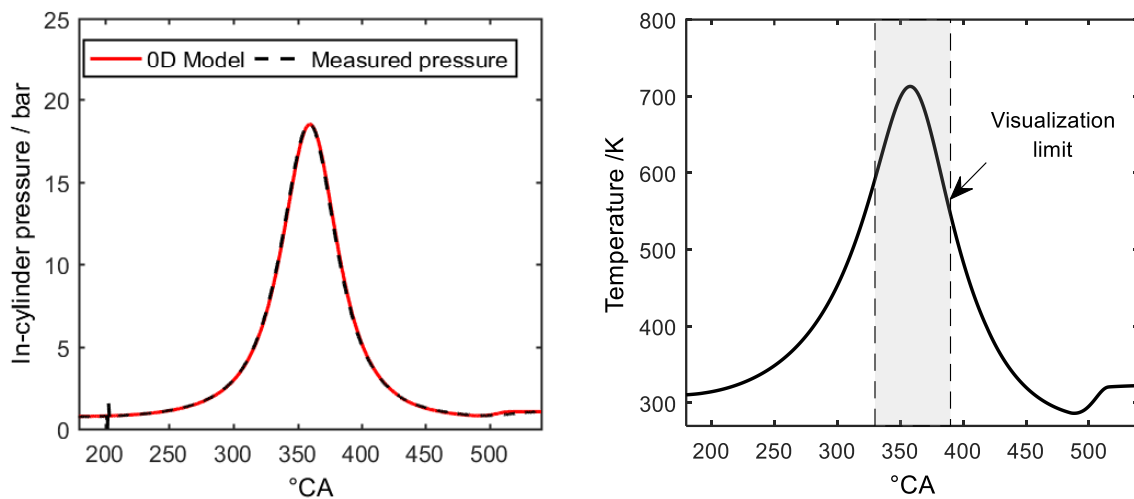


Figure 5-25: In-cylinder pressure and temperature traces obtained from the adjusted 0D simulation. Left: Comparison of the measured in-cylinder pressure with 0D model resulting pressure trace. Right: 0D simulated in-cylinder temperature trace. The grey area marks the zone that cannot be visualized in the engine because the piston blocks the optical access.

### 5.7.2 Comparison of results: 0D simulation vs. measurements

The measured in-cylinder bulk gas temperature is compared with the in-cylinder temperature trace obtained with 0D model-based simulation presented in the previous section. For the reference condition test case, the comparison is presented in Figure 5-26. For the measurements, the bulk gas temperature is calculated by averaging the temperature in the  $62 \times 5 \text{ mm}^2$  region (shown in Figure 5-9) in the time-averaged in-cylinder temperature images.

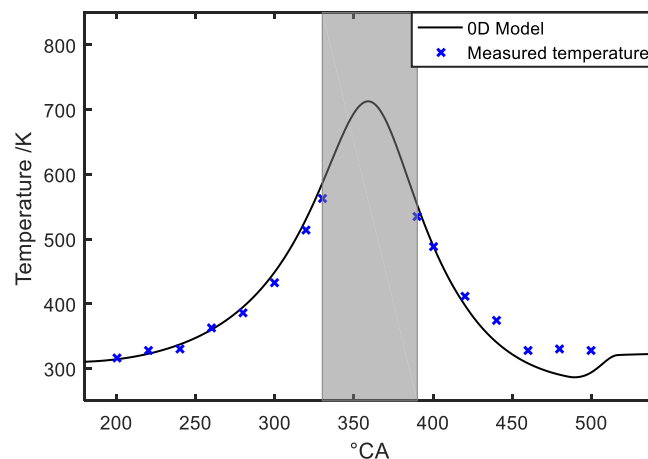


Figure 5-26: Spatially-averaged in-cylinder temperature obtained with phosphor thermometry at intake reference condition ( $T = 298 \text{ K}$ ). The grey region shows the crank angle degrees that are not optically accessible. The experimental results (blue symbols) are compared with the simulation (line).

The measured bulk-gas temperature shows a reasonably good agreement with the predicted in-cylinder temperature as shown in Figure 5-26. The trend shown by the measured data follows the evolution of

the in-cylinder temperature predicted by the 0D simulation. A small deviation from the predicted temperatures is observed at the end of the expansion stroke, between 480 and 500°CA. As discussed before, in this crank-angle range, the model prediction is affected by the uncertainty caused by the reversed flow. In this case, the measured results agree better with the expected trend of the in-cylinder temperature following quite monotonic decrease.

The measured temperatures together with the predicted temperatures are presented in Table 5-4. From 200 to 420°CA, the measurements show a maximum deviation from the model of around 5%. A much higher deviation of 14% is observed at 480°CA, where the simulation probably underestimates the in-cylinder temperature.

Table 5-4: Comparison between measured spatially-averaged in-cylinder temperature and simulated temperature for the reference test case at 298 K intake temperature.

Timing / °CA	T: measured / K	T: 0D simulation / K	$\Delta$ (%)	Timing / °CA	T: measured / K	T: 0D simulation / K	$\Delta$ (%)
200	317	314	1.0	400	487	490	0.6
220	327	322	1.6	420	412	398	3.5
240	330	337	2.1	440	373	341	9.4
260	341	360	5.3	460	327	308	6.2
280	385	395	2.5	480	331	290	14.1
300	432	449	3.8	500	329	294	11.9
320	515	532	3.2				
330	563	586	3.9				
390	535	552	3.1				

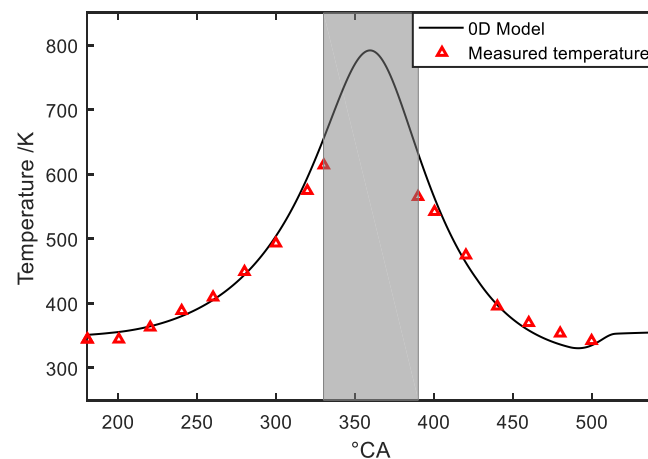


Figure 5-27: Spatially-averaged in-cylinder temperature obtained with phosphor thermometry at increased intake temperature condition ( $T = 333$  K). The measurements (red symbols) are compared with the simulation (line).

Figure 5-27 shows the results for the increased intake temperature condition test case. The measurements capture well the absolute difference in temperature between the reference condition and the increased

intake temperature condition. It is important to remark that while a flat-field correction was used to normalize the temperature at 200°CA in the reference condition, the same flat-field is used for the temperature estimation for the increased intake temperature case. Therefore, the fact that the temperature difference between the two test cases is well captured by the measurements is a further prove of the good accuracy of the diagnostic. The absolute values of the measured in-cylinder temperatures are in good agreement with the predicted temperatures from 0D simulation. Significant temperature differences in the order of 6–10% are observed for crank angles near TDC (330 and 390°CA) as shown in Table 5-5. At these crank angles, the measured time-averaged temperature (shown in Figure 5-14), is much more affected by the inhomogeneity distribution of the in-cylinder temperature.

Table 5-5: Comparison of measured and simulated temperature for the 333 K intake temperature reference case.

<b>Tim- ing / °CA</b>	<b>T: measured / K</b>	<b>T: 0D simulation / K</b>	<b>Δ (%)</b>	<b>Timing / °CA</b>	<b>T: measured / K</b>	<b>T: 0D simulation / K</b>	<b>Δ (%)</b>
180	342	351	2.6	390	566	631	10.3
200	343	355	3.4	400	543	565	3.9
220	362	364	0.5	420	474	464	2.2
240	388	380	2.1	440	395	398	0.8
260	409	405	1.0	460	370	358	3.4
280	448	444	0.9	480	352	336	4.8
300	493	505	2.4	500	343	335	2.4
320	575	596	3.5				
330	614	655	6.3				

Figure 5-28 shows a comparison of the in-cylinder temperatures measured at different tumble conditions and the 0D simulation. The measured temperatures suggest that there is not a significant impact on in-cylinder temperatures with increasing the tumble level. However, a small decrease in temperature is observed during the compression stroke from 300 to 330°CA where the increased rotating flows are expected to enhance the wall heat transfer. The same decrease in temperature is also visible during the expansion stroke, with a maximum temperature difference of 32 K (480°CA) compared to the reference test case, as shown in Table 5-6. After TDC, the entire tumble broke up into micro-scale turbulence improving the wall heat transfer. Even though it is not possible to verify the measured temperature difference, the fact that results are coherent with first order estimations (the stronger tumble motion causes higher heat losses and lower temperatures), is a further indication of the reliability of the technique.

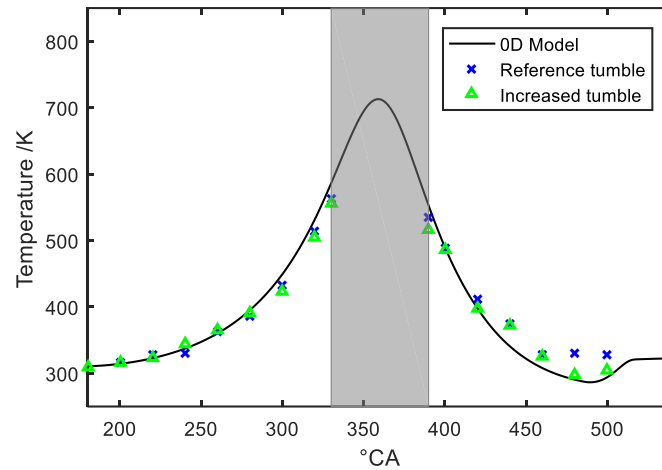


Figure 5-28: Spatially-averaged in-cylinder temperature obtained with phosphor thermometry at reference and increased tumble conditions.

Table 5-6: Comparison of measured and simulated in-cylinder temperatures for reference and increased tumble.

Timing / °CA	<i>T</i> : ref. tumble / K	<i>T</i> : increased tumble / K	Timing / °CA	<i>T</i> : ref. tumble / K	<i>T</i> : increased tumble / K
200	317	315	400	487	485
220	327	323	420	412	397
240	330	344	440	373	371
260	341	364	460	327	324
280	385	391	480	331	299
300	432	423	500	329	304
320	515	504			
330	563	554			
390	535	516			

## 5.8 Measurement uncertainty

The measurement of the temperature by thermographic PIV involves different steps, from experimental to post-processing ones, each affected by error sources. The experimental procedure and the post-processing methodology aim at minimizing these error sources, but a certain level of error is unavoidable. Assessing the effect of these error sources is important to evaluate the ability of the measurement technique to capture the physical processes. It is for instance interesting to evaluate if the measurement technique is accurate enough to capture the effect of parametric variations on the in-cylinder gases tem-

---

perature (effect of tumble intensity for instance), or if measured temperature stratification is the consequence of a physical process (for example heat transfer processes during the compression stroke) or of a low measurement precision (for example due to a low signal to background ratio).

Among the numerous sources of error that exist in the measurement we can cite: light collected by the camera system that does not come from the fluorescence of the phosphor particles illuminated by the laser sheet, non-uniformity and non-linearity of the camera sensor, camera shot noise, image registration errors, calibration error... All these error sources are taken into account in the post processing: background images are taken before and after acquisition sequences and are subtracted to the raw images, a flat field image is used to correct for non-uniformity of the camera sensor, pixel binning is used to optimize camera linearity, median filtering is used to minimize camera shot noise, a high precision target is used for image registration, and the measurement uncertainty due to calibration has been assessed using the calibration data. However, these corrections are imperfect and error sources remain, affecting the accuracy (systematic error) and the precision (statistical error) of the measurement.

Taking into account all the corrections implemented, we consider that in the present measurement, systematic errors are mainly affected by the two following error sources: uncertainties associated with the calibration process where the intensity ratio images are converted to temperature images (c.f. section 4.6.2), and a low signal to background ratio at high temperature. The main sources of errors of the calibration are related to the choice of filters as well as the quality of the fitting process as discussed in section 4.6.2. This effect of the calibration on the measurement uncertainty is presented later in this section. To better illustrate the uncertainties related to low signal to background ratio, an investigation of the evolution of this ratio during the compression stroke was performed. The background is the result of different processes, including flare of the phosphorescence signal emitted from particles in the laser sheet and reflected by the chamber walls, as well as phosphor emission from particles sticking on the engine walls and illuminated by reflection of the laser. These background sources may vary in intensity and location during the experiment, so that the background image acquired before and after the acquisition sequence are not able to perfectly correct for this effect. When the signal to background decrease to low levels, the contribution of this error source may become predominant, affecting both the measurement accuracy and precision.

Figure 5-29 illustrates the evolution of the signal, the background and the ratio of both during compression when the temperature in the cylinder increases. The signal intensity is calculated by averaging the signal intensity in  $8 \times 8$  mm<sup>2</sup> region of the time-averaged signal intensity images (over 200 engine cycles). The region of interest was chosen in a zone where the signal was approximately uniform. It is clear in this graph that when temperature increases the signal to background ratio decreases significantly because of the decrease in phosphorescence signal. At high temperature ( $>500\text{K}$ ) the signal to background is close to 1. With such low ratios, it is easy to understand that small error in the determination of the background may result in large measurement errors. However, due to the difficult to quantify precisely the contribution of the background variation to temperature error, such a quantitative analysis could not be performed in the scope of the present work, and further investigations on the variation of the background signal during measurements need to be done in future.

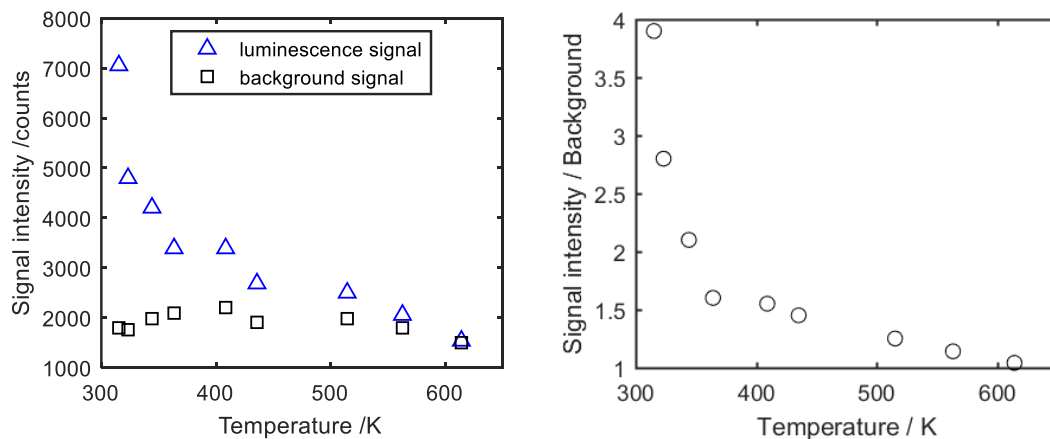


Figure 5-29: Left: Variation of the luminescence signal and background signal as a function of the temperature. Right: Variation of the luminescence to background signal ratio as a function of the temperature. The signal intensity is derived from the average signal on an  $8 \times 8$  mm<sup>2</sup> region of the time-averaged signal intensity images.

Despite of this limitation, the measurement uncertainty was investigated in two ways. First the effect of the calibration on the measurement uncertainty is analyzed in the next section, and an estimation of the measurement precision is presented in the following one.

### 5.8.1 Effect of the calibration on the measurement uncertainty

The measurement uncertainty due to calibration of the spatially-averaged in-cylinder temperatures was determined by taking into account the confidence interval associated to the calibration curve, shown in Figure 4-40. The upper and lower limits of the confidence interval of the calibration curve were used to determine the upper and lower temperatures at the respective crank angle. The difference between the upper and lower temperature was used to estimate the uncertainty of the temperature measurement.

For the test cases studied in this work, the obtained measurement uncertainties are presented in Figure 5-30 and Figure 5-31 in term of error bars plotted together with the spatially-averaged temperatures. The results from the OD simulation are also plotted in the same figures. The measurement uncertainty decreases during the compression stroke and increases during the expansion stroke, as shown in Figure 5-32-left. This is related to the large confidence interval obtained at lower temperatures as shown and discussed in section 4.6 and shown in Figure 4-40. As discussed in section 4.6.2, the choice of filters allows to optimize the measurements for temperatures higher than 400 K. This leads to an improvement on the measurement uncertainty due to calibration at higher temperatures, as shown in Figure 5-32-right.

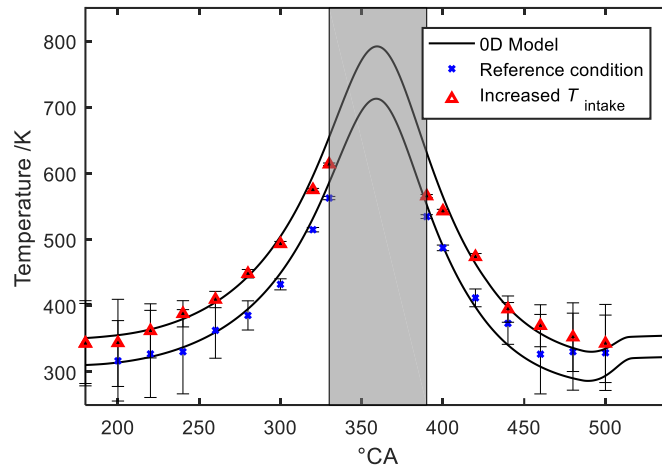


Figure 5-30: Measurement uncertainties of the 200-cycle average plotted in the form of error bars for different intake temperature conditions: Reference and increased intake temperature conditions.

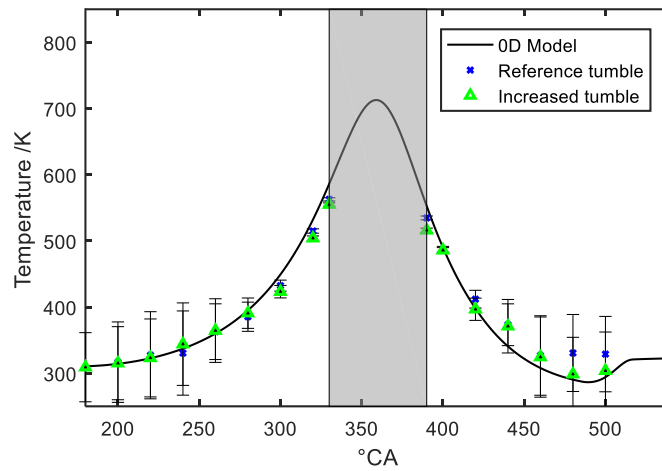


Figure 5-31: Measurement uncertainties of the 200-cycle average plotted in the form of error bars for different intake conditions: Reference and increased tumble conditions.

The measurement uncertainty due to the calibration is found to be 55 K (18%) at 300 K and 2 K (0.3%) at 614 K for the 200-cycle average. This shows a promise for highly accurate temperature measurements at higher temperatures (near TDC) in future experiments. Note that the measurement uncertainty presented here is only due to the calibration. As explained before, at high temperature conditions the measurements are strongly affected by the low signal to background ratio, in such a way that this effect is competing with the lower uncertainty related to the calibration.

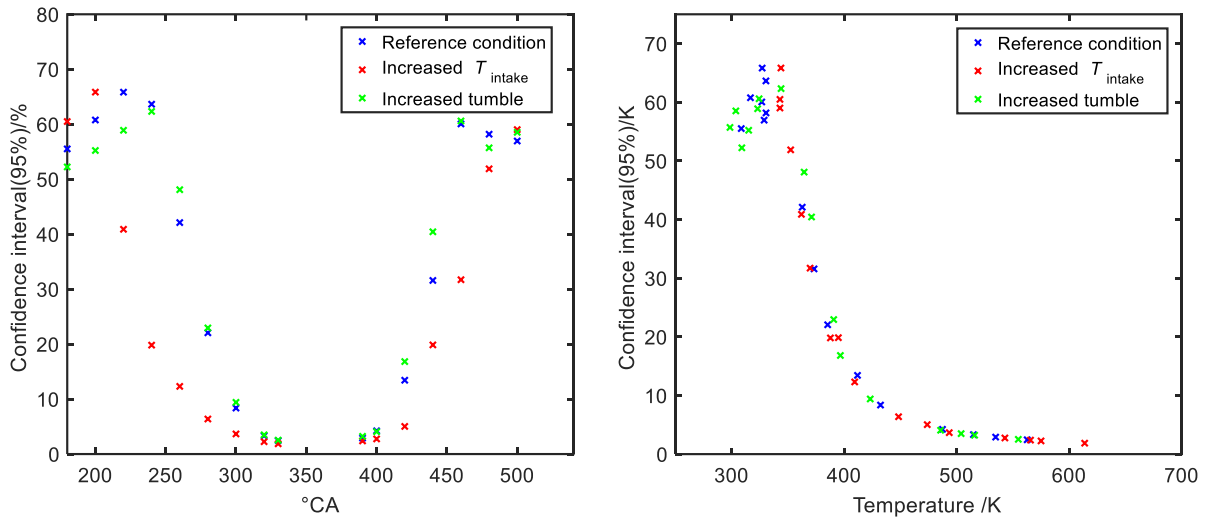


Figure 5-32: Left: Variation of the measurement uncertainty during the compression and expansion strokes for each test case. Right: Measurement uncertainty as a function of the measured temperature for each test case.

### 5.8.2 Measurement precision

Similarly to the analysis of the systematic error, taking into account all the corrections implemented, we consider that in the present measurement statistical errors are mainly affected by low signal to background ratio at high temperature. Indeed, we consider that pixel binning, median filtering, and the use of a high precision target are efficient in minimizing the errors due to camera non-linearity, camera shot noise and image registration respectively. However, Figure 5-32 shows that important errors can be expected at high temperature due to the low signal to background. Unfortunately, it is also at high temperature, late in the compression stroke that fluctuations and stratification of temperature are expected due respectively to cycle to cycle pressure variation, and stratification induced by wall heat transfer during the compression stroke. Therefore, since the quantification of the measurement error due to low signal to background ratio could not be performed in the scope of the present work, a detailed analysis of the temperature stratification and in particular the analysis of the contribution of physical process compared to measurement error is not possible.

Therefore, in this section, the calculation of the temperature precision is based on the hypothesis that the temperature is uniform and the measured cycle-to-cycle temperature fluctuations are only due to the measurement uncertainties. While this hypothesis seems to be valid at BDC where the in-cylinder temperature is quite close to the intake temperature, this is not the case near TDC where the in-cylinder temperature increases together with the wall heat transfer inducing cycle-to-cycle fluctuation on the mean temperature and stratification. To discriminate the effect of the cycle-to-cycle pressure fluctuation in the calculation of the measurement precision, a comparison with the expected temperature variation cycle-to-cycle is made later in this section.

The single-shot precision was determined from 200 single-shot temperature images for each engine timing. Temperature precisions were calculated on a double standard deviation basis in a  $62 \times 5 \text{ mm}^2$  region of interest where the temperature was approximately uniform. These data were used to generate

the histogram of the temperature distributions for each crank angle studied. Figure 5-33 shows histograms of single-shot temperature for the reference condition. The single-shot standard deviation increases when approaching TDC due to the multiple factors already discussed.

For the reference test case, the obtained standard deviation (STD) increases from 3.7 K (1.2% at 317 K) to 17.3 K (3.3% at 515 K), from 200 to 320°CA respectively. For the increased intake temperature condition case, the results are presented in Figure 5-34. From 200 to 320°CA, the STD increases from 2.3 K (0.6% at 343 K) to 24.4 K (4.2% at 575 K), respectively. It is important to note that for the increased intake temperature case, the STD increases compared to the reference case.

For the reference test case, during the expansion stroke, the measured standard deviation is 14.4 K (3% at 487 K), 10.1 K (2.7% at 373 K), 10.4 K (3.1% at 331 K), and 10.8 K (3.2% at 329 K) at 400, 440, 480, and 500°CA respectively. For the increased intake temperature test case, the STD is according to Figure 5-34: 24.4 K (3.7% at 543 K), 10.7 K (2.7% at 395 K), 7.4 K (2.1% at 352 K), and 7.4 K (2.1% at 343 K) at 400, 440, 480, and 500°CA respectively.

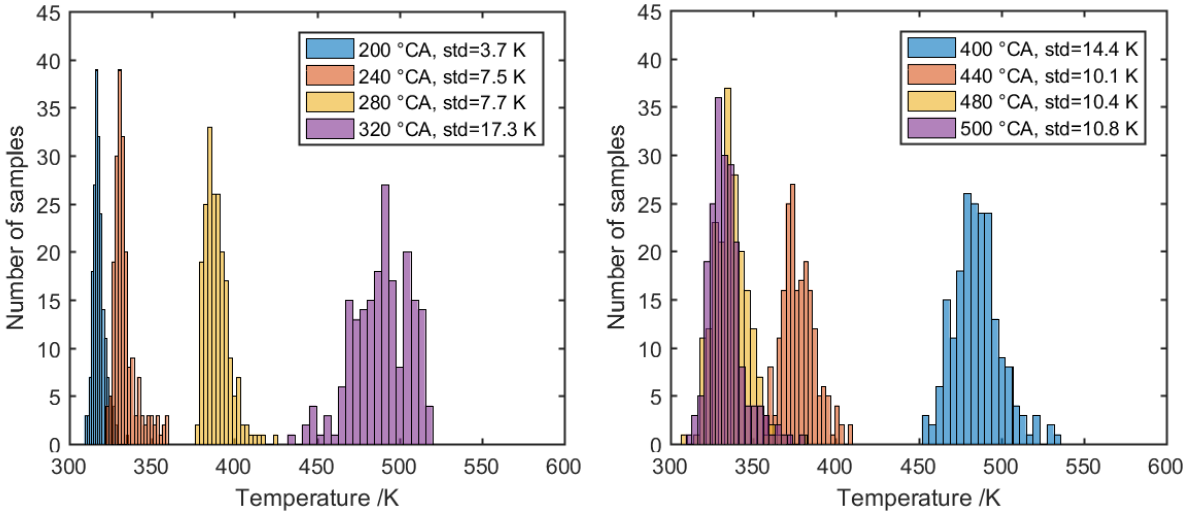


Figure 5-33: Histograms of 200 single-shot temperature measurements recorded at various crank angles for the reference condition. The results are presented during compression (left) and expansion (right). Where std represents the measured standard deviation in temperature derived from a 65×5 mm<sup>2</sup> field.

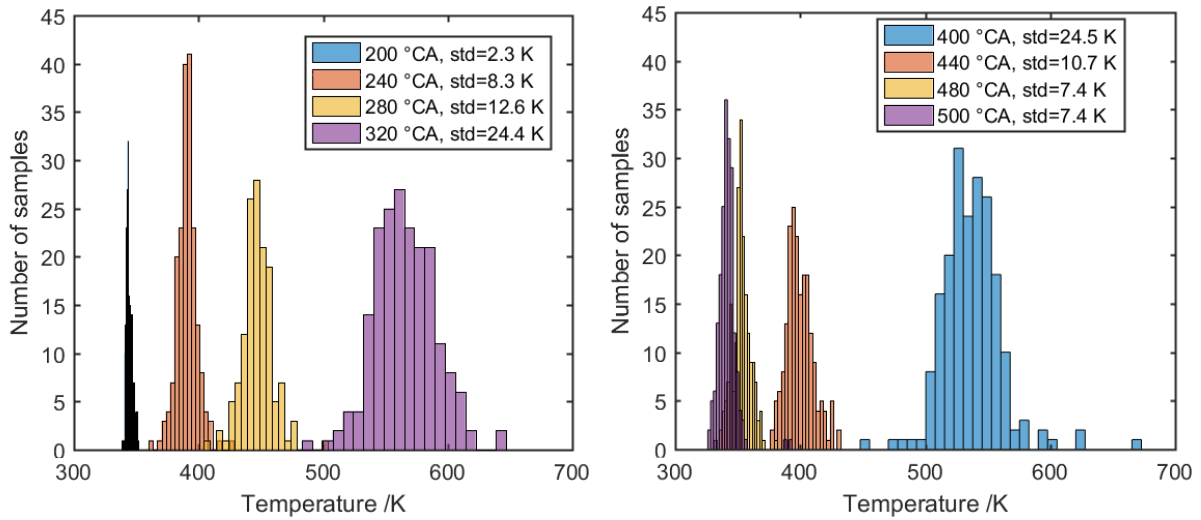


Figure 5-34: Histograms of 200 single-shot temperature measurements, recorded at various crank angles for increased intake temperature. The results are presented during the compression (left) and expansion (right). Where std represents the measured standard deviation in temperature derived from a  $65 \times 5 \text{ mm}^2$  field.

Figure 5-35 shows the single-shot standard deviation obtained for the increased tumble condition. During the compression stroke, the measured STD is 5 K (1.6% at 315 K), 7.3 K (2.1% at 344 K), 4.7 K (1.2% at 391 K), and 12 K (2.4% at 504 K) at 200, 240, 280, and 320°CA respectively. During the expansion stroke, the STD is 10.5 K (2% at 485 K), 10.1 K (2.7% at 371 K), 5.1 K (1.7% at 299 K), and 3.7 K (1.2% at 304 K) at 400, 440, 480, and 500°CA respectively. The single-shot measurements obtained at increased tumble show a slight decrease in the measured temperature dispersion. The single-shot mean temperatures show a less broad temperature distribution compared to the reference test case. These results suggest that with increasing tumble, the in-cylinder temperature fluctuations due to cycle-to-cycle and heat transfer variations decrease.

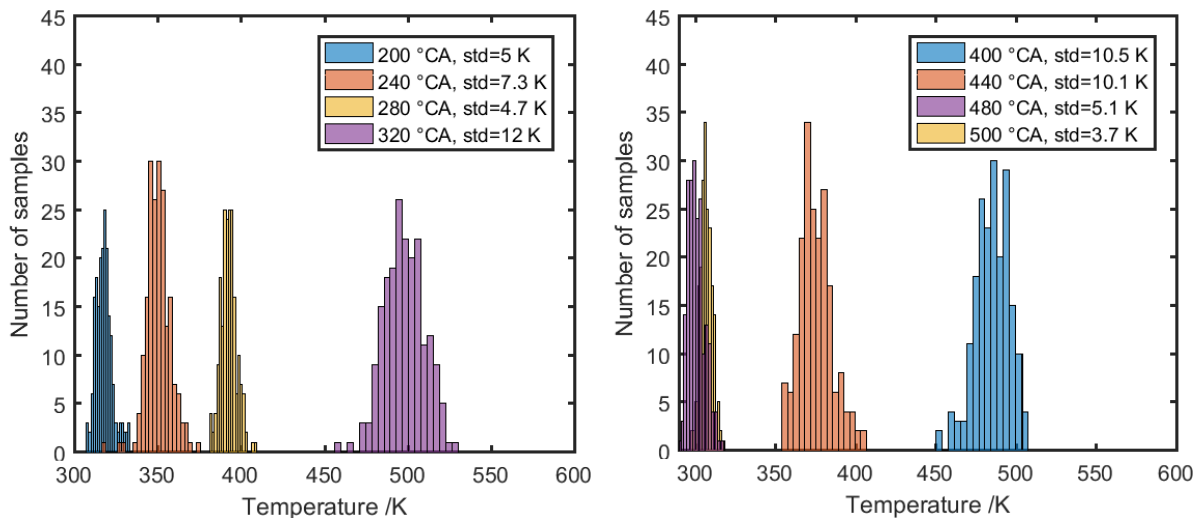


Figure 5-35: Histograms of 200 single-shot temperature measurements, recorded at various engine timings and at increased tumble condition. The results are presented during the compression (left) and expansion (right). Where std represents the measured standard deviation in temperature derived from a  $65 \times 5 \text{ mm}^2$  field.

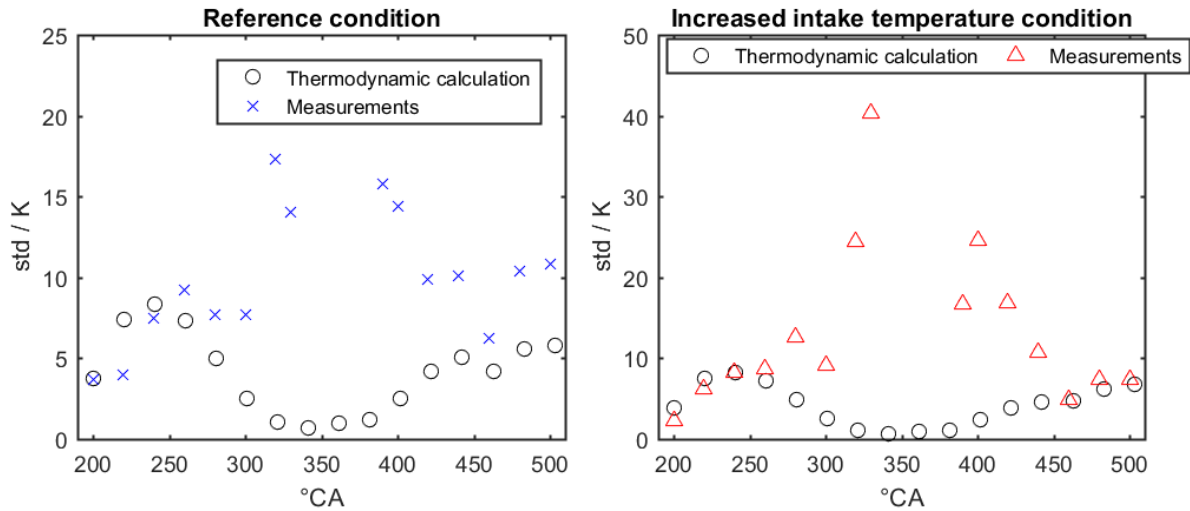


Figure 5-36: Comparison between the measured standard deviation (measurements) and the expected temperature variation based on a thermodynamic calculation. The comparison is made for the reference condition and increased intake temperature condition.

To compare the measured standard deviation to the expected cycle-to-cycle temperature variation, a thermodynamic calculation based on the cycle-to-cycle pressure traces is carried out. This comparison is performed based on the fact that the precision of the pressure measurement is high with respect to phosphor thermometry. Figure 5-36, shows the comparison between the measured standard deviation and the expected temperature variation based on the thermodynamic calculation. For crank angles near BDC corresponding to low temperature, the measured standard deviation quite well agrees with the expected temperature variation suggesting a high measurement precision. Approaching TDC, the measured STD is much higher than expected temperature variation based on the thermodynamic calculation. This result shows that cycle to cycle temperature fluctuations due to pressure fluctuations are not responsible for the measured standard deviation. The latter is therefore either due to the low measurement precision at high temperature (mainly due to the low signal-to-background ratio) or to stratification of the temperature induced by the wall heat transfer during the compression stroke. Again, since the former is was not determined in the present work, is was not possible to evaluate their respective contribution. In this context, the estimation of the measurement precision proposed here can be considered as a pessimistic temperature uncertainty since it might also include existing temperature stratification. In future experiments, the variation of background signal during measurements would need to be taken into account to quantify the associated temperature error. At this stage, further investigations are required to differentiate the effect of physical processes and measurement error on the measured temperature standard deviation.

---

---

## 6 INFLUENCE OF SPRAY AND COMBUSTION

### 6.1 Experiments in the presence of fuel injection

In-cylinder temperature measurements were also carried out in the presence of direct fuel injection under motored conditions. For these measurements, non-fluorescent *n*-pentane was chosen for its high volatility at room temperature. To speed up the spray evaporation after injection, the intake temperature was set to 333 K. The focus of the measurements was to investigate the ability of the technique to resolve changes to the in-cylinder temperature distribution caused by spray evaporation. For this purpose, two injection test cases based on two injection timings were investigated (170 and 220°CA, cf. Figure 6-1) that are expected to significantly influence the in-cylinder temperature distribution even if they are not representative for real engine conditions.

Injection specifications	
Injector type	Bosch GDI HDEV 5.2
Operating pressure	200 bar
Injection duration	1000 $\mu$ s
Injection timing	170°CA, 220°CA
Number of holes	5
Inlet temperature	60°C

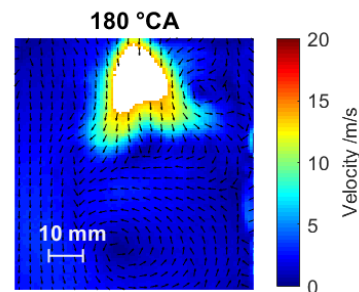


Figure 6-1: Left: Injection specifications in this study. Right: Time-averaged velocity field in the presence of spray injection at 180°CA with an injection timing of 170°CA. No gas-phase velocity information is available in the zone containing fuel droplets corresponding to the white zone.

PIV measurements were performed simultaneously with the temperature measurements. The Mie scattering images were additionally useful to visualize the fuel spray. An example of the time-averaged velocity field obtained at 180°CA with 170°CA injection timing is shown in Figure 6-1.

For 170°CA injection timing, the time-averaged in-cylinder temperature images are presented in Figure 6-2. The temperature images were taken at 190 and 200°CA (390  $\mu$ s and 1080  $\mu$ s after the end of injection, EOI, respectively). The temperature maps obtained with the spray injection are compared to temperature maps obtained without injection. Time-averaged PIV images at these crank angles are also presented in Figure 6-3. In the case of fuel injection, the time-averaged temperature images show a colder zone located in the center of the cylinder due to evaporation cooling. The presence of the spray in this zone is verified by the PIV images presented in Figure 6-3. To help visualize the difference in temperature distribution between the injection and the reference test case, the resulting horizontal temperature profiles are plotted on the right-hand side of the Figure 6-2. The horizontal temperature profiles are taken at 55 mm distance from the injector tip. This comparison indicates that between the two cases there is a maximum temperature difference of approximately 15 K (at 190°CA) and 10 K (at 200°CA). By performing a calculation based on adiabatic fuel-air mixing, using the spray model presented in [98], at the present conditions, the two-temperature gap measured would correspond to the fuel mass fraction of  $Y_f \sim 0.34$  and 0.24, respectively. The order of magnitude of the calculated fuel mass fraction is consistent with what expected at that stage of the mixing. This fact, together with the fact that the cooling

effect becomes smaller when passing from 190 to 200°CA confirms the consistency of the results. This effect is less visible in the single-shot temperature images, presented in Figure 6-4.

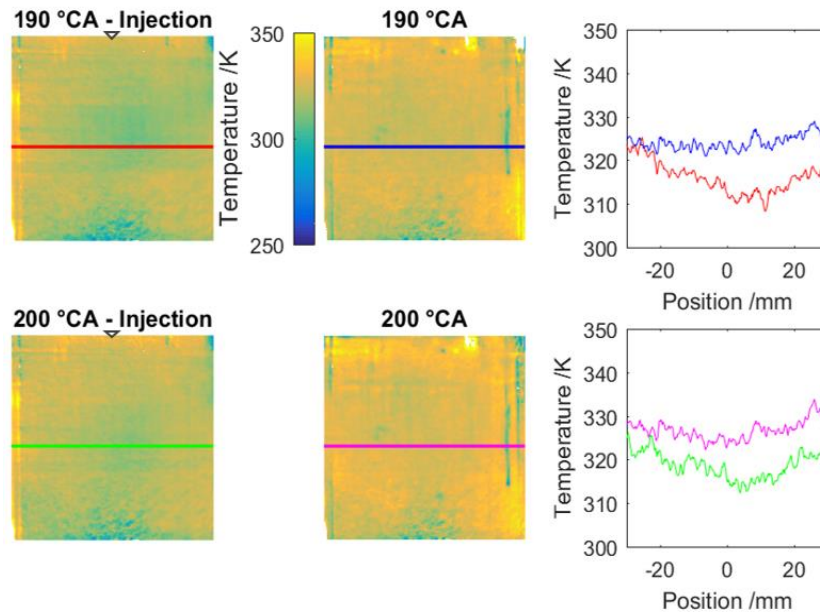


Figure 6-2: Time-averaged images of in-cylinder temperature after the injection of *n*-pentane at 170°CA (injection timing). The results are averaged over 100 engine cycles. The spray impact on the temperature field is visible by comparing measurements with and without injection obtained at 190 and 200°CA. A comparison of the horizontal temperature profiles is shown on the right. The triangles indicate the position of the injector.

The velocity field is modified by spray injection because the spray penetrates into the cylinder with high velocities, as shown in Figure 6-3. While the spray evaporation co-exists with the tumble flows at 190°CA, at 200°CA the spray interferes with the tumble flows resulting in a complex structure of the flow field. In modern engine technologies, the way how the fuel is injected into the cylinder is important to control the aerodynamic rotating flows and increase the overall engine efficiency.

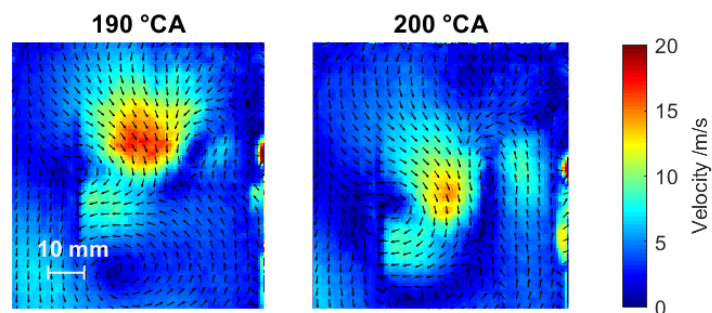


Figure 6-3: Time-averaged in-cylinder gas velocity field after the injection of *n*-pentane at 170°CA (injection timing). The results are averaged over 100 engine cycles.

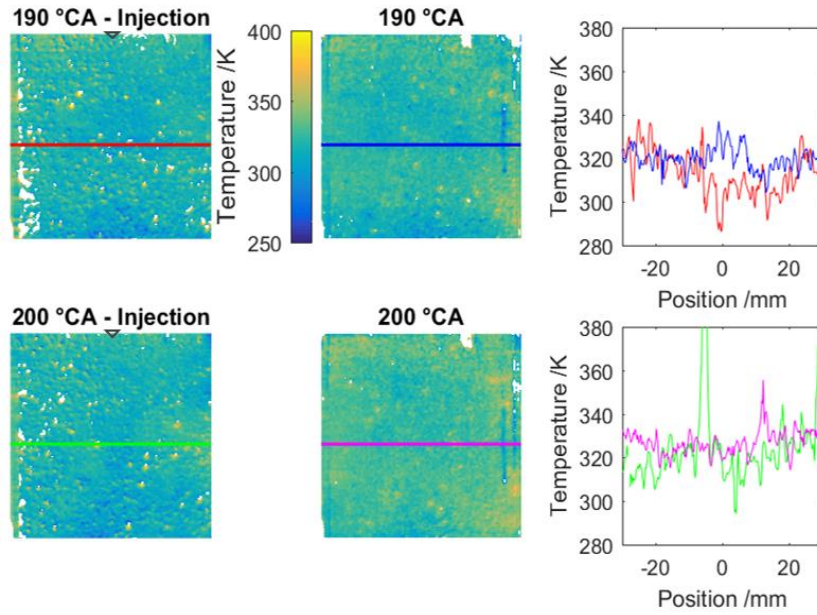


Figure 6-4: Single-shot temperature fields after injection of *n*-pentane at 170°CA. The influence of the spray on the temperature field is visible by comparing measurements with and without injection at 190 and 200°CA.

The results obtained with 220°CA injection timing are presented in Figure 6-5. The same spray-cooling effect in the order of 10 K is visible in the horizontal temperature profiles in Figure 6-5. The time-averaged velocity fields related to the injection test case are shown in Figure 6-6. In this case, the velocity field still shows the tumble flow. This is probably due to the later injection timing (220°CA) promoting the formation of a dominant tumble flow.

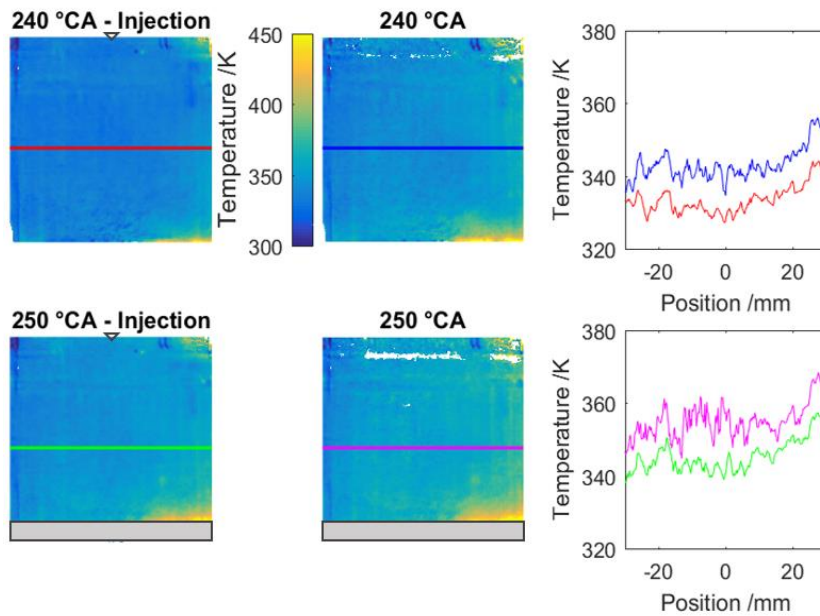


Figure 6-5: Time-averaged images of in-cylinder temperature after the injection of *n*-pentane at 220°CA. The results are averaged over 100 engine cycles. The spray impact on the temperature field is visible by comparing measurements with and without injection at 240 and 250°CA. A comparison of the horizontal temperature profiles is shown on the right. The triangles mark the position of the injector.

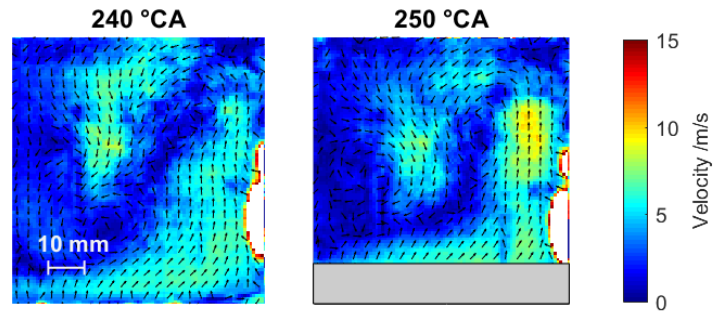


Figure 6-6: Time-averaged images of in-cylinder velocity field after the injection of *n*-pentane at 220°C. The results are averaged over 100 engine cycles.

## 6.2 Particle survival during combustion

In contrast to many other laser diagnostics techniques, phosphor thermometry can potentially be used to investigate the temperature in post-combustion gases. In this phase, the gas temperature can provide important information to understand wall heat-losses. Most tracer-based thermometry techniques cannot be employed for this purpose since organic tracers would be consumed during combustion. When using phosphor thermometry, however, one critical aspect is whether the phosphor particles “survive” the exposure to the high temperature and reacting environment of the combustion without disintegration and without changing their luminescent properties. In order to test the resistance of the phosphor particles to combustion, a series of temperature measurements were made in the post-combustion gas. In these measurements, only ZnO:Zn phosphor particles were tested. The measurements were performed at fixed engine timing (520°C) under 100 engine cycles. The engine timing of 520°C corresponds to the end of the expansion stroke and to lower in-cylinder temperatures during the exhaust valve opening. Therefore, this engine timing was chosen in order to discriminate the effect of the combustion from the effect of the high temperatures on the particles phosphorescence (thermal quenching). *Iso*-octane was injected in the center of the combustion chamber and ignition was initiated by the spark plug. The engine was operated under low-load conditions with an equivalence ratio of  $\phi = 0.8$  to prevent damage to the quartz cylinder and reduce flame temperature. The main combustion parameters are summarized in Table 6-1.

Table 6-1: Engine settings for fired operation.

Injection specifications			
Injector type	Bosch GDI HDEV 5.2	Type of fuel	<i>iso</i> -octane
Injection pressure	200 bar	Equivalence ratio	0.8
Injection duration	1000 $\mu$ s		
Injection timing	100°C		
Spark advance	342°C		
Intake air temperature	60°C		

Temperature images were taken over 50 engine cycles for both motored and fired operation to enable a fair comparison in terms of particle seeding density and window fouling. The time sequence is shown in Figure 6-7. Due to the lean mixture, the operating point revealed combustion instabilities causing some misfired cycles. This aspect was useful because it provided strong cycle-to-cycle temperature variations as also visible from the pressure traces in Figure 6-7.

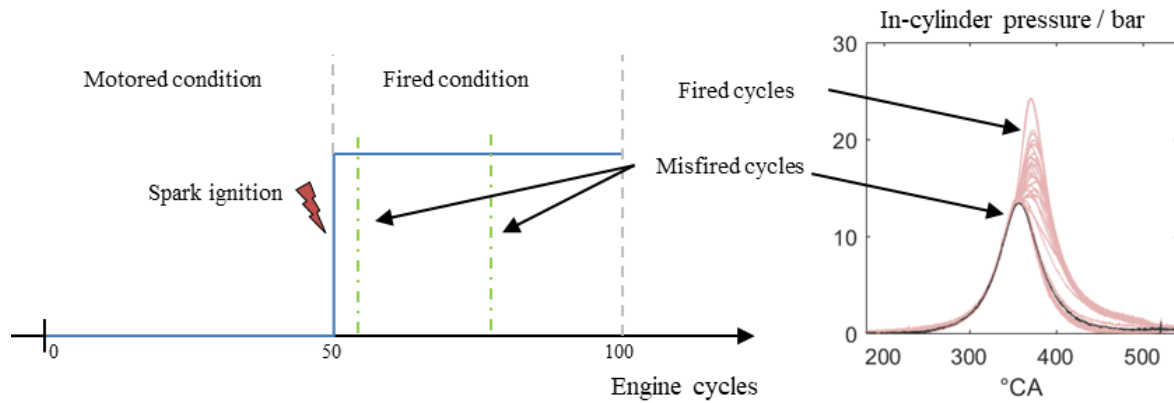


Figure 6-7: Time sequence of fired engine operation and related pressure traces.

Figure 6-10 shows single-shot temperature measurements (center column) along with the in-cylinder pressure trace (left column of the figure) and the averaged intensity signal on the cameras (right column). Starting from the first row, three engine operating conditions are presented: motored condition (first row), fired event (second and third row), misfired event (last row).

The three cases are described below:

1. Motored condition: As expected in this condition, there is no problem to perform temperature measurements with phosphor particles. The measured in-cylinder pressure trace is used to control the operating mode in which the measurement is performed. As shown in Figure 6-10 (right column). The average luminescence intensity signal on both cameras is sufficient for ratio-based thermometry on a single-shot level. Also, in this condition, the intensity signal on both cameras is almost constant for all engine cycles.
2. Fired condition: Under this condition, a strong reduction in signal intensity is observed on both cameras and it is not possible to perform thermometry measurements. Figure 6-8, shows the comparison of Mie-scattering images under motored and fired conditions. The Mie scattering image taken at 520°CA under fired condition shows that only few particles are still present in the measurement plane after combustion event when a large number of particles was visible at motored conditions. In this condition, the luminescence intensity signal is quite low preventing any temperature measurements, as shown in Figure 6-10 (right column). It is not clear what is the impact of the combustion event on the phosphor particles, therefore few hypotheses are presented.

The first hypothesis is that the phosphor particles are degraded by the high temperature reached during the combustion. Figure 6-9, shows the adiabatic in-cylinder temperature estimated from a thermodynamic calculation based on the measured pressure traces. Depending on the type of combustion observed, the maximum temperature reached by the particles is estimated to be between 1000 K and 1350 K that is quite below the expected melting temperature of the ZnO:Zn phosphor

---

(2000 K, [99]). Therefore, the loss of the luminescence signal should not be attributed to a modification of the physical state of the particles.

Also, the lower Mie scattering signal indicates a decrease of the particles number density in the measurement plane. This could be caused by the gas expansion due to the high temperature condition after the combustion event. Therefore, a lower particles number density combined with high temperature condition could be a possible cause of the lack of luminescence signal after the combustion event.

The second hypothesis is that the particles could be chemically transformed after the combustion event altering the luminescence properties of the phosphor. In fact, the excess of oxygen (due to the lean combustion mode), during combustion, could be the cause of a probable oxidation of zinc oxide, corrupting the luminescence properties of this material. At this stage, both hypotheses are opened and further investigations are needed to study the particle behavior during combustion.

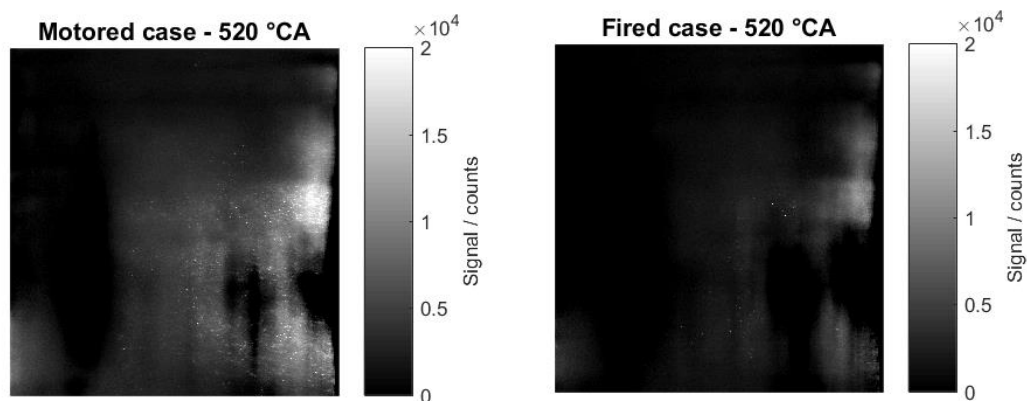


Figure 6-8: Mie scattering images taken during measurements in motored (left) and fired (right) condition.

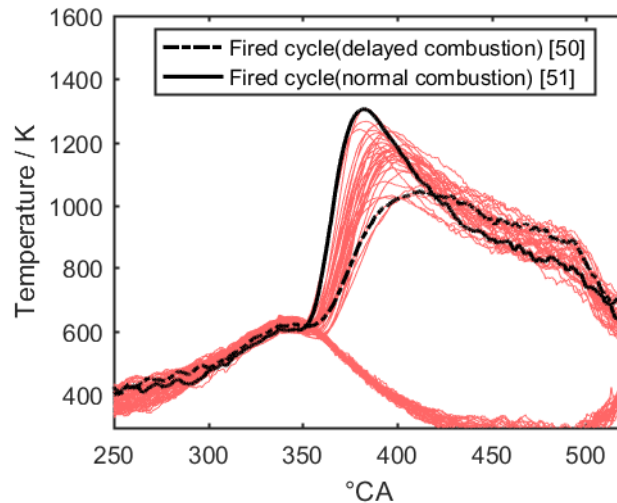


Figure 6-9: Adiabatic in-cylinder temperature estimation based on thermodynamic calculation of the measured in-cylinder pressure traces. In black the temperature profiles correspond to two fired cycles with a delayed combustion (dashed line) and “normal” combustion.

3. Misfired condition: During the misfired cycles, temperature measurements are still possible as the mixture has not been ignited. Compared to the motored case, some inhomogeneities of

the temperature field are observed that are attributed to the backflow gases occurring at this crank angle (the exhaust valve is open promoting a reverse flow into the cylinder). Note that in this case, due to the previous fired cycles, the backflow gases are hotter compared to the motored case, promoting a non-homogenous in-cylinder temperature distribution.

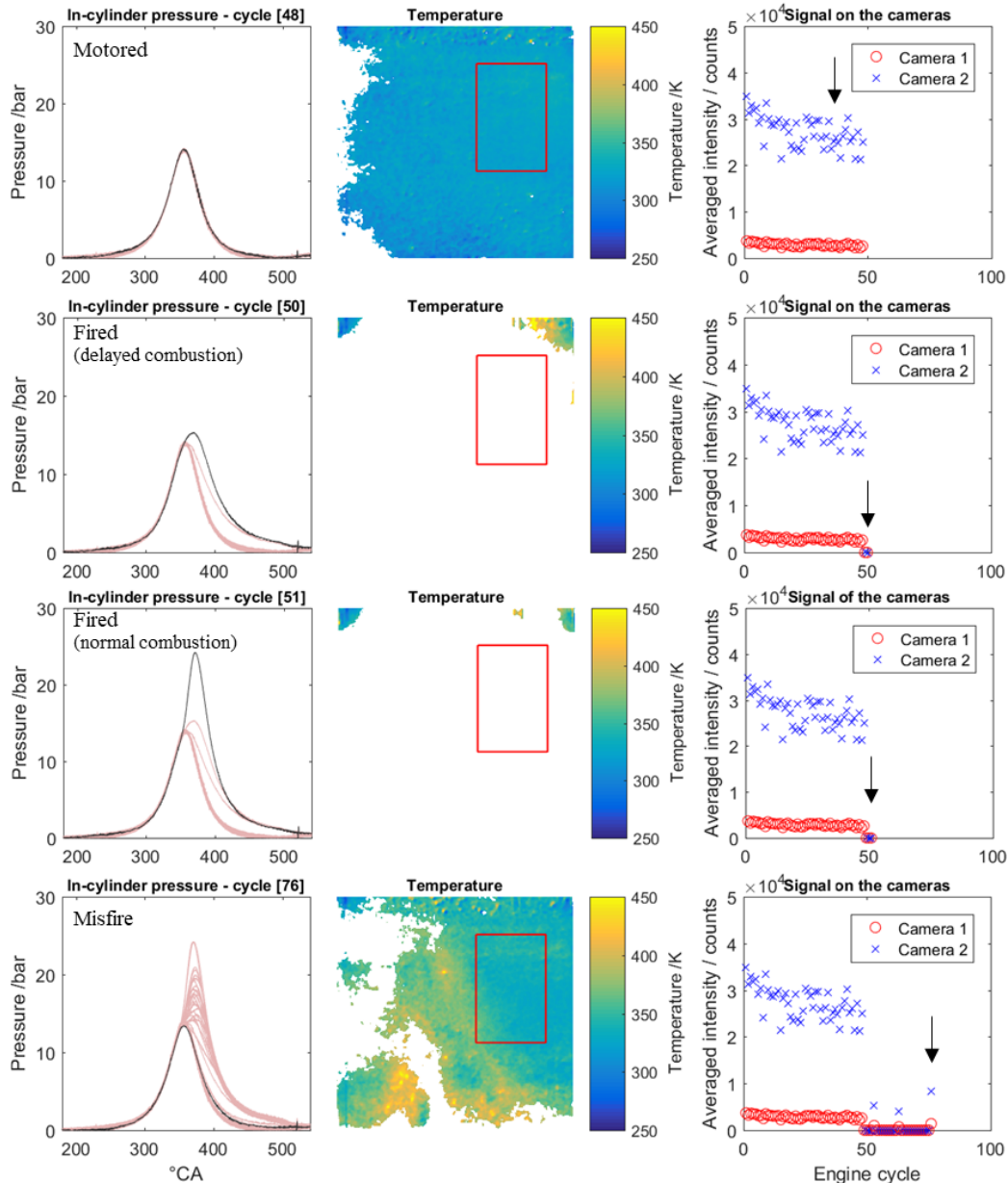


Figure 6-10: Series of single-shot temperature measurements obtained at 520°CA during motored (first row), fired (second and third rows) and misfired (last row) engine cycles. The respective in-cylinder pressure traces are presented in the first column. The pressure trace in black corresponds to the current engine cycle. The pressure traces in red, correspond to the previously measured cycles. The variation of the averaged intensity signal on the two ICCD cameras during the engine cycle is presented in the third column. The last data points on the graphs indicate the averaged signal intensity corresponding to the current engine cycle. The red rectangle in the temperature images shows the zone where the averaged signal intensity is determined for both cameras.

---

## 7 PERSPECTIVES AND CONCLUSIONS

### 7.1 Perspectives

In this work, the potential of thermographic PIV for the simultaneous temperature and velocity field measurement in an optical engine was investigated. Based on the results obtained, several key areas for future works are identified, in particular, improvements of thermographic PIV technique and new applications in IC engine.

#### 7.1.1 Diagnostics improvements

Thermographic PIV technique is based on the use of thermographic phosphor particles as tracers for gas-phase temperature and velocity measurements. The feasibility of this technique relies on the photo-physical properties of the phosphor. The selection of a suitable phosphor material for engine measurements is a crucial task due to high-temperature conditions in a confined harsh environment. In this work, ZnO:Zn was chosen as phosphor after a comparison with two further commercially available phosphors: BAM and ZnO. It was found that ZnO:Zn enables accurate and precise temperature measurements in motored engine conditions. However, using this phosphor it was not possible to perform measurements in fired conditions due to a loss of the luminescence signal. The high in-cylinder temperatures combined with a probable particle degradation during the combustion are supposed to prevent temperature measurements. Therefore, one of the main improvements proposed for the phosphor thermometry under fired conditions is related to the search of phosphors capable to resist in fired conditions and allowing measurements in- and post-flame zone. From the results obtained in this work, it is advised to choose a phosphor made with a host material that is not altered in the flame.

Most of the phosphors used for phosphor thermometry were originally designed for commercial lighting applications (e.g., fluorescent lamps, CRT screens, etc.). Also, most of these phosphors have been characterized in conditions far away from those required for gas thermometry applications. Therefore, future developments are required in two key areas.

- Investigation of available phosphors: There are still many commercial phosphors designed for other applications that need to be characterized and compared for gas thermometry application under controlled conditions (laser fluence, seeding density, aerosolized condition, etc.). In this sense, the definition of an experimental procedure for characterization will help in this crucial task.
- Phosphor design: Suitable phosphors with desired characteristics (high quantum efficiency, high sensitivity to temperature variation, short lifetime, etc.) that resist combustion could be specifically designed for gas thermometry. This strategy can be the key of success on the development of this technique for a large variety of application with different temperature ranges.

Additional improvement is required for optimized phosphor particle seeding. As shown in Chapter 5, the quality of the single-shot temperature and velocity images are affected by the inhomogeneous particle distribution. Before this work, T-PIV was employed in a basic experimental apparatus like Bunsen burner or turbulent heated jet where the seeding density can be controlled over the entire measurement timing. In engine measurements, the phosphor particles are seeded from the intake manifold during the

---

intake stroke without any possibility to control the seeding density during the entire engine cycle. Therefore, maintaining a constant and homogeneous seeding density over the intake stroke is important. Future improvements must include new seeders with controllable particle number density minimizing agglomeration. The particle seeding also depends on the particle shape and size. An improvement of the particle manufacturing process can thus be helpful.

It was shown in Chapter 5 that some of the in-cylinder temperature measurements were affected by systematic particle number density inhomogeneities. Additional features in the detected images like vertical and horizontal lines were caused by the progressive wear of the cylinder surfaces. Other features including spots were generated from the imperfect background correction unable to completely eliminate laser scattering. One way to reduce the sensitivity of the measurement on the above mentioned effects can be the use of SLIPI (structured laser illumination planar imaging). SLIPI uses a structured laser light sheet to distinguish the directly detected signal light from blurred signal that results from secondary scattering and other background. The modulation of the incoming laser light sheet is preserved in the luminescence from the measurement plane while secondary scattered luminescence from particles elsewhere (i.e., on the windows) that are illuminated by scattered laser light are unstructured. In a reconstruction of two or even three quasi-simultaneously recorded images with shifted modulation patterns, the signal from the plane of interest can be reconstructed. This approach can be a powerful tool to improve the quality of the temperature images in a harsh confined environment like an engine. Another way to reduce signal generated and scattered from the surfaces is minimizing particle deposition on the cylinder walls. This is possible by using coated phosphor particles that reduce electrostatic forces and thus particle sticking.

The engine measurements presented in Chapter 5 were performed at low repetition rate. In future, this type of measurements can be also performed at high repetition rate (kHz) offering the opportunity to perform cinematographic measurements of the temperature and velocity fields during the entire engine cycle. From a theoretical point of view, thermographic PIV can also be combined with stereoscopic detection enabling instantaneous measurements of the velocity components together with a (slightly blurred) temperature field in a defined measurement plane.

### 7.1.2 Applications of T-PIV in IC engines

In engine development, several key areas are still under investigations to increase efficiency while reducing pollutant formation. In this sense, thermographic PIV offers the possibility to investigate complex phenomena where the temperature and velocity fields are important. T-PIV can be used to improve the understanding of fluctuating in-cylinder processes by measuring the cycle-to-cycle variations under different operating conditions. In this study, the impact of the tumble flow on the in-cylinder temperature distribution was investigated.

Analyzing the cycle-to-cycle fluctuations of the temperature and velocity fields, T-PIV can be used to study, e.g., unwanted ignition and combustion phenomena that are highly relevant for designing new highly-efficient engines. Autoignition strongly depends on temperature and is influenced by the fluid flow in the engine. For detailed investigations of these processes, T-PIV can be highly valuable.

Heat losses to the cylinder walls affect the thermal efficiency of an engine. For this reason, thermal barrier coatings are developed to minimize the heat losses and improve the fuel economy. T-PIV is a

---

powerful tool to compare the effect of different coating materials and thicknesses by observing their effect on the in-cylinder gas temperature and motion.

## 7.2 Conclusions

The main objective of this work was to simultaneously measure temperature and velocity in the cylinder of an optically accessible engine in motored operation. Simultaneous phosphor thermometry and particle image velocimetry (PIV) was chosen for this study. The combination of these diagnostics referred as thermographic PIV (T-PIV) was developed for measurements in IC engine. The work presented in this thesis provides two main developments of the technique.

Suitable phosphor materials for engine measurements were chosen from three commercially available phosphors: BAM:Eu<sup>2+</sup>, ZnO and ZnO:Zn. A methodology was implemented to characterize the phosphors on both phosphor-coated surfaces and aerosolized particles. The luminescence and intensity-ratio response of the phosphors to various parameters including temperature were measured resulting in temperature-dependent calibration curves for two-color signal intensity ratios to be used for the analysis of measurements obtained from engine experiments. To assess the influence of experimental parameters, the phosphors were characterized via parametric variations of seeding density, impact of laser fluence, and temperature. In this task, a dedicated particle counting system able to resolve particle number densities in the range of 10<sup>10</sup>–10<sup>11</sup> particles/m<sup>3</sup> was developed. A comparison of the luminescence properties obtained from surface and aerosol measurements was performed and the obtained results showed that the aerosol characterization is more representative for the engine application of phosphor thermometry. Based on the results presented in section 4.5, ZnO:Zn shows a stronger sensitivity to temperature compared to BAM:Eu<sup>2+</sup>, increasing temperature precision. Also, compared to ZnO, ZnO:Zn shows slightly higher luminescence intensity. For these reasons, ZnO:Zn was chosen in this work as candidate for the engine measurements.

One of the novelties of this work was the use of ZnO:Zn with a particle size of 3.5 μm as a tracer for temperature and velocity measurements in an optically-accessible engine. The engine application under multiple operating conditions was used to extend the validation of T-PIV in an engine environment and to evaluate the experimental uncertainties.

Time-averaged and single-shot temperature measurement maps show good agreement with the temperature variation predicted from zero-dimensional simulations for the compression and the expansion stroke. The obtained averaged temperature fields showed deviation from the simulation of about 1% (200°C) to 14% (480°C). These deviations were considered in the accuracy limits of the simulation. Moreover, measurements performed with increased intake temperature show a maximum temperature deviation of around 10% at 390°C resulting in good agreement with the temperature predicted by the 0D simulation.

The measurement accuracy related to calibration was found to be 55 K (18%) at 300 K and 2 K (0.3%) at 614 K for the 200-cycle average. This shows a promise for accurate temperature measurements at higher temperatures (near TDC) in future experiments. The precision of the temperature measurement was evaluated by comparing the shot-to-shot measurement to the pressure-derived temperature. The results indicated good precision near the bottom dead center (similar shot-to-shot dispersion between the two temperatures) and lower precision near top dead center.

---

For the first time, the effect of the tumble on the temperature field was investigated with T-PIV. The results show a small decrease in temperature from 9 K (300°C) to 19 K (330°C) during the compression stroke where the increased rotating flows are expected to enhance the wall heat transfer. The same decrease in temperature is also visible during the expansion stroke, with a maximum temperature difference of 32 K (480°C) compared to the reference case.

The ability of the technique to resolve temperature distributions was also demonstrated in cases with spray-evaporation-induced temperature stratification. The resulting temperature fields after fuel injection show a spray cooling in the order of 10 K confined to the center of the cylinder where the fuel evaporates.

One critical aspect of phosphor thermometry is whether the particles survive the exposure to the flame front. The resistance of the phosphor particles to combustion was investigated in a series of temperature measurements in fired conditions. It was found that the ZnO:Zn phosphor used does not allow post-flame measurements. The lack of the luminescence intensity signal prevents temperature measurements. This aspect limits the use of ZnO:Zn phosphor exclusively to the measurements in motored and misfired conditions.

---

## 8 REFERENCES

- [1] Dec JE. Advanced compression-ignition engines, understanding the in-cylinder processes. *Proceedings of the Combustion Institute* 2009;32(2):2727–42.
- [2] Allison SW GG. Remote thermometry with thermographic phosphors: Instrumentation and applications. *Review of Scientific Instruments* 1997;68(7):2615.
- [3] Abram C, Fond B, Beyrau F. Temperature measurement techniques for gas and liquid flows using thermographic phosphor tracer particles. *Progress in Energy and Combustion Science* 2018(64):93–156.
- [4] Aldén M, Omrane A, Richter M, Särner G. Thermographic phosphors for thermometry: A survey of combustion applications. *Progress in Energy and Combustion Science* 2011;37(4):422–61.
- [5] Hasegawa R, Sakata I, Yanagihara H., Särner G., Richter M., Aldén M et al. Two-Dimensional Temperature Measurements in Engine Combustion Using Phosphor Thermometry. In: *SAE Technical Paper 2009-24-0033*, 2009,
- [6] Neal NJ, Jordan J, Rothamer D. Simultaneous Measurements of In-Cylinder Temperature and Velocity Distribution in a Small-Bore Diesel Engine Using Thermographic Phosphors. *SAE International Journal of Engines* 2013;6(1):300–18.
- [7] Takada N, Sakata I, Yanagihara H, Lindén J, Richter M, Aldén M, Johansson B. Two-Dimensional Temperature Measurements in Diesel Piston Bowl Using Phosphor Thermometry. In: *SAE Technical Paper 2009-24-0033*, 2009.
- [8] Zhang Z. *LDA Application Methods*. Berlin, Heidelberg: Springer Berlin Heidelberg; 2010.
- [9] Raffel M. *Particle image velocimetry: A practical guide*. 2nd ed. Heidelberg, New York: Springer; 2007.
- [10] Cavazzini G. *The Particle Image Velocimetry - Characteristics, Limits and Possible Applications: InTech*; 2012.
- [11] Prasad AK. Stereoscopic particle image velocimetry. *Experiments in Fluids* 2000;29(2):103–16.
- [12] Bücker I, Karhoff D-C, Klaas M, Schröder W. Stereoscopic multi-planar PIV measurements of in-cylinder tumbling flow. *Experiments in Fluids* 2012;53(6):1993–2009.
- [13] Elsinga GE, Scarano F, Wieneke B, van Oudheusden BW. Tomographic particle image velocimetry. *Experiments in Fluids* 2006;41(6):933–47.
- [14] Singh AP, Gupta A, Agarwal AK. Tomographic Particle Image Velocimetry for Flow Analysis in a Single Cylinder Optical Engine. *SAE International Journal of Materials and Manufacturing* 2015;8(2):472–81.
- [15] Bevan KE, Ghandhi JB. PIV Measurements of In-Cylinder Flow in a Four-Stroke Utility Engine and Correlation with Steady Flow Results. In: *SAE Technical Paper 2004-32-0005*, 2004.
- [16] Zhao F-Q, Hiroyasu H. The applications of laser Rayleigh scattering to combustion diagnostics. *Progress in Energy and Combustion Science* 1993;19(6):447–85.

- 
- [17] Richard BM, Walter RL, Joseph NF. Laser Rayleigh scattering. *Measurement Science and Technology* 2001;12(5):R33.
- [18] Boguszko M EG. On the use of filtered Rayleigh scattering for measurements in compressible flows and thermal fields. *Experiments in Fluids* 2005;38(1):33–49.
- [19] Yalin AP, Miles RB. Ultraviolet filtered Rayleigh scattering temperature measurements with a mercury filter. *Optics Letters* 1999;24(9):590.
- [20] Müller D, Pagel R, Burkert A, Wagner V, Paa W. Two-dimensional temperature measurements in particle loaded technical flames by filtered Rayleigh scattering. *Applied Optics* 2014;53(9):1750–8.
- [21] Gregory S Elliott and Nick Glumac and Campbell D Carter. Molecular filtered Rayleigh scattering applied to combustion. *Measurement Science and Technology* 2001;12(4):452.
- [22] Most D, Leipertz A. Simultaneous two-dimensional flow velocity and gas temperature measurements by use of a combined particle image velocimetry and filtered Rayleigh scattering technique. *Applied Optics* 2001;40(30):5379.
- [23] Stockhausen G, Doll U, Strehlau T, Willert C. Combined filtered Rayleigh and Mie scattering for simultaneous planar temperature and velocity measurements. 15th Int Symp on Applications of Laser Techniques to Fluid Mechanics to Fluid Mechanics Lisbon, Portugal, 05-08 July, 2010.
- [24] Eckbreth AC. *Laser diagnostics for combustion temperature and species*. 2nd ed. Amsterdam, United Kingdom: Gordon & Breach; 1996.
- [25] Kohse-Höinghaus K, Jeffries JB. *Applied combustion diagnostics*. New York, London: Taylor & Francis; 2002.
- [26] Brackmann C, Bood J, Afzelius M, Bengtsson PE. Thermometry in internal combustion engines via dual-broadband rotational coherent anti-Stokes Raman spectroscopy. *Measurement Science and Technology* 2004;15(3):R13.
- [27] Weigl MC, Beyrau F, Leipertz A. Simultaneous temperature and exhaust-gas recirculation-measurements in a homogeneous charge-compression ignition engine by use of pure rotational coherent anti-Stokes Raman spectroscopy. *Applied Optics* 2006;45(15):3646.
- [28] Beyrau F, Bräuer A, Seeger T, Leipertz A. Gas-phase temperature measurement in the vaporizing spray of a gasoline direct-injection injector by use of pure rotational coherent anti-Stokes Raman scattering. *Optics Letters* 2004;29(3):247.
- [29] Bohlin A, Kliwer CJ. Communication: Two-dimensional gas-phase coherent anti-Stokes Raman spectroscopy (2D-CARS): Simultaneous planar imaging and multiplex spectroscopy in a single laser shot. *The Journal of Chemical Physics* 2013;138(22):221101.
- [30] Schulz C, Sick V. Tracer-LIF diagnostics: Quantitative measurement of fuel concentration, temperature and fuel/air ratio in practical combustion systems. *Progress in Energy and Combustion Science* 2005;31(1):75–121.
- [31] Koban W, Koch JD, Hanson RK, Schulz C. Toluene LIF at elevated temperatures: implications for fuel-air ratio measurements. *Applied Physics B* 2004;80(2):147–50.
-

- 
- [32] Tea G, Bruneaux G, Kashdan JT, Schulz C. Unburned gas temperature measurements in a surrogate Diesel jet via two-color toluene-LIF imaging. *Proceedings of the Combustion Institute* 2011;33(1):783–90.
- [33] Devillers R, Bruneaux G, Schulz C. Development of a two-line OH-laser-induced fluorescence thermometry diagnostics strategy for gas-phase temperature measurements in engines. *Applied Optics* 2008;47(31):5871.
- [34] Burns IS, Hult J, Hartung G, Kaminski CF. A thermometry technique based on atomic lineshapes using diode laser LIF in flames. *Proceedings of the Combustion Institute* 2007;31(1):775–82.
- [35] Hildenbrand F, Schulz C, Hartmann M, Puchner F, Wawrschin G. In-Cylinder NO-LIF Imaging in a Realistic GDI Engine Using KrF Excimer Laser Excitation. In: *SAE Technical Paper Series 1999-01-3545*.
- [36] Kaminski CF, Engström J, Aldén M. Quasi-instantaneous two-dimensional temperature measurements in a spark ignition engine using 2-line atomic fluorescence. *International Symposium on Combustion* 1998;27(1):85–93.
- [37] Bessler WG, Hofmann M, Zimmermann F, Suck G, Jakobs J, Nicklitzsch S et al. Quantitative in-cylinder NO-LIF imaging in a realistic gasoline engine with spray-guided direct injection. *Proceedings of the Combustion Institute* 2005;30(2):2667–74.
- [38] Bessler WG, Hildenbrand F, Schulz C. Two-line laser-induced fluorescence imaging of vibrational temperatures in a NO-seeded flame. *Applied Optics* 2001;40(6):748.
- [39] Bessler WG, Schulz C. Quantitative multi-line NO-LIF temperature imaging. *Applied Physics B* 2004;78(5):519–33.
- [40] Schulz C, Sick V, Wolfrum J, Drewes V, Zahn M, Maly R. Quantitative 2D single-shot imaging of NO concentrations and temperatures in a transparent SI engine. *International Symposium on Combustion* 1996;26(2):2597–604.
- [41] Dec JE, Hwang W. Characterizing the Development of Thermal Stratification in an HCCI Engine Using Planar-Imaging Thermometry. *SAE Int. J. Engines*, 2(1):421-438, 2009.
- [42] Kaiser SA, Schild M, Schulz C. Thermal stratification in an internal combustion engine due to wall heat transfer measured by laser-induced fluorescence. *Proceedings of the Combustion Institute* 2013;34(2):2911–9.
- [43] Peterson B, Baum E, Böhm B, Sick V, Dreizler A. Evaluation of toluene LIF thermometry detection strategies applied in an internal combustion engine. *Applied Physics B* 2014;117(1):151–75.
- [44] Peterson B, Baum E, Böhm B, Sick V, Dreizler A. High-speed PIV and LIF imaging of temperature stratification in an internal combustion engine. *Proceedings of the Combustion Institute* 2013;34(2):3653–60.
- [45] Peterson B, Baum E, Böhm B, Sick V, Dreizler A. Spray-induced temperature stratification dynamics in a gasoline direct-injection engine. *Proceedings of the Combustion Institute* 2015;35(3):2923–31.
-

- 
- [46] Kaiser S, White CM. PIV and PLIF to Evaluate Mixture Formation in a Direct-Injection Hydrogen-Fuelled Engine. *SAE International Journal of Engines* 1(1):657-668, 2009.
- [47] Brübach J, Feist JP, Dreizler A. Characterization of manganese-activated magnesium fluorogermanate with regards to thermographic phosphor thermometry. *Measurement Science and Technology* 2008;19(2):25602.
- [48] Melling A. Tracer particles and seeding for particle image velocimetry. *Measurement Science and Technology* 1997;8(12):1406–16.
- [49] Fond B, Abram C, Beyrau F. On the characterisation of tracer particles for thermographic particle image velocimetry. *Applied Physics B* 2015;118(3):393–9.
- [50] Abram C. High Repetition Rate Temperature and Velocity Imaging in Turbulent Flows using Thermographic Phosphors. Department of Mechanical Engineering, Imperial College London; 2014.
- [51] Knappe C. Phosphor thermometry on surfaces: A study of its methodology and its practical applications. Lund: Division of Combustion Physics, Department of Physics, Lund University; 2013.
- [52] Fond B. Simultaneous temperature and velocity imaging in turbulent flows using thermographic phosphor tracer particles. Department of Mechanical Engineering, Imperial College London; 2014.
- [53] M. Yen W, Shionoya S, Yamamoto H. *Phosphor Handbook*: 2nd Ed.: CRC Press; 2007.
- [54] Lin Y-C, Karlsson M, Bettinelli M. Inorganic Phosphor Materials for Lighting. *Topics in Current Chemistry* 2016;374(2):21.
- [55] Blasse G, Grabmaier BC. *Luminescent Materials*. Berlin, Heidelberg: Springer Berlin Heidelberg; 1994.
- [56] Ronda CR. *Luminescence: From theory to applications*. Weinheim: Wiley-VCH; 2008.
- [57] Dorenbos P. Electronic structure engineering of lanthanide activated materials. *The Journal of Chemical Physics* 2012;22(42):22344–9.
- [58] M. Yen W, J. Weber M. *Inorganic Phosphors: Compositions, preparation and optical properties*: CRC Press; 2004.
- [59] Riseberg LA, Moos HW. Multiphonon Orbit-Lattice Relaxation of Excited States of Rare-Earth Ions in Crystals. *Physical Review* 1968;174(2):429–38.
- [60] Brübach J, Pflitsch C, Dreizler A, Atakan B. On surface temperature measurements with thermographic phosphors: A review. *Progress in Energy and Combustion Science* 2013;39(1):37–60.
- [61] Brübach J, Kissel T, Frotscher M, Euler M, Albert B, Dreizler A. A survey of phosphors novel for thermography. *Journal of Luminescence* 2011;131(4):559–64.
- [62] Fuhrmann N, Kissel T, Dreizler A, Brübach J. Gd<sub>3</sub>Ga<sub>5</sub>O<sub>12</sub>:Cr-a phosphor for two-dimensional thermometry in internal combustion engines. *Measurement Science and Technology* 2011;22(4):45301.
- [63] Goss LP, Smith AA, Post ME. Surface thermometry by laser-induced fluorescence. *Review of Scientific Instruments* 1989;60(12):3702–6.
-

- 
- [64] Feist JP, Heyes AL, Choy KL, Su B (eds.). Phosphor thermometry for high temperature gas turbine applications: ICIA SF 99. 18th International Congress on Instrumentation in Aerospace Simulation Facilities. Record (Cat. No.99CH37025), Toulouse, France, 1999, pp. 6/1-6/7.
- [65] Feist JP HA. The characterization of Y<sub>2</sub>O<sub>2</sub>S: Sm powder as a thermographic phosphor for high temperature applications. *Measurement Science and Technology* 2000;11(7):942–7.
- [66] Jordan J RD. Pr:YAG temperature imaging in gas-phase flows. *Applied Physics B* 2013;110(3):285–91.
- [67] Kaczkan M, Boruc Z, Fetlinski B, Turczynski S, Malinowski M. Temperature dependence of 3P<sub>0</sub> Pr<sup>3+</sup> fluorescence dynamics in Y<sub>4</sub>Al<sub>2</sub>O<sub>9</sub> crystals. *Applied Physics B* 2013;113(2):277–83.
- [68] Jordan J RD. Pr:YAG temperature imaging in gas-phase flows. *Applied Physics B* 2013;110(3):285–91.
- [69] Fond B, Abram C, Beyrau F. Characterisation of the luminescence properties of BAM: Eu<sup>2+</sup> particles as a tracer for thermographic particle image velocimetry. *Applied Physics B* 2015;121(4):495–509.
- [70] Abram C, Fond B, Beyrau F. High-precision flow temperature imaging using ZnO thermographic phosphor tracer particles. *Optics express* 2015;23(15):19453–68.
- [71] Särner G, Richter M, Aldén M. Investigations of blue emitting phosphors for thermometry. *Measurement Science and Technology* 2008;19(12):125304.
- [72] Omrane A, Ossler F, Alden M. Two-Dimensional Surface Temperature Measurements of Burning Materials. *Proceedings of the Combustion Institute* 29(2):2653-2659 2002.
- [73] Omrane A, Särner G, Aldén M. 2D-temperature imaging of single droplets and sprays using thermographic phosphors. *Applied Physics B* 2004;79(4):431–4.
- [74] Heyes AL, Seefeldt S, Feist JP. Two-colour phosphor thermometry for surface temperature measurement. *Colour and Design in the natural and man-made worlds* 2006;38(4–6):257–65.
- [75] Brübach J, Patt A, Dreizler A. Spray thermometry using thermographic phosphors. *Applied Physics B* 2006;83(4):499–502.
- [76] Tobin KW, Allison SW, Cates MR, Capps GJ, Beshears DL. High-temperature phosphor thermometry of rotating turbine blades. *AIAA Journal* 1990;28(8):1485–90.
- [77] Fond B, Abram C, Heyes AL, Kempf AM, Beyrau F. Simultaneous temperature, mixture fraction and velocity imaging in turbulent flows using thermographic phosphor tracer particles. *Optics express* 2012;20(20):22118–33.
- [78] Abram C, Fond B, Heyes A, Beyrau F. High-speed planar thermometry and velocimetry using thermographic phosphor particles. *Applied Physics B* 2013;111(2):155–60.
- [79] Dronniou N, Dec JE. Investigating the Development of Thermal Stratification from the Near-Wall Regions to the Bulk-Gas in an HCCI Engine with Planar Imaging Thermometry. *SAE International Journal of Engines* 2012;5(3):1046–74.
-

- 
- [80] Van Lipzig JPJ, Yu M, Dam NJ, Luijten CC, M. de Goey LPH. Gas-phase thermometry in a high-pressure cell using BaMgAl<sub>10</sub>O<sub>17</sub>: Eu as a thermographic phosphor. *Applied Physics B* 2013;111(3):469–81.
- [81] Zhang S, Kono T, Ito A, Yasaka T, Uchiike H. Degradation mechanisms of the blue-emitting phosphor BaMgAl<sub>10</sub>O<sub>17</sub>: Eu<sup>2+</sup> under baking and VUV-irradiating treatments. *Journal of Luminescence* 2004;106(1):39–46.
- [82] Yu M, Särner G, Luijten CCM, Richter M, Aldén M, Baert RSG et al. Survivability of thermographic phosphors (YAG: Dy) in a combustion environment. *Measurement Science and Technology* 2010;21(3):37002.
- [83] Bizarri G, Moine B. On phosphor degradation mechanism: Thermal treatment effects. *Journal of Luminescence* 2005;113(3-4):199–213.
- [84] Särner G, Richter M, Alden M. Two-dimensional thermometry using temperature-induced line shifts of ZnO:Zn and ZnO:Ga fluorescence. *Optics Letters* 2008;33(12):1327–9.
- [85] Fan L, Gao Y, Hayakawa A, Hochgreb S. Simultaneous, two-camera, 2D gas-phase temperature and velocity measurements by thermographic particle image velocimetry with ZnO tracers. *Experiments in Fluids* 2017;58(4):155.
- [86] Khalid AH, Kontis K. Thermographic Phosphors for High Temperature Measurements: Principles, Current State of the Art and Recent Applications. *Sensors* 2008;8(9):5673–744.
- [87] Long DA. Handbook of Raman spectroscopy. From the research laboratory to the process line. Edited by Ian R. Lewis and Howell G. M. Edwards. Marcel Dekker, New York and Basel, 2001. *J. Raman Spectrosc.* 2004;35(1):91.
- [88] Princenton Instruments - Acton. PI-MAX2: 1003 Specifications.
- [89] Moffat RJ. Describing the uncertainties in experimental results. *Experimental Thermal and Fluid Science* 1988;1(1):3–17.
- [90] Berntsson, Andreas W, Josefsson, Göran, Ekdahl R, Ogink R, Grandin B. The Effect of Tumble Flow on Efficiency for a Direct Injected Turbocharged Downsized Gasoline Engine. *SAE International Journal of Engines* 2011;4(2):2298–311.
- [91] Hill PG, Zhang D. The effects of swirl and tumble on combustion in spark-ignition engines. *Progress in Energy and Combustion Science* 1994;20(5):373–429.
- [92] Maligne D, Kashdan J, Ricordeau V. Base de données ide: moteur optique: Projet ICAMDAC - phase 4.1. IFPEN.
- [93] Woschni G. A Universally Applicable Equation for the Instantaneous Heat Transfer Coefficient in the Internal Combustion Engine. In: *SAE Technical Paper Series 670931*, 1967.
- [94] Lafossas F-A, Colin O, Le Berr F, Menegazzi P. Application of a New 1D Combustion Model to Gasoline Transient Engine Operation. In: *SAE Technical Paper 2005-01-2107*.
- [95] Richard S, Bougrine S, Font G, Lafossas F-A, Le Berr F. On the Reduction of a 3D CFD Combustion Model to Build a Physical 0D Model for Simulating Heat Release, Knock and Pollutants in SI Engines. *Oil & Gas Science and Technology* 2009;64(3):223–42.
-

- 
- [96] Kashdan JT, Bruneaux G. Laser-Induced Phosphorescence Measurements of Combustion Chamber Surface Temperature on a Single-Cylinder Diesel Engine. In: SAE Technical Paper 2011-01-2049, 2011.
- [97] Kashdan JT, Thirouard B. A Comparison of Combustion and Emissions Behaviour in Optical and Metal Single-Cylinder Diesel Engines. SAE International Journal of Engines 2009;2(1):1857–72.
- [98] Pastor J, Javierlopez J, Garcia J. A 1D model for the description of mixing-controlled inert diesel sprays. Fuel 2008;87(13-14):2871–85.
- [99] Rodnyi PA, Khodyuk IV. Optical and luminescence properties of zinc oxide (Review). Optics and Spectroscopy 2011;111(5):776–85.

---

## 9 APPENDIX A

Dans le cadre de cette thèse, une technique de diagnostic optique a été développée pour mesurer simultanément la température et la vitesse du gaz dans un moteur thermique transparent.

L'objectif principal de ces travaux était de mesurer simultanément la température et la vitesse du gaz dans le cylindre d'un moteur optique en fonctionnement entraîné. La technique de la PIV-thermographique (T-PIV) combine la thermométrie par phosphorescence et la vélocimétrie par images de particules (PIV) et offre la possibilité de mesurer simultanément la température et la vitesse du gaz. Les travaux présentés dans cette thèse fournissent deux développements principaux de la technique : la caractérisation des matériaux luminophores en condition gazeuse et l'application de la T-PIV dans un environnement moteur.

Des matériaux luminophores appropriés pour les mesures en environnement moteur ont été choisis parmi trois luminophores disponibles dans le commerce : BAM:Eu<sup>2+</sup>, ZnO et ZnO:Zn. Une méthodologie a été mise en œuvre pour caractériser les luminophores en surface et en condition gazeuse.

La réponse spectrale d'émission lumineuse a été mesurée en fonction de divers paramètres, y compris celui de la température, dans le but d'obtenir une courbe d'étalonnage afin d'appliquer la technique au moteur. Dans cette étude, la méthode spectrale a été utilisée pour déterminer la température à partir du changement d'émission lumineuse. De plus, les luminophores ont été caractérisés par des variations paramétriques : la densité des particules, l'impact de la densité d'énergie du laser et la température. Dans le cadre de cette étude, un système de comptage de particules a été développé, capable de résoudre des densités de nombre de particules de l'ordre de  $10^{10}$ - $10^{11}$  particules/m<sup>3</sup>. Une comparaison des propriétés lumineuses obtenues à partir de mesures en surface d'une part et en gaz d'autre part a été effectuée. Les résultats obtenus ont montré que la caractérisation des luminophores en condition gaz est plus représentative pour une application dans un environnement moteur.

D'après les résultats obtenus dans ce travail, le luminophore ZnO:Zn montre une sensibilité à la température plus importante que le BAM:Eu<sup>2+</sup> et permet ainsi d'obtenir une plus faible incertitude sur la mesure de température. Pour cet raison, le ZnO:Zn a été choisi dans ce travail comme candidat pour mesurer la température et la vitesse du gaz dans un moteur optique.

L'une des nouveautés de ce travail a été l'utilisation du ZnO:Zn avec une taille de particule de 3,5 μm en tant que traceur pour les mesures de températures et de vitesses dans un moteur optique. La technique a été appliquée en différentes conditions moteur : en entraîné, en combustion, avec injection de carburant et avec variation paramétrique de la température d'admission. Ces tests ont permis de déterminer les potentiels de cette technique ainsi qu'une évaluation des incertitudes de mesures relatives à la mesure de température.

Les mesures ont été effectuées à un régime moteur de 1200 tr/min avec une fréquence d'échantillonnage de 10 Hz entre 180 et 540 °v<sub>il</sub> sans combustion. Les champs de températures et de vitesses ont été mesurés avec succès à différents angles vilebrequin pendant la phase de compression et de détente. Les champs de températures moyennes obtenus ont montré un écart par rapport à la simulation (0D) d'environ 1% (200 °CA) à 14% (480 °CA). En outre, les mesures effectuées avec une température d'admission plus élevée montrent un écart maximal de température d'environ 10 % à 390 °CA, ce qui correspond bien à la température estimée par la simulation 0D.

---

L'incertitude de mesure liée à l'étalonnage a été mesurée dans l'ordre de 55 K (18 %) à 300 K et de 2 K (0,3 %) à 614 K sur une moyenne de 200 cycles moteur. Cela laisse entrevoir la possibilité d'effectuer des mesures de température précises à des températures plus élevées (près du PMH) dans le cadre d'expériences futures. Les résultats indiquent une bonne précision près du point mort inférieur (dispersion similaire entre les deux températures) et une précision inférieure près du point mort supérieur. Toutefois le niveau de signal de phosphorescence diminue à haute température ce qui conduit à un faible rapport du signal sur background. Cet aspect induit une augmentation non négligeable de l'incertitude de mesure à haute température.

Pour la première fois, l'effet du Tumble a été étudié sur des champs de températures avec T-PIV. Les résultats montrent une légère diminution de la température de 9 K (300 °CA) et à 19 K (330 °CA) pendant la course de compression où l'augmentation du mouvement de Tumble devrait améliorer le transfert thermique aux parois du cylindre. La même baisse de température est également visible pendant la détente, avec une différence de température dans l'ordre de 32 K (480 °CA) par rapport aux conditions de référence.

Cette technique permet aussi de mesurer la stratification de la température due à l'injection de carburant. Les résultats obtenus montrent une distribution non homogène de la température à l'intérieur du cylindre due à l'évaporation du spray de carburant. On observe notamment une diminution de la température de l'ordre de 10 K au centre du cylindre. Ce résultat montre ainsi que la technique peut être utilisée pour mesurer la stratification de la température due aux injections de carburant dans un moteur.

La T-PIV a également été testée pour mesurer la température des gaz en post-combustion. La résistance des particules à la combustion a été étudiée dans une série de mesures de températures en conditions de combustion. Il a été constaté que le luminophore utilisé (ZnO:Zn) ne permet pas de réaliser les mesures post-combustion. L'absence du signal de luminescence empêche la mesure de la température. Dans ce cas, les mesures étaient impossibles, probablement en raison d'une dégradation du matériau luminophore utilisé qui ne résiste pas aux températures élevées de la combustion. Les perspectives de développements futures qui résultent de ces résultats sont la sélection d'un luminophore capable de résister à plus hautes températures. Cet aspect limite l'utilisation du luminophore ZnO:Zn exclusivement aux mesures en condition entraînée.

Enfin, la technique montre un grand potentiel de développement dans un environnement moteur.